Charles University in Prague
Faculty of Mathematics and Physics

Doctoral Thesis

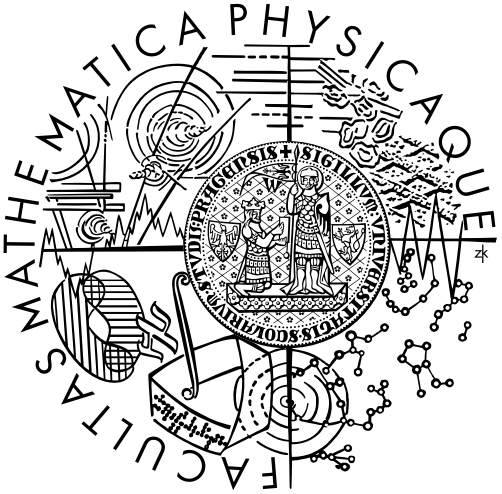

Nahlovskyy Bohdan Vasyl'ovych

The study of chemical diffusion and properties of electric contacts on CdTe for gamma ray detector applications

Institute of Physics of Charles University

Supervisor: Doc. RNDr. Roman Grill, CSc.

Branch: Quantum Optics and Optoelectronics

2010

dedicated to my brother

Acknowledgements

I express my deep gratitude to my supervisor Doc. RNDr. Roman Grill, CSc. for his guidance through the whole period of my study. I am grateful for his kindness, understanding and willingness to help. Our frequent discussions of various scientific problems were great sources of knowledge and inspiration for me. His contribution into the explanation of the experimental results and creating theoretical models were vital for this work.

It was a great honour for me to work in the group of Prof. RNDr. Pavel Höschl, DrSc. and I am very grateful to him for his big support during my doctoral study.

I would like to express my sincere thanks to Doc. Ing. Jan Franc, DrSc. and Ing. Eduard Belas, CSc. for excellent guidance at the beginning of my research work, providing valuable advises concerning research.

I am grateful to Doc. RNDr. Pavel Moravec CSc. who has provided assistance in constructing experimental set-up. His contribution into tuning equipment and planing experiment allowed to optimize measurements and obtain novel data.

I am thankful to Prof. RNDr. Ing. Josef Šikula, DrSc. from CNRL (VUT, Brno) for kind offer to exploit equipment for capacitance-voltage measurements and for the valuable discussion of the obtained results.

I would like to acknowledge Roman Fesh, Karol Strečko, Věra Poláková, Miloš Černý and all other workers of the Institute of Physics of Charles University in Prague for their help in my research and study.

I am especially grateful to my parents for their love, inspiration and support.

I hereby declare, that I wrote my doctoral thesis by myself using exclusively cited sources. Loan allowance granted.

Prague, 2010 Nahlovskyy B.V.

Contents

Introduction

Nowadays gamma ray detectors are used in various aspects of our life, including environmental [1] and security monitoring, nuclear science [2], and medical imaging [3]. Demands to the quality and accessibility at a reasonable cost of these devices increase every day. Medical applications are strictly limited by radiation dose living tissue can be exposed to. In security purposes, size and resolution are of main importance. Hence, detectors are required to be extremely sensitive, to have high image resolution, be portable and non fastidious in operation.

Semi-insulating (SI) cadmium telluride (CdTe) has long been known to have great potential in room-temperature gamma ray semiconductor detector applications [4, 5]. It has number of advantages over other semiconductor detectors used for the same purposes (Ge, GaN). High atomic numbers of both components (Z_{Cd}=48, Z_{Te}=52) makes it much more effective in radiation-atomic interaction. Large enough band gap ($1.5\,eV$) at room temperature provides high resistivity (above $10^9\,\Omega \cdot cm$) of the intrinsic material and therefore a low leakage current, critical for the high signal to noise ratio. High mobility of electrons ($\sim 1100\,cm^2/Vs$ at 300 K) allows to reach a high intrinsic $\mu\tau$ (mobility-lifetime) product and therefore a high degree of charge collection and a good spectral resolution. The full potential of this compound for high-energy photon detection applications, however, was not exploited for many decades due to the limited commercial availability of high-quality crystals [4]. This situation has changed dramatically during the mid nineties with the emergence of few companies committed to the advancement and commercialization of CdZnTe based radiation detector technology. Companies Endicott Interconnect Technologies, Inc. (U.S.A.), ACRORAD Company Ltd. (Japan), Nippon Mining & Metals Co. Ltd. (Japan), LETI-CEA (France), Redlen Technologies (Canada) offer large single-crystals grown by high pressure Bridgman (HPB) or travelling heater methods (THM).

Still, the growth of large single-crystals of CdTe is state-of-the art process. Conditions, under which high quality crystals grow, are not suitable for obtaining high resistivity material. Even ingots grown from 7N purity initial materials have free carriers concentration much higher than allowed maximum of $10^7\,cm^{-3}$. To achieve SI CdTe, the compensation of unintentional impurities and native defects by the pinning of the Fermi level to some deep level near the middle of the band gap is

necessary. However, high density of doping defects significantly increases trapping and recombination centres concentration, which decreases detection ability [6]. Another possibility to compensate native point defects (NPD) and decrease level of needed doping is the annealing in the atmosphere of one of the components to get stoichiometric composition.

Another problem of semiconductor gamma ray detectors is the leakage current. When it is comparative with the effective current going through the device, huge amount of signal is lost. Hence, sensitivity decreases significantly. Surface conductivity is responsible for the appearance of leakage current as well. By an appropriate surface treatment it is possible to overcame this problem. Surface treatment greatly influences the quality of contacts and properties of the metal-semiconductor junction.

The aim of this work is to investigate mass diffusion processes which occur in CdTe at temperatures above $500\,^{\circ}C$ and to find the conditions to obtain material with required properties. Study is done indirectly through the observation of changes in the material conductivity depending on the changes of the component vapour pressure.

The second part of the thesis concerns with surface treatment in various etching solutions, which is studied in detail first to get surfaces much more resistive than bulk material, second to prepare ohmic contacts to be used as electrodes. Three-terminal technique is employed for the measurement and results are compared with more common two-terminal method. Capacitance-voltage experiment is used to obtain additional information about contact properties.

Chapter 1

CdTe: Review

1.1 Crystal structure

Cadmium telluride belongs to the $A^{II}B^{IV}$ group of semiconductors with a cubic zincblende crystal structure (Figure (1.1)). This structure is described as a pair of inter-penetrating face centred cubic (fcc) sub-latices of each element, Cd and Te, offset from each other by one quarter of a unit cell body diagonal. The space group of this structure is called $F\bar{4}3m$ (in Hermann-Mauguin notation), or 216 in the International Tables for Crystallography.

The room temperature lattice parameter of CdTe is the largest among the $A^{II}B^{IV}$ compounds and depends on the deviation from stoichiometry. It varies from 6.480Å for crystals grown from Cd-rich melt to 6.488Å for grown from Te-rich one [7]. Recently, in research conducted on samples quenched after annealing, it was shown that the lattice parameter decreases with increasing deviation from stoichiometry for both Te- and Cd-rich cadmium telluride [8]. The lattice parameter of stoichiometric CdTe was reported to be 6.4825 Å.

Chemical bonds between cadmium and tellurium atoms are characterized as intermediate to ionic and covalent. They are formed by the Cd $5s^2$ and Te $5s^25p^4$ electrons. Atomic orbitals are mixed and form new sp^3 hybrid orbitals.

The shape of the Brillouin zone of zincblende structure is a truncated octahedron (Figure (1.2)) with fourteen plane faces, six square faces along the [100] direction and eight hexagonal faces along [111] direction.

1.2 Band structure

CdTe has a direct energy band structure with a minimum of the conduction band and maximum of the valence band in the centre of Brillouin zone, Γ point.

The Kane model [9] is used to calculate the band structure. In this model atomic wave function and the spin of electron are taken into consideration. Interactions, which determine the heavy hole effective mass are not included in the simplified

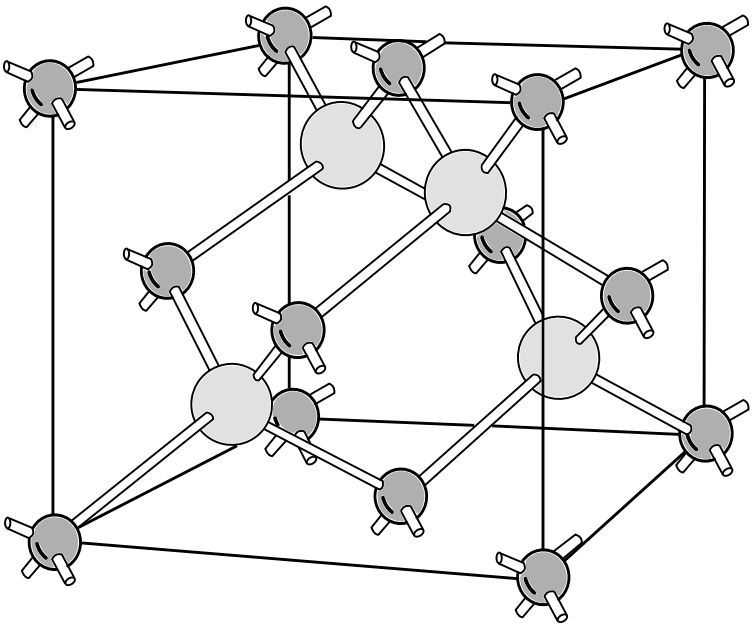

Figure 1.1: Zincblende crystal structure. The arrangement of atoms is the same as in diamond cubic structure, but with alternating types of atoms at the different lattice sites.

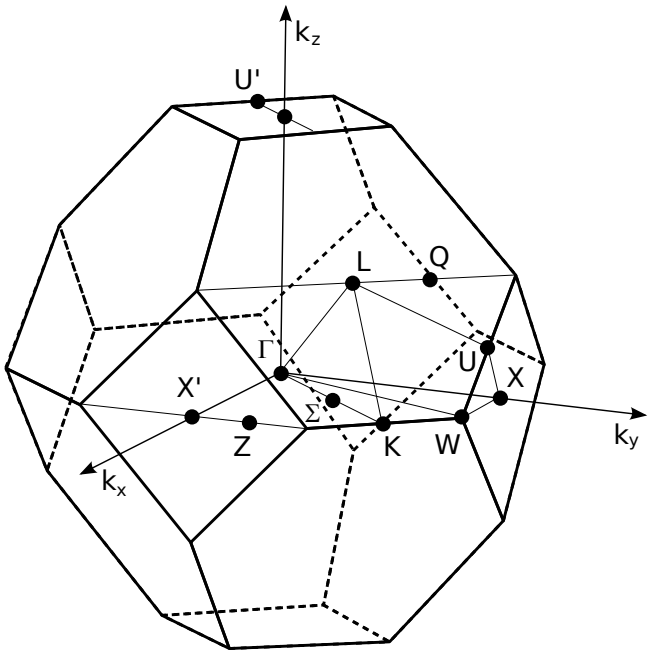

Figure 1.2: Brillouin zone of zincblende structure.

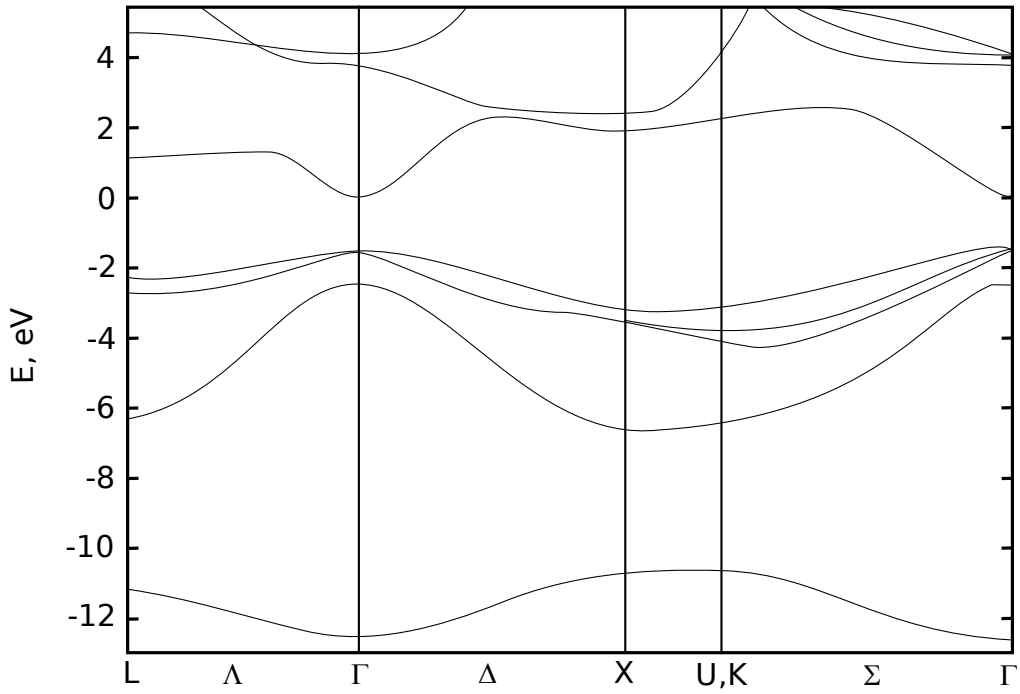

Figure 1.3: Cadmium telluride band structure diagram.

Kane's model.

The valence band structure consists of three bands, two of them are degenerated at $\vec{k} = 0$. The third sub-band is split-off by the spin orbit coupling. The split-of energy at $\vec{k} = 0$ is denoted by Δ. The conduction and valence band dispersion can be approximated by the following forms:

- conduction band

$$E - E_g = \frac{\hbar^2 k^2}{2m_0} + \frac{1}{2}\left(\sqrt{E_g^2 + \frac{8P^2k^2}{3}} - E_g\right) \tag{1.1}$$

  where P is Kane's matrix element ($P = 8 \times 10^{-8}\, eVcm$),

- valence band
  - heavy holes

$$E = -\frac{\hbar^2 k^2}{2m_h} \tag{1.2}$$

  - light holes

$$E = \frac{\hbar^2 k^2}{2m_0} - \frac{1}{2}\left(\sqrt{E_g^2 + \frac{8P^2k^2}{3}} - E_g\right) \tag{1.3}$$

– split-off band

$$E = -\Delta + \frac{\hbar^2 k^2}{2m_0} - \frac{P^2 k^2}{3(E_g + \Delta)} \tag{1.4}$$

where $\Delta = 0.8$ eV.

As can be seen in Figure (1.3) the conduction band and the light hole valence band are non-parabolic. That means that E is not simply proportional to k^2.

The value of the forbidden gap depends on the temperature. Various authors investigated the energy gap temperature dependence of CdTe. According to Brebrick [10]:

$$E_g = 1.70 - 5.345 \times 10^{-4} T, eV. \tag{1.5}$$

D. Nobel [11] gives different equation:

$$E_g = 1.622 - 3.5 \times 10^{-4} T - 1.1 \times 10^{-7} T^2, eV. \tag{1.6}$$

CdTe has relatively wide band gap which allows to use non-degenerate statistics for moderate carrier concentration. The low effective mass of the electron ($m_e = 0.096 m_0$) in CdTe results in good transport properties of electrons.

1.3 Crystal growth methods

A large diameter CdTe single crystals are strongly desired for the application in semiconductor technology. The ingots are sliced with an inner diameter diamond coated blade and polished to form wafers. A wafer is a thin slice of material used in the fabrication of integrated circuit and other micro-devices. The wafer serves as the substrate for microelectronic devices built in and over the wafer and undergoes to many micro-fabrication process steps such as doping or ion implantation, etching, deposition of various materials, and photo-lithographic patterning. Requirements to the crystals' quality are very high. Wafers are formed of high purity (99.9999%), nearly defect-free single crystalline material. Crystal diameter is important as well. The larger the wafer, the less space on the edges as a percentage of total space. This means, less of the wafer is un-etched, and in theory should have higher productivity. This is the basis of shifting to larger and larger wafer sizes.

There is no single best method of crystal preparation. A number of them were developed. Each of this method has its advantage and disadvantage and the growth technique is chosen depending on various parameters.

- Czochralski method

  For many semiconductor materials pulling from the melt by the Czochralski method (Figure 1.4) is the dominant technique for obtaining single crystals. A seed crystal, mounted on a rod, is dipped into the molten material. The seed

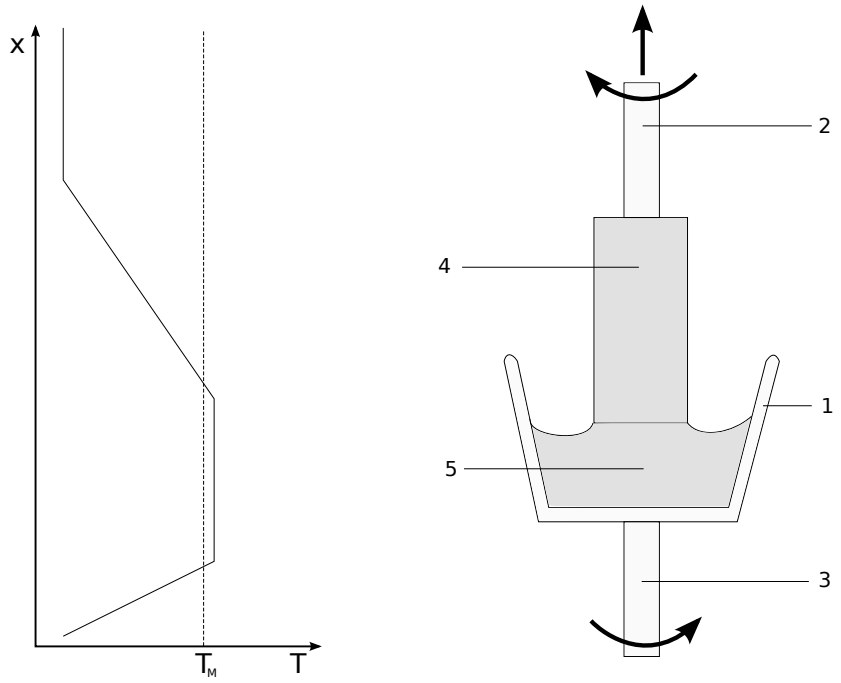

Figure 1.4: Temperature profile and schematic graph of the Czochralski process. T_M - melting point temperature; 1 - crucible; 2, 3 - rods, rotated in opposite directions; 4 - ingot; 5 - melt.

crystal's rod is pulled upwards and rotated at the same time. By precisely controlling the temperature gradients, rate of pulling and speed of rotation, it is possible to extract a large, single-crystal, cylindrical ingot from the melt. Occurrence of unwanted instabilities in the melt can be avoided by investigating and visualizing the temperature and velocity fields during the crystal growth process. This process is normally performed in an inert atmosphere, such as argon, and in an inert chamber, such as quartz.

High cadmium vapour pressure does not allow to use this method directly for CdTe growth. Its modification, liquid encapsulated Czochralski (LEC) [12, 13] in which liquid encapsulation prevents the loss of volatile Cd, can be used instead. However, despite LEC has been proven to be suitable for several other compound semiconductors, it has not succeeded for CdTe. Its disadvantage is in large temperature non-linearities and large temperature gradients causing high thermal stress in the growing crystal.

- Vapour growth method

  Growth process under this technique is performed at temperatures lower that the material melting point. The crystals are grown in a closed crucible which is moved through a step temperature gradient [14, 15]. The source material is always hotter than the growing surface as shown on Figure (1.5). Thus, mass transport occurs from the source to the crystal. The extended growth

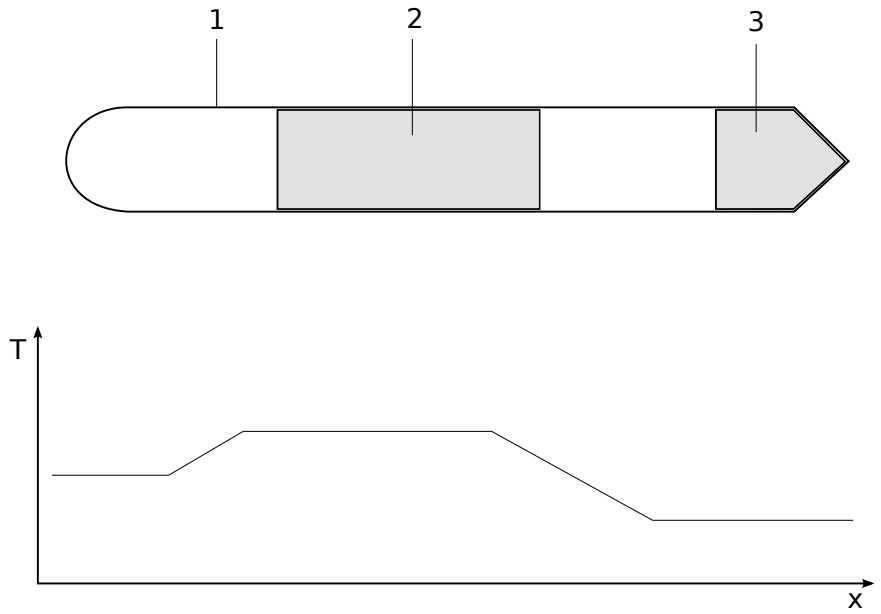

Figure 1.5: Schematic graph and temperature profile of the vapour phase growth technique. 1 - quartz ampoule; 2 - charge; 3 - crystal.

period allows the defects to reach a state of equilibrium, where most of the dislocations content is concentrated in sub-grain boundary walls. This method is used to growth CdZnTe with different compositions.

- Travelling heater method

  Float-zone method was initially developed for the crystal purification. Latter it was found to be suitable for the crystal growth.

  Material obtained from float-zone technique is a high-purity alternative to crystals grown by the Czochralski process. The concentrations of impurities, such as carbon and oxygen, are extremely low. impurity The dimensions of float-zone wafers are generally less than $150\,mm$ due to the surface tension limitations during growth. A radio-frequency (RF) field is used to produce a local melted zone on the polycrystalline rod that is dragged from one end to the other. Float-zone pulling is shown on Figure (1.6). Seed crystal is used at one end in order to start the growth. The whole process is carried out in an evacuated chamber or in an inert gas purge. The molten zone carries the impurities away with it and hence reduces impurity concentration (impurities are mostly more soluble in the melt than in crystal). Specialized doping techniques like: Core doping, Pill doping, Gas doping and Neutron transmutation are used to incorporate a uniform concentration of dopant.

  The growth rate is very slow, about $5\,mm/day$, to prevent supercooling. That

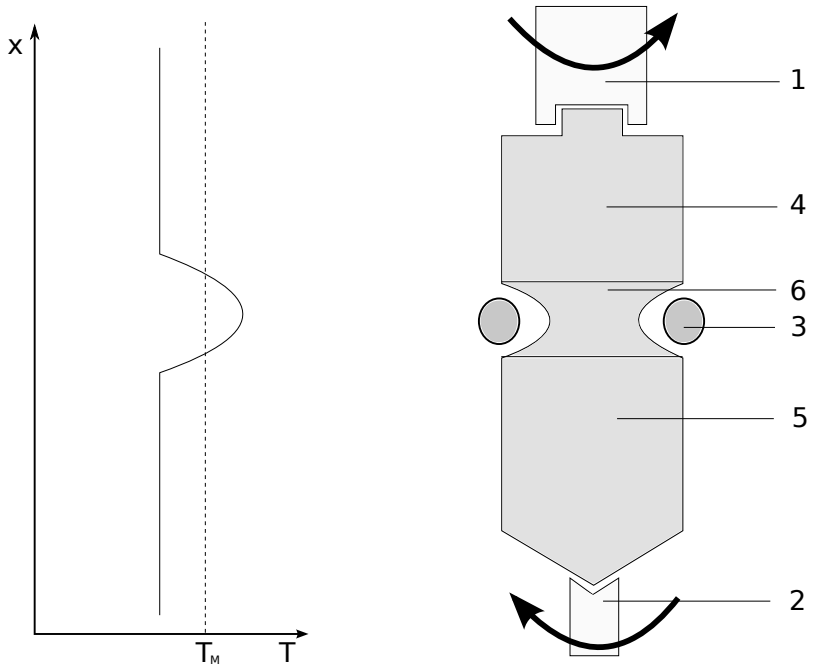

Figure 1.6: Temperature profile and schematic graph of the float-zone growth method. T_M - melting point temperature; 1 - feed rod holder; 2 - seed rod holder; 3 - RF heating coil; 4 - feed rod; 5 - single crystal; 6 - molten zone.

is why this method is not appropriate for the growth of large crystals. Ingots, obtained by this method, usually have several grains. Therefore, this technique is effective for manufacturing of high purity crystals with large grains for devices based on small chips such as radiation detectors.

- Vertical gradient freeze method

  Gradient freeze method along with Bridgman method are the most frequently used for melt growth of CdTe and related compounds. The vertical modification, called Vertical Gradient Freeze, is preferred in industrial use because of higher demand on round wafers.

  The method involves heating of polycrystalline material in a container above its melting temperature and slow cooling from its one end. Single crystal material is progressively formed along the length of the container. The process can be carried out in a horizontal or vertical geometry. The source material is at the fixed position without movement. The temperature is gradually lowered so that the growth rate changes as a function of temperature. Generally, the growth rate becomes faster when the temperature becomes lower. Therefore, stable crystal growth becomes difficult as the crystal growth proceeds. In order to prevent this growth rate change, the temperature distribution in the furnace must be precisely controlled.

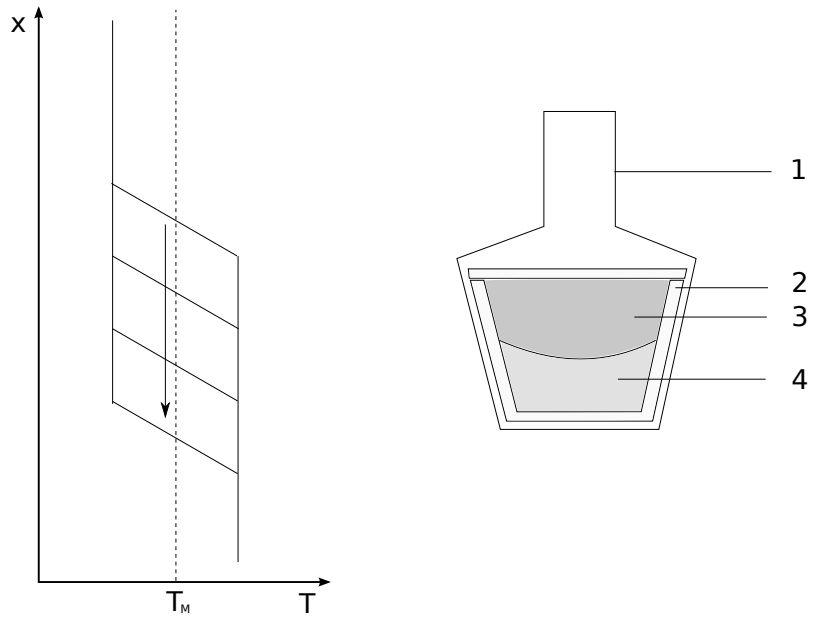

Figure 1.7: Temperature profile change and schematic graph of the vertical gradient freezing method. T_M - melting point temperature; 1 - quartz ampoule; 2 - crucible; 3 - crystal; 4 - melt.

- Bridgman technique

  CdTe crystals can be grown by the low pressure Bridgman, also called Bridgman-Stockbarger, technique in a closed evacuated ampoule with small tellurium excess [16]. The three material phases, solid, liquid and gas, coexist during the growth, and the pressure in the ampoule is nearly equal to the tellurium vapour pressure at the growth temperature. Under these conditions the crystal contains excess tellurium atoms that during cool down come out as precipitates, mainly at dislocations and grain boundaries.

  The crystal quality improves and precipitates are avoided by applying the modified Bridgman technique [16, 17, 18]. In this procedure there is small cadmium excess in the ampoule. During crystal growth one ampoule end is kept at lower temperature that defines component vapour pressure in the system. The growth process involves continuous material transfer between the three phases. The constant vapour pressure keeps constant liquid composition, and balanced amounts of cadmium and tellurium within the crystal.

  Figure (1.8) and Figure (1.9) present the horizontal and vertical versions of this technique, respectively. In both cases the crystal grows from the melt by moving it along a region with temperature gradient that extends from above to below the melting point. The growth may proceed by mechanically moving the ampoule, or by moving the furnace. In recent systems the furnace consists

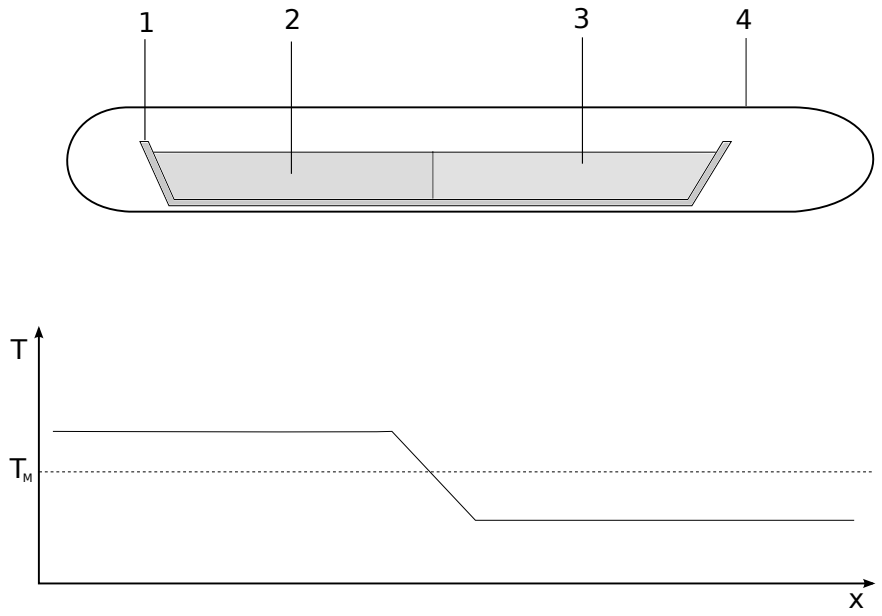

Figure 1.8: Schematic graph and temperature profile of the Bridgman growth method. T_M - melting point temperature; 1 - crucible; 2 - melt; 3 - crystal; 4 - quartz ampoule.

of several heating zones and a computer control of temperature profile. The computer shifts the profile electronically and there are no mechanically moving parts within the furnace [17, 18].

The vertical configuration, shown in Figure (1.9), is preferred for the industrial production because of higher yield of round wafers compared to the horizontal method.

In high pressure Bridgman (HPB), crystals grow from a melt of nearly equal quantities of cadmium and tellurium, with small cadmium excess. High pressure of the Ar requires growth furnace of special design. The crystal grows at high temperature, above 1100°C, at a high growth rate of few millimetres per hour. Zinc addition increases the crystal's band gap and electrical resistivity, therefore, it reduces the detector's spectral broadening by dark current noise. HPB yields high quality detectors and detector arrays, however, the crystal uniformity is limited, and the detector's yield is low. Control of the high pressure system is inconvenient.

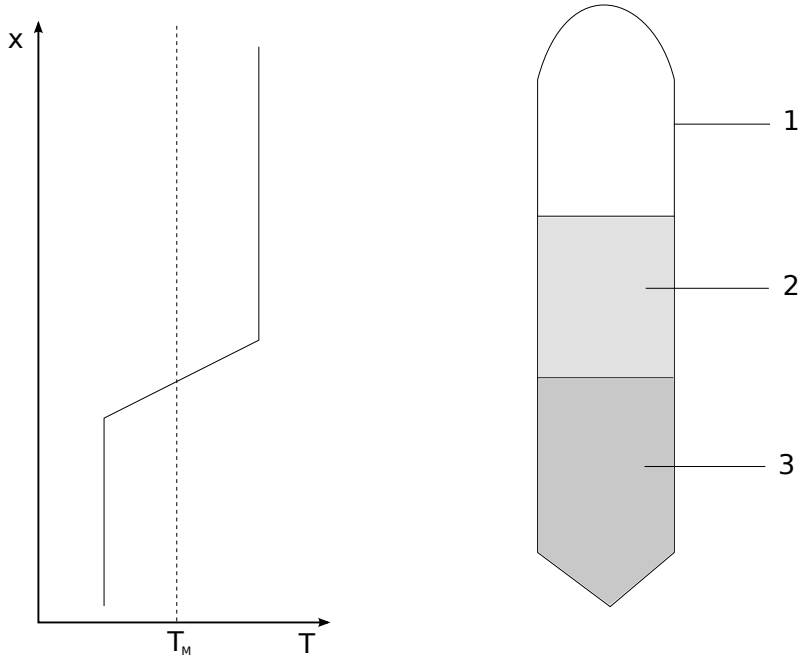

Figure 1.9: Schematic graph and temperature profile of the vertical Bridgman growth method modification. T_M - melting point temperature; 1 - quartz ampoule; 2 - melt; 3 - crystal.

1.4 Defects

At the absolute zero temperature the crystal in the thermodynamic equilibrium is completely ordered. This follows from the Gibbs free energy

$$\Delta G = \Delta H - T\Delta S. \tag{1.7}$$

At temperatures above absolute zero a deviation from ideal structure occurs. It can be described in terms of different type defects. Electrical properties of the semiconductor material greatly depend on the concentration of the point defects. Interaction between defects is described by the quasi-chemical defect reaction (QCDR) approach proposed by Kröger [19].

Electric properties at room temperature are influenced by defect reactions, which proceed during the cooling, due to different electric characteristics (valence, ionization energies) of the input/output reacting defects. The final defect structure is determined by the temperature T at which the reactions have frozen. Generally speaking, various defect reactions freeze at different temperatures and the final defect structure is influenced by the whole history of the crystal.

Dominant native defects routinely accepted in CdTe are Cd vacancy (V_{Cd}), Cd interstitial (Cd_I) and Te antisite (Te_{Cd}) [20, 21]. The existence of Te_{Cd} is well-grounded in Te-rich CdTe [20, 21] but its electrical character has not been set yet.

Also ionization energies of V_{Cd} were not fixed definitely and both shallow and mid-gap second ionization level of V_{Cd} is used in recent literature [20, 22].

The neutral defect densities are set by P_{Cd} via the reactions and respective forms [23]

$$Cd_I^0 \leftrightarrow Cd_g, \tag{1.8}$$

$$\left[Cd_I^0\right] = n_o \frac{P_{Cd}}{\mathcal{K}} \exp\left[\frac{S(Cd_I)^{vib}}{k_b}\right] \times \exp\left[-\frac{E(Cd_I) + U(Cd_I)^{vib}}{k_b T}\right], \tag{1.9}$$

$$V_{Cd}^0 \leftrightarrow Cd_{Cd} - Cd_g, \tag{1.10}$$

$$\left[V_{Cd}^0\right] = n_o \frac{\mathcal{K}}{P_{Cd}} \exp\left[\frac{S(V_{Cd})^{vib}}{k_b}\right] \times \exp\left[-\frac{E(V_{Cd}) + U(V_{Cd})^{vib}}{k_b T}\right], \tag{1.11}$$

$$Te_{Cd}^0 \leftrightarrow 2Cd_{Cd} + Te_{Te} - 2Cd_g, \tag{1.12}$$

$$\left[Te_{Cd}^0\right] = n_o \frac{\mathcal{K}^2}{P_{Cd}^2} \exp\left[\frac{S(Te_{Cd})^{vib}}{k_b}\right] \times \exp\left[-\frac{E(Te_{Cd}) + U(Te_{Cd})^{vib}}{k_b T}\right]. \tag{1.13}$$

E is the relevant formation energy related to corresponding defect reaction, the energy U^{vib} and entropy S^{vib} determine contributions to the vibrational free energy. The parameter

$$\mathcal{K} = (k_b T)^{5/2} \left(\frac{m_{Cd}}{2\pi\hbar^2}\right)^{3/2} \tag{1.14}$$

connects Cd chemical potential μ_{Cd} to P_{Cd} as

$$\mu_{Cd} = k_b T \ln \frac{P_{Cd}}{\mathcal{K}}. \tag{1.15}$$

$n_o = 1.48 \times 10^{22}\, cm^{-3}$ is the Cd or Te atom density, k_b is the Boltzmann constant, and m_{Cd} is the mass of Cd atom.

The densities of multiply ionized defects are calculated for acceptors and donors

$$\left[X^{z-}\right] = \left[X^0\right] \frac{g_{X^{z-}}}{g_{X^x}} \exp\left(\frac{z\mu_F - E_a^1 - ... - E_a^z}{k_b T}\right), \tag{1.16}$$

$$\left[X^{z+}\right] = \left[X^{0}\right] \frac{g_{X^{z+}}}{g_{X^{0}}} \exp\left(\frac{E_d^1 + ... + E_d^z - z\mu_F}{k_b T}\right), \tag{1.17}$$

where E_a and E_d are the acceptor and donor one-electron ionization energies. $g_{X^{z-}}$ and $g_{X^{z+}}$ are the degeneracies of the defects. The index z means the ionization degree.

In Cl-doped CdTe the set of point defects is completed by shallow donor Cl_{Te} and shallow acceptor complex labelled A-centre A$\equiv$($Cl_{Te}V_{Cd}$). All defect densities both in neutral and charged modifications are easily calculated with quasi-chemical formalism [5]. In relatively strongly doped CdTe:Cl the Fermi energy μ_F is elevated above the value in undoped CdTe and the density of native donors is reduced. At P_{Cd} near saturation, the equilibrium density of Te_{Cd} is minimum and we thus omit this defect in this thesis. In analytical calculations we skip also Cd_I and demonstrate on exact numerical results the validity of such simplification.

The native defects formation, vibration, and ionization energies, vibration entropies, factors of degeneracy as well as gap energy E_g according to [5] are used. The second ionization energy of V_{Cd} is set $0.3E_g$ above the top of the valence band. The density of Cl related A-centre formed by singly ionized V_{Cd}^- and Cl_{Te}^+ is calculated with

$$\left[\mathrm{A}^0\right] = \frac{g_A}{n_o} \left[\mathrm{V}_{\mathrm{Cd}}^-\right] \left[\mathrm{Cl}_{\mathrm{Te}}^+\right] e^{-\frac{E_A}{k_b T}}, \tag{1.18}$$

$$\left[\mathrm{A}^-\right] = \frac{[\mathrm{A}^0]}{2} e^{\frac{\mu_F - E_a}{k_b T}}, \tag{1.19}$$

where configuration degeneracy for A-center incorporating donor in Te sublattice $g_A = 4$, atom density of Cd or Te $n_o = 1.48 \times 10^{22}$ cm^{-3}, and the A-centre ionization energy $E_a = 120$ meV [24]. E_A is the A-centre formation energy fitted to experimental data.

Having fixed defect thermodynamic parameters, the Fermi energy is calculated solving electric neutrality condition

$$\begin{aligned} n + \left[\mathrm{V}_{\mathrm{Cd}}^-\right] + 2\left[\mathrm{V}_{\mathrm{Cd}}^{2-}\right] + \left[\mathrm{A}^-\right] = \\ p + \left[\mathrm{Cd}_{\mathrm{I}}^+\right] + 2\left[\mathrm{Cd}_{\mathrm{I}}^{2+}\right] + \left[\mathrm{Cl}_{\mathrm{Te}}^+\right], \end{aligned} \tag{1.20}$$

n, p being free electron and hole densities, with parallel fulfilment of Cl balance equation

$$[\mathrm{Cl}] = \left[\mathrm{Cl}_{\mathrm{Te}}^0\right] + \left[\mathrm{Cl}_{\mathrm{Te}}^+\right] + \left[\mathrm{A}^0\right] + \left[\mathrm{A}^-\right]. \tag{1.21}$$

Leaving out defects with low density V_{Cd}^-, Cd_I^+, Cd_I^{2+}, Cl_{Te}^0, A^0, and p in eqs.

(1.20) and (1.21), n may be expressed as

$$n = [\mathrm{Cl}]\,\frac{1 - \frac{g_A}{2n_o}\left[\mathrm{V}_{\mathrm{Cd}}^{-}\right] e^{\frac{\mu_F - E_a - E_A}{k_b T}}}{1 + \frac{g_A}{2n_o}\left[\mathrm{V}_{\mathrm{Cd}}^{-}\right] e^{\frac{\mu_F - E_a - E_A}{k_b T}}} - 2\left[\mathrm{V}_{\mathrm{Cd}}^{2-}\right]. \tag{1.22}$$

Note that $\mathrm{V}_{\mathrm{Cd}}^{-}$ cannot be neglected here due to multiplication with adjacent exponential function. Looking for the solution of equation (1.22), two characteristic regimes are identified in CdTe:Cl. (i) At high P_{Cd} an uncompensated material characterized by $[\mathrm{V_{Cd}}] \ll [\mathrm{Cl}]$ and stable $n \approx [\mathrm{Cl}]$ is obtained. (ii) Lower P_{Cd} results in an increased $[\mathrm{V_{Cd}}]$ and mutual donor-acceptor compensation, which allows to neglect n in equation (1.22). Such a simplification immediately allows to establish the correlation between μ_F and P_{Cd} in a form

$$\mu_F \propto \frac{k_b T}{2} \ln P_{\mathrm{Cd}}, \tag{1.23}$$

which yields $n \propto P_{\mathrm{Cd}}^{0.5}$ being typical for compensated CdTe [25]. The relation (1.23) implies that densities of principal point defects $\mathrm{V}_{\mathrm{Cd}}^{2-}$, A^{-}, and $\mathrm{Cd}_{\mathrm{I}}^{2+}$ are only weakly dependent on P_{Cd} in compensated regime.

1.5 Electric transport properties

The transport properties provide valuable information about the type and concentration of the carriers, the band structure and the electron scattering mechanisms.

Transport properties of electrons and holes in cadmium telluride are influenced by the scattering on the optical [26] and acoustic [27, 28] phonons and ionized impurities. Since there are two atoms per primitive unit cell in zincblende structure, there are six phonon branches - three acoustic and three optical. Along the high-symmetry directions the phonons are classified as transverse or longitudinal. This is done according to the displacement relatively to the direction of wave vector.

From the energy and temperature dependence of the scattering rate it can be found, that:

- $\mu \approx \mathrm{T}^{-\frac{3}{2}}$ - scattering on acoustic phonons (deformation potential);
- $\mu \approx \mathrm{T}^{-\frac{1}{2}}$ - scattering on acoustic phonons (piezoelectric);
- $\mu \approx \mathrm{T}^{-\frac{1}{2}}$ - scattering on polar optical phonons;
- $\mu \approx \mathrm{T}^{\frac{3}{2}}$ - scattering on ionized impurities.

The combined mobility is given by the sum of different scattering mechanism mobilities via Matthiessen rule

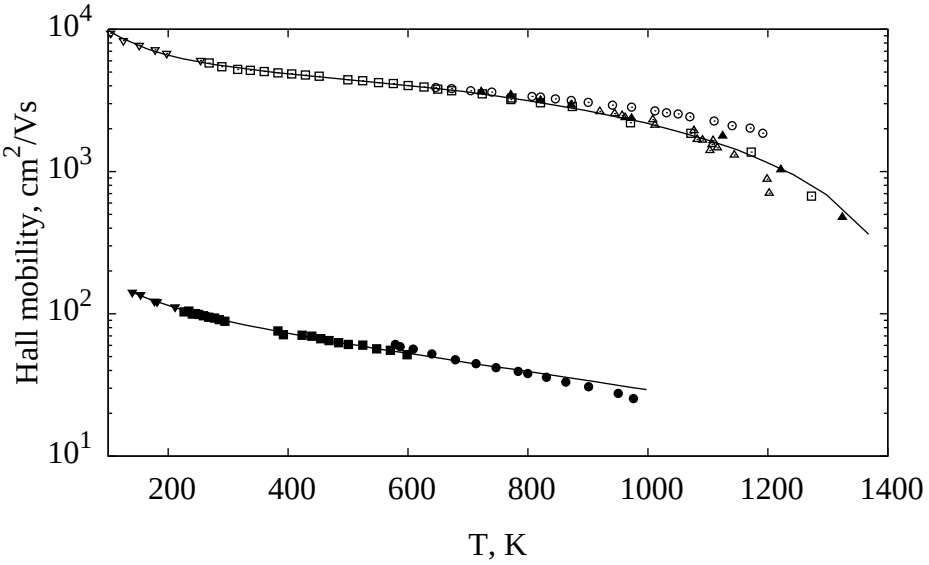

Figure 1.10: Hall mobility data for electrons (▽ - Segall [29], □ - Turkevych [31], ○ - Smith [32], ▲ - Franc [33]) and holes (▼ - Yamada [30], ■ - Turkevych [31], ● - Smith [32]) in CdTe. Lines represents best theoretical fit for electrons [31] and holes [34]

$$\mu = \left(\sum_i \frac{1}{\mu_i} \right)^{-1}. \tag{1.24}$$

Experimental results on Hall mobility for electrons and holes are presented in Figure (1.10). In case of electrons at lower temperatures the mobility is limited by a scattering of electrons on ionized impurities and polar optical phonons [29]. At mid-temperature region the scattering on polar optical phonons dominates. Theoretical form for the polar optical phonon mobility of holes was proposed by Yamada [30]

$$\mu_h^{PO} = 57[e^{\frac{252}{T}} - 1]. \tag{1.25}$$

Recent results obtained at high temperatures are in good agreement with this model. This means that no other type of scattering takes place there.

1.6 Application

CdTe and CdZnTe are used for various applications. CdTe is a highly useful material in the making of thin film photovoltaic modules (photovoltaics). Thin-film CdTe provides a greatly cost-effective solar cell design, but at a smaller efficiency than poly-silicon.

CdTe can be alloyed with mercury to make a versatile infra-red detector material (HgCdTe).

CdTe is used as an infra-red optical material for optical windows and lenses but it has small application and is limited by its toxicity so that few optical laboratories will consider working with it.

CdTe is also applied for electro-optical modulators. It has the greatest electro-optic coefficient of the linear electro-optic effect among II-VI compound crystals ($r_{41} = r_{52} = r_{63} = 6.8{\times}10^{-12}\, m/V$).

CdTe alloyed with a small amount of zinc makes an excellent solid-state X-ray and gamma ray detector (CdZnTe). Radiation detectors using CdZnTe can operate in direct-conversion (or photoconductive) mode at room temperature, unlike some other materials, particularly germanium, which require liquid nitrogen cooling. Their relative advantages include high sensitivity for x-rays and gamma-rays, due to the high atomic numbers of Cd and Te, and better energy resolution than scintillator detectors. CdZnTe can be formed into different shapes for different radiation-detecting applications, and a variety of electrode geometries, such as coplanar grids, have been developed to provide unipolar (electron-only) operation, thereby improving energy resolution.

The material has a high electro-optic coefficient and transparency in the mid-infra-red region, making it a good modulator material for infra-red lasers. The same properties make it useful for detection of terahertz waves.

An additional use is as a substrate material for the epitaxial growth of mercury cadmium telluride (HgCdTe), an infra-red detector material. $Cd_{0.96}Zn_{0.04}Te$ is almost perfectly lattice matched to LWIR HgCdTe (80% Hg, 20% Cd). However, it is difficult to grow large crystals of fixed composition.

Chapter 2

Diffusion in CdTe

X-ray and gamma ray detector application depends upon properties of CdTe that are sensitive to native defect and impurity concentrations which, in turn, are influenced by crystal growth as well as by post-growth annealing processes.

Rather impressive changes in properties are produced by slight change in stoichiometry – often less than 10^{-5} atomic fraction. CdTe changes the carrier type with slight shift in stoichiometry. In a practical sense, the rate of change of crystal composition upon annealing is relevant to the processing of this material for device application. Changes in composition are controlled by the interdiffusion coefficient, D, which is related to the self-diffusion coefficients and the thermodynamic factor. The self-diffusion coefficients are in turn related to the individual defect concentrations and mobilities. Thus, the dependence of self-diffusion coefficients upon component pressure provides insight into the dominant native defects which exist in CdTe.

There are two principal diffusion quantities of interest in describing component diffusion, the self-diffusion coefficients, D_{Cd} and D_{Te} and the interdiffusion coefficient, D_{CdTe}. Since there are no concentration differences in true self-diffusion, Fick's law should be obeyed and an experimental profile should be 'normal' in the sense that it may be analytically represented by the appropriate solution to Fick's law. By contrast, the interdiffusion coefficient may vary with position since interdiffusion occurs in the presence of concentration gradients. The interdiffusion coefficient is related to the self-diffusion coefficients by the Darken equation [35],

$$D_{CdTe} = (N_{Te} D^T_{Cd} + N_{Cd} D^T_{Te}) \cdot \frac{d \ln a_{Cd}}{d \ln N_{Cd}}, \tag{2.1}$$

where N_{Cd} and N_{Te} are the mole fractions of Cd and Te, D^T_{Cd} and D^T_{Te} are the tracer diffusion coefficients of Cd and Te, and a_{Cd} is the activity of cadmium. The term $(d \ln a_{Cd}/lnN_{Cd})$ is named the thermodynamic factor. The value of the D_{CdTe} is expected to be much larger than the largest of the self-diffusion coefficients because of the large values expected for the thermodynamic factor.

Point defect model for the evaluation of tracer diffusion coefficients was proposed by Chern and Kröger [36]:

$$D_{Cd}^{T} = \frac{1}{n_0} \sum_{X_{Cd}} f_{X_{Cd}} D_{X_{Cd}} [X_{Cd}], \tag{2.2}$$

$$D_{Te}^{T} = \frac{1}{n_0} \sum_{X_{Te}} f_{X_{Te}} D_{X_{Te}} [X_{Te}], \tag{2.3}$$

where $f_{X_{Cd}}$, $f_{X_{Te}}$ are correlation coefficients and $D_{X_{Cd}}$, $D_{X_{Te}}$ are the diffusion coefficients of the cadmium X_{Cd} and tellurium X_{Te} related defects respectively.

2.1 Interdiffusion

Out of all II-VI compounds, which can be prepared both n- and p-type without doping, CdTe has the widest gap. The n- of p-type is obtained by annealing in Cd or Te atmosphere, respectively. The early research of diffusion in CdTe was made by De Nobel [11]. Annealing was done at high temperature at pressure P_{Cd}. Samples were quenched to room temperature. Measured n-type electrical conductivity varied as $P_{Cd}^{1/2}$. Assumption was made that high temperature defect structure is preserved during the quenching operation. A conclusion was made that a singly ionized cadmium interstitial dominates the charge neutrality condition:

$$[Cd_i^+] = n = K P_{Cd}^{1/2}. \tag{2.4}$$

In the more recent measurements [37, 38, 32, 39] at elevated temperatures conductivity was found to vary as $P_{Cd}^{1/3}$. This time doubly ionized cadmium interstitial is considered to rule the charge neutrality condition:

$$2[Cd_i^{2+}] = n. \tag{2.5}$$

Independence of the conductivity from P_{Cd} at high cadmium pressure was reported for the undoped CdTe [38]. No simple defect model has been proposed to explain both these results and the high temperature conductivity.

The chemical diffusion coefficient was measured by relating step-like changes in cadmium pressure (P_{Cd}) to subsequent changes in conductivity. The following temperature dependence of the D_{CdTe} for the temperature range 600-800 °C was given by Zanio [40]:

$$D_{CdTe} = 4 \cdot e^{\frac{-1.15 \pm 0.1 eV}{k_B T}} (cm^2/s). \tag{2.6}$$

Rud' and Sanin performed similar type measurements in the temperature range 700-900 °C [41]:

$$D_{CdTe} = 1.03 \cdot e^{\frac{-0.97 eV}{k_B T}} (cm^2/s). \tag{2.7}$$

It was also reported that diffusion data for increasing and decreasing step-change in P_{Cd} produce slightly different D_{CdTe}. For $\Delta P_{Cd} > 0$ a single exponential described the transient of the electrical conductivity while at $\Delta P_{Cd} < 0$ a more complex behaviour involving conductivity varying with time according to a sum of two exponential functions.

Detailed interpretation of interdiffusion in cadmium telluride in terms of native point defects have been given in [42] and [43]. Intrinsic defects such as cadmium vacancies and cadmium interstitials were reported to be responsible for the D_{CdTe}.

2.2 Cd diffusion

Preliminary studies indicate that Cd-tracer diffusion coefficient D_{Cd} increases with increasing cadmium pressure, which was associated with interstitial diffusion mechanism [11]. Similar dependence was reported for CdS [44] and for CdSe [45]. However, in later studies [46] of the cadmium self-diffusion in CdTe over the temperature range 700-1000 °C and at various cadmium pressures D_{Cd} was found to be independent of pre-annealing treatment and also independent of Cd pressure. The temperature dependence was represented by:

$$D_{Cd} = (1.26^{+1.07}_{-0.72}) e^{\frac{-2.07 \pm 0.08 eV}{kT}} (cm^2/s) \tag{2.8}$$

for the whole temperature range. An exchange mechanism, a ring mechanism and a neutral associate of a cadmium vacancy and cadmium interstitial were suggested as a possible explanations for the independence of D_{Cd} upon P_{Cd}.

Time required to establish a new uniform conductivity after a change in component pressure was also studied. It was found to be $\sim 10^3$ shorter than times necessary to homogenize the radio-tracer composition. Rapid rate of equilibration of the electronic defects was explained by the generation of point defects internally, without mass transport from the external vapour. The crystal interior was presumed to sense the external pressure changes via dislocations and thereby cause point defect generation [47]. A quantitative correlation between the rate of attainment of electronic equilibrium, an estimated dislocation diffusion coefficient and the dislocation density was shown. However, Zanio [40] showed that there is no correlation between the interdiffusion coefficient and the dislocation density in CdTe.

A large difference in the rate of attainment of electronic equilibrium and the homogeneous distribution of the tracer was explained by expected difference in diffusion behaviour with and without a concentration gradient. The rate of attainment of electronic equilibrium for a step jump in component pressure depends upon the chemical diffusion coefficient, since a gradient in concentration is initially established by changing the external component pressure. The tracer self-diffusion coefficient, however, refers to diffusion in the absence of a concentration gradient and may be

much smaller then the interdiffusion coefficient [48]. In the CdTe the interdiffusion coefficient is related to the two self-diffusion coefficients and the thermodynamic factor, as given in equation (2.1).

It was reported later [36], that D_{Cd} is practically independent of P_{Cd} and low cadmium pressures, but at high cadmium pressures D_{Cd} slightly increases and approaches $D_{Cd} \propto P_{Cd}^{1/3}$ relation near Cd saturated conditions. This effect became significant at temperatures higher than 800°C while at 700°C the increase is smaller.

D_{Cd} was also reported independent of P_{Cd} in [49], within experimental error, as determined by the values at P_{Cd}^{max} and P_{Cd}^{min}:

$$D_{Cd}(P_{Cd}^{max}) = 326 \times e^{\frac{-2.67eV}{k_B T}} (cm^2/s) \tag{2.9}$$

$$D_{Cd}(P_{Cd}^{min}) = 15.8 \times e^{\frac{-2.44eV}{k_B T}} (cm^2/s) \tag{2.10}$$

The complex defect model was developed to describe the diffusion behaviour, which involves more than one mechanism. In accordance with equation (2.1), the two largest contributions to D_{Cd} were reported to be interstitial mechanism involving Cd_i^{2+} at high pressures, which is dependent upon $P_{Cd}^{1/3}$, and a pressure independent ring mechanism involving neutral associate $(V_{Cd}Cd_i)^0$.

2.3 Te diffusion

Tellurium diffusion coefficient D_{Te} varies reciprocally to P_{Cd} at all temperatures over most of the region of CdTe solid stability [36, 49, 47]. The only exception is the high cadmium pressure region. In [47] pressure dependency of the D_{Te} at 800° was described by:

$$D_{Te} = 1.6 \times 10^{-14} P_{Cd}^{-1} (cm^2/s) \tag{2.11}$$

This equation is in good agreement with the temperature dependencies of the D_{Te} reported by Borsenberger and Stevenson [49]:

$$D_{Te}(P_{Te_2}^{max}) = 1.66 \times 10^{-4} e^{\frac{-1.38eV}{k_B T}} (cm^2/s), \tag{2.12}$$

$$D_{Te}(P_{Te_2}^{min}) = 8.54 \times 10^{-7} e^{\frac{-1.42eV}{k_B T}} (cm^2/s). \tag{2.13}$$

Pressure dependence was described by the relation:

$$D_{Te} = D_{Te_i^0} K_i(T) P_{Te_2}^{1/2}, \tag{2.14}$$

where K_i is the mass action constant for the formation of Te_i^0.

Near cadmium saturated conditions the value of D_{Te} becomes independent of P_{Cd}. Another diffusion mechanism was proposed for this region [36]. Te diffusion has contributions by tellurium interstitial Te_i^- and Te vacancy diffusion mechanisms.

From the equation (2.1) the dependence of the D_{Te} from Cd vapour pressure can be described:

$$D_{Te} = D_{Te_i^0} K_{Te_i^0} P_{Cd}^{-1} + D_{V_{Te}^{2+}} K_{V_{Te}^{2+}} P_{Cd}^{1/3}, \tag{2.15}$$

where $D_{Te_i^0}$, $D_{V_{Te}^0}$ represents the defects diffusivity and $K_{Te_i^0}$, $K_{V_{Te}^0}$ represents the mass action constants for the formation of tellurium interstitial, Te_i^0, and Te vacancy, V_{Te}^{2+}, defects respectively.

2.4 Chemical diffusion in CdTe:Cl

Given a concentration $[X^q]$ of defect X with a charge q, the flux of X^q along the z direction with the diffusion coefficient D_{X}^q is expressed by

$$J_{\mathrm{X}}^q = -D_{\mathrm{X}}^q \frac{\partial [X^q]}{\partial z} + < v_{\mathrm{X}}^q > [X^q]. \tag{2.16}$$

The average velocity $< v_{\mathrm{X}}^q >$ is incurred by an internal electric field induced by charged defects. Using the Nernst-Einstein relation and basic charge defect statistics, J_{X}^q can be simplified to the form [50]

$$J_{\mathrm{X}}^q = -D_{\mathrm{X}}^q \frac{[X^q]}{[X^0]} \frac{\partial [X^0]}{\partial z}. \tag{2.17}$$

The flux of the stoichiometry deviation Δ is obtained as

$$J_\Delta = \sum_{X,q} \frac{\partial \Delta}{\partial [X^0]} J_X^q, \tag{2.18}$$

where

$$\begin{aligned} \Delta = [\mathrm{Cd}] - [\mathrm{Te}] = \left[\mathrm{Cd}_{\mathrm{I}}^0\right] + \left[\mathrm{Cd}_{\mathrm{I}}^+\right] + \left[\mathrm{Cd}_{\mathrm{I}}^{2+}\right] - \\ - \left[\mathrm{V}_{\mathrm{Cd}}^0\right] - \left[\mathrm{V}_{\mathrm{Cd}}^-\right] - \left[\mathrm{V}_{\mathrm{Cd}}^{2-}\right] + \left[\mathrm{Cl}_{\mathrm{Te}}^0\right] + \left[\mathrm{Cl}_{\mathrm{Te}}^+\right]. \end{aligned} \tag{2.19}$$

Chlorine A-centre does not appear in Δ explicitly because it represents both one Cd and one Te atoms missing in the lattice. Combining eqs. (2.17) and (2.18), the chemical diffusion coefficient $\tilde{D}$ is expressed in the form [51]

$$\tilde{D} = -\frac{J_\Delta}{\partial \Delta / \partial z} = \sum_{X,q} D_X^q \frac{[X^q]}{[X^0]} \left| \frac{d[X^0]}{d\Delta} \right|. \tag{2.20}$$

To simplify the calculations, local defect equilibrium and quasi neutral approximation are used as it is commonly done in such systems [50]. The diffusion of Cl is not assumed. Consequently, all defect densities as well as μ_F may be expressed with Cd chemical potential.

Usually, the diffusion flux is mediated by native vacancies and interstitials, for

that $[X^0] \propto P_{Cd}^{\pm 1}$. Equation (2.20) can be than expressed in the form

$$\tilde{D} = \frac{\sum_{X,q} D_X^q [X^q]}{P_{Cd} d\Delta / dP_{Cd}}. \tag{2.21}$$

In compensated CdTe:Cl with V_{Cd}^{2-} dominant diffusing species, $\tilde{D}$ is well approximated with

$$\tilde{D} = \frac{D\left(\mathrm{V}_{Cd}^{2-}\right)\left[V_{Cd}^{2-}\right]}{P_{Cd}\frac{d\left(\left[V_{Cd}^{2-}\right]-\left[Cl_{Te}^{+}\right]+n\right)}{dP_{Cd}}} \approx \frac{D\left(V_{Cd}^{2-}\right)\left[V_{Cd}^{2-}\right]}{P_{Cd} dn/dP_{Cd}}. \tag{2.22}$$

Taking equation (1.23) into account, $\tilde{D} \propto P_{Cd}^{-0.5}$ is predicted for this case.

Chapter 3

Metal-semiconductor junction

Metal-to-semiconductor junctions are of great importance since they are present in every semiconductor device. They can behave either as a Schottky barrier or as an ohmic contact dependent on the character of the interface.

3.1 Energy band diagram

The barrier between the metal and the semiconductor can be identified on an energy band diagram. The energy band diagram of the metal and the semiconductor aligned using the same vacuum level are shown in Figure 3.1. As the metal and semiconductor are brought together, the Fermi energies of the metal and the semiconductor do not change right away. This yields the flatband diagram of Figure 3.2. The barrier height, ϕ_B, is defined as the potential difference between the Fermi energy of the metal and the band edge where the majority carriers reside. As shown in Figure 3.2, for an n-type semiconductor the barrier height is obtained from:

$$\phi_B = \Phi_m - \chi. \tag{3.1}$$

Φ_m is the work function of the metal and χ is the electron affinity of semiconductor. The work function of selected metals as measured in vacuum can be found in Table 3.1. For p-type material, the barrier height is given by the difference between the valence band edge and the Fermi energy in the metal:

$$\phi_B = \frac{E_g}{q} + \chi - \Phi_m \tag{3.2}$$

A metal-semiconductor junction therefore forms a barrier for electrons and holes if the Fermi energy of the metal as drawn on the flatband diagram is set between the conduction and valence band edge.

The built-in potential, ϕ_I, is the difference between the Fermi energy of the metal

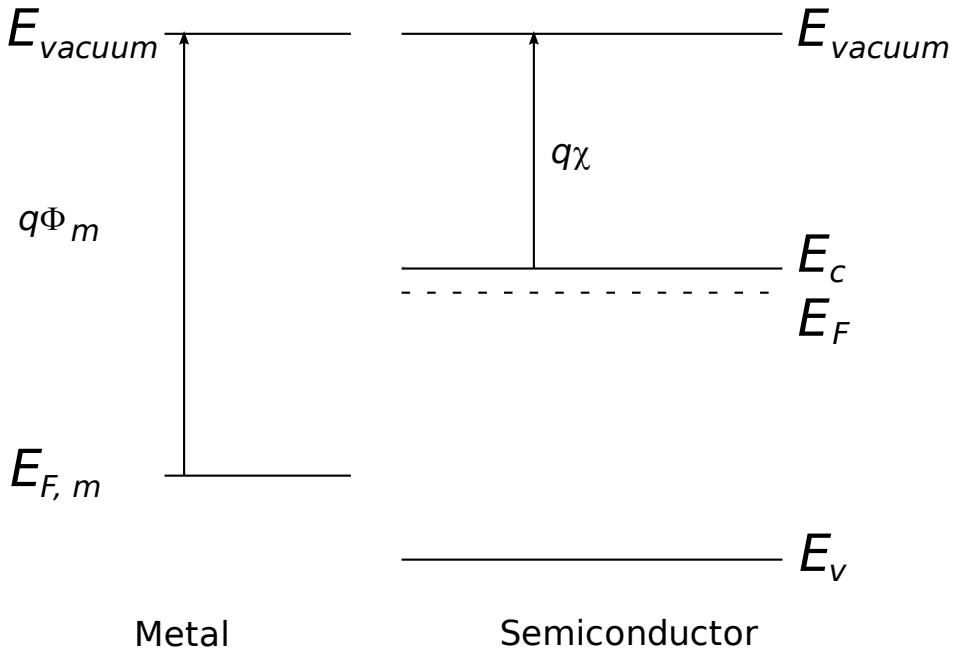

Figure 3.1: Aligned energy band diagrams of metal and semiconductor.

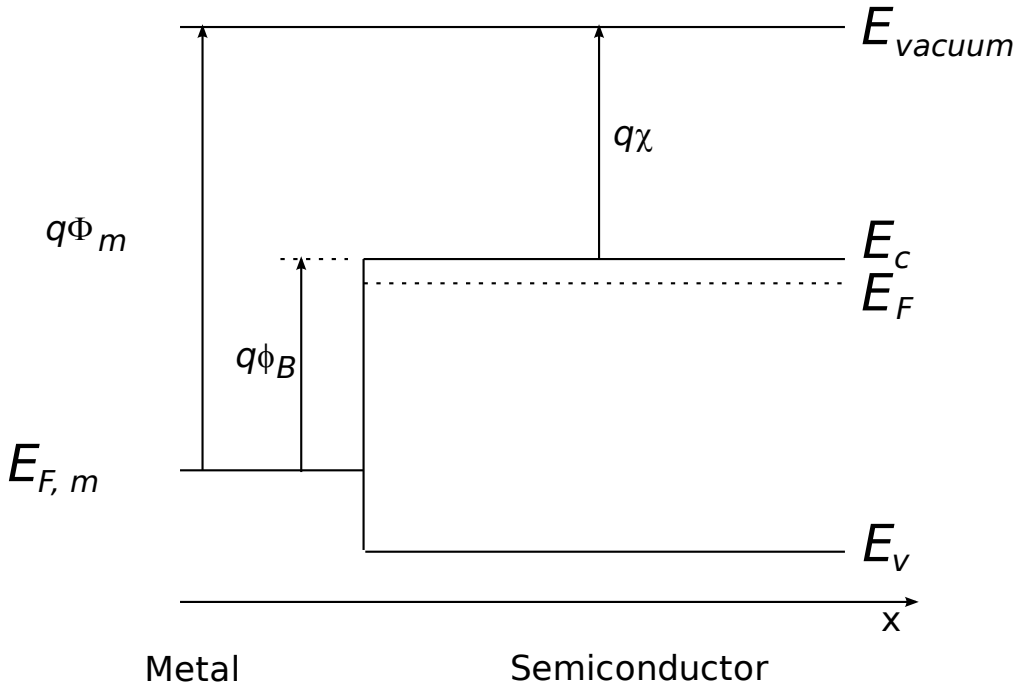

Figure 3.2: Energy band diagram of metal and semiconductor in contact.

Table 3.1: Work functions of selected metals [52]

Metal	Crystallographic direction	Work function ϕ_m, eV
Au	100	4.20
	110	4.06
	111	4.26
Pt	polycrystalline	5.64
	110	5.84
	111	5.93
	320	5.22
	331	5.12
In	polycrystalline	4.09

and that of the semiconductor and can be calculated from:

$$\phi_I = \Phi_m - \chi - \frac{E_c - E_{F,n}}{q} \tag{3.3}$$

and

$$\phi_I = \chi + \frac{E_c - E_{F,p}}{q} - \Phi_m \tag{3.4}$$

for n- and p-type semiconductor, respectively.

The measured barrier height for metal-semiconductor junctions often differs from the ones calculated using (3.1) or (3.2). This is due to the complex behaviour of the metal-semiconductor interface. The ideal metal-semiconductor theory assumes that both materials are infinitely pure, that there is neither interaction between the two materials nor an interface layer. Chemical reactions between the metal and the semiconductor alter the barrier height as do interface states at the surface of the semiconductor and interface layers. Some general trends however can still be observed. As predicted by (3.1) and (3.2), the barrier height on n-type/p-type semiconductor increases/decreases for metals with a higher work function.

3.2 Thermal equilibrium

The flatband diagram, shown in Figure 3.2, is not a thermal equilibrium diagram, since the Fermi energy in the metal differs from that in the semiconductor. Electrons in the n-type semiconductor can lower their energy by traversing the junction. As electrons leave the semiconductor, a positive charge due to ionized donors stays behind. This charge creates an electric field that lowers the band edges of the semiconductor. Electrons flow into the metal until equilibrium is reached between the diffusion of electrons from the semiconductor into the metal and the drift of electrons caused by the field. This equilibrium is characterized by a constant Fermi energy throughout the structure as shown in Figure 3.3.

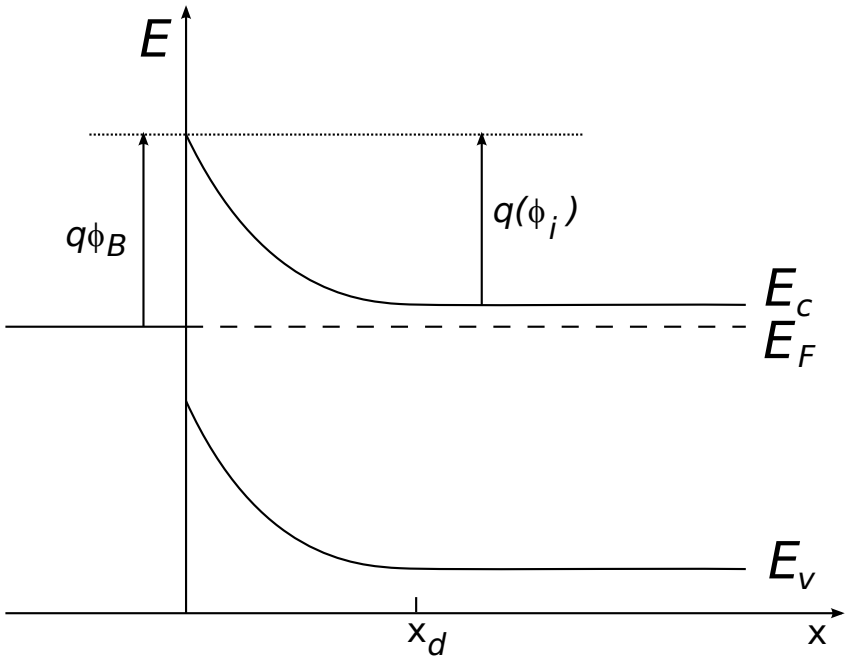

Figure 3.3: Energy band of a metal-semiconductor contact in thermal equilibrium.

It is of interest to note that in thermal equilibrium, i.e. with no external voltage applied, there is a region in the semiconductor close to the junction (x_d), which is depleted of mobile carriers. This region is called the depletion region. The potential across the x_d equals the built-in potential, ϕ_i.

3.3 Forward and reverse bias

Operation of a metal-semiconductor junction under forward and reverse bias (V_a) is illustrated in Figures 3.4 and 3.5, respectively. When a positive bias is applied to the metal (Figure 3.4), the Fermi energy of the metal is lowered with respect to the Fermi energy in the semiconductor. This results in a smaller potential drop across the semiconductor. The balance between diffusion and drift is disturbed and more electrons will diffuse towards the metal than the number drifting into the semiconductor. This leads to a positive current through the junction at a voltage comparable to the built-in potential.

As a negative voltage is applied (Figure 3.5), the Fermi energy of the metal is raised with respect to the Fermi energy in the semiconductor. The potential across the semiconductor now increases, yielding a larger depletion region and a larger electric field at the interface. The barrier, which restricts the flux of electrons from the metal, is unchanged so that the flow of electrons is independent of the applied

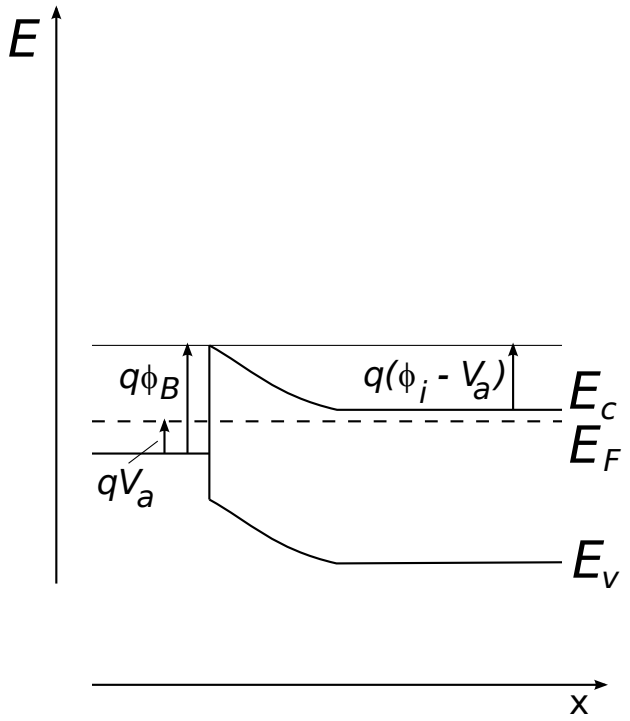

Figure 3.4: Energy band diagram of metal-semiconductor junction under forward bias.

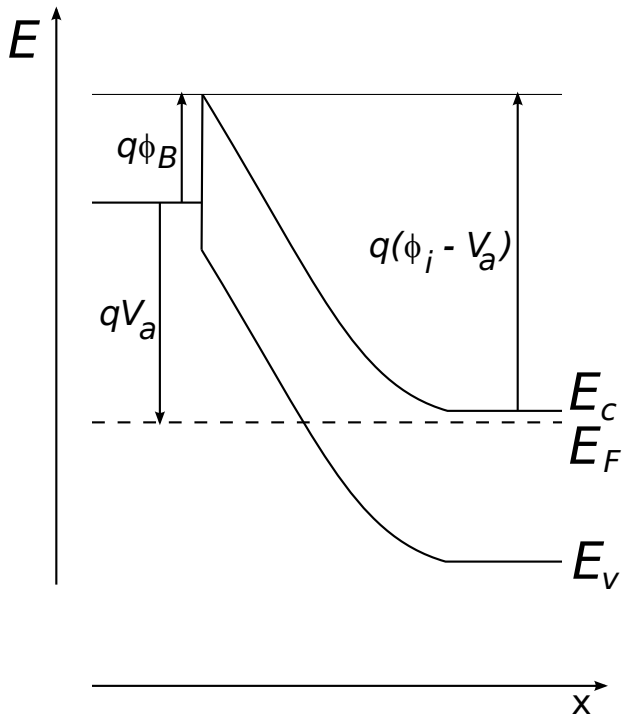

Figure 3.5: Energy band diagram of metal-semiconductor junction under reverse bias.

voltage. The metal-semiconductor junction with positive barrier height has therefore a pronounced rectifying behaviour. A large current exists under forward bias, while almost no current exists under reverse bias.

The potential across the semiconductor equals the built-in potential, ϕ_i, minus the applied voltage, V_a.

$$\phi_{(x=\infty)} - \phi_{(x=0)} = \phi_i - V_a. \tag{3.5}$$

3.4 Poisson equation

The electrostatic analysis of a metal-semiconductor junction is of interest since it provides knowledge about the charge and field in the depletion region. It is also required to obtain the capacitance-voltage characteristics of the contact.

For the general analysis Poisson equation is used:

$$\frac{d^2\phi}{dx^2} = -\frac{\rho}{\epsilon_s} = -\frac{q}{\epsilon_s}(p - n + N_d^+ - N_a^-) \tag{3.6}$$

where, ϵ_s, is semiconductor permittivity, and the charge density, ρ, is written as a function of the electron density, the hole density and the donor and acceptor densities. To solve the equation, the electron and hole density, n and p, must be expressed as a function of the potential, ϕ, yielding:

$$\frac{d^2\phi}{dx^2} = \frac{q}{\epsilon_s}[2n_i \cdot sinh(\frac{\phi}{V_t}) + N_d^+ - N_a^-] \tag{3.7}$$

with

$$\phi = \frac{1}{q}(E_f - E_i), \tag{3.8}$$

$$V_t = \frac{kT}{q}, \tag{3.9}$$

$$n = n_i e^{\frac{\phi}{V_t}}, \tag{3.10}$$

$$p = n_i e^{-\frac{\phi}{V_t}}, \tag{3.11}$$

where E_i is intrinsic Fermi energy, n_i - intrinsic carrier density.

This second-order non-linear differential equation (3.7) can not be solved analytically. Instead, a simplifying assumption is usually made that the depletion region is fully depleted and that the adjacent neutral regions contain no charge.

3.5 Full depletion approximation

The simple analytic model of the metal-semiconductor junction is based on the full depletion approximation. This approximation is obtained by assuming that the semiconductor is fully depleted over a distance x_d, called the depletion region. While

this assumption does not provide an accurate charge distribution, it provides very reasonable approximate expressions for the electric field and potential throughout the semiconductor.

To apply the full depletion approximation to an M-S junction on n-type semiconductor, the depletion region is defined to be between the metal-semiconductor interface ($x = 0$) and the edge of the depletion region ($x = x_d$).

To find the depletion layer width, the electric field and the potential across the semiconductor should be calculated as a function of the depletion layer width. Requiring the potential across the semiconductor to equal the difference between the built-in potential and the applied voltage, $\phi_i - V_a$, depletion layer width can be found.

As the semiconductor is depleted of mobile carriers within the depletion region, the charge density in that region is due to the ionized donors. Outside the depletion region, the semiconductor is assumed neutral. This yields the following expressions for the charge density, ρ:

$$\rho(x) = qN_d,\ for\, 0 < x < x_d \tag{3.12}$$

$$\rho(x) = 0,\ for\, x \geq x_d \tag{3.13}$$

where full ionization is assumed so that the ionized donor density equals the donor density, N_d. This charge density is shown in Figure 3.6. The charge in the semiconductor is exactly balanced by the charge in the metal, Q_M, so that no electric field exists except around the metal-semiconductor interface.

Using Gauss's law we obtain electric field as a function of position, also shown in Figure 3.7:

$$\varepsilon(x) = \frac{qN_d}{\epsilon_s}(x_d - x),\ for\, 0 < x < x_d \tag{3.14}$$

$$\varepsilon(x) = 0,\ for\, x \geq x_d \tag{3.15}$$

where ϵ_s is the dielectric constant of the semiconductor. The electric field is assumed to be zero outside the depletion region. It is expected to be zero there since a non-zero field would cause the mobile carriers to redistribute until there is no field. The depletion region does not contain mobile carriers so that there can be an electric field. The largest (absolute) value of the electric field is obtained at the interface and is given by:

$$\varepsilon(0) = -\frac{qN_d x_d}{\epsilon_s} = -\frac{Q_d}{\epsilon_s} \tag{3.16}$$

where the electric field was also related to the total charge (per unit area), Q_d, in the depletion layer. Since the electric field is minus the gradient of the potential, one obtains the potential by integrating the expression for the electric field, yielding:

$$\phi(x) = 0,\ for\, x \leq 0 \tag{3.17}$$

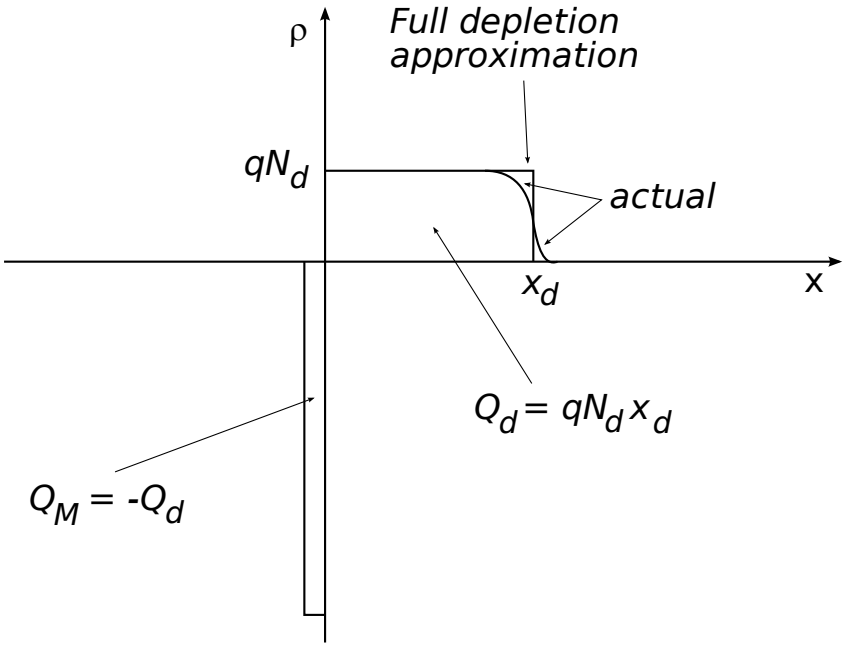

Figure 3.6: Full depletion approximation charge density.

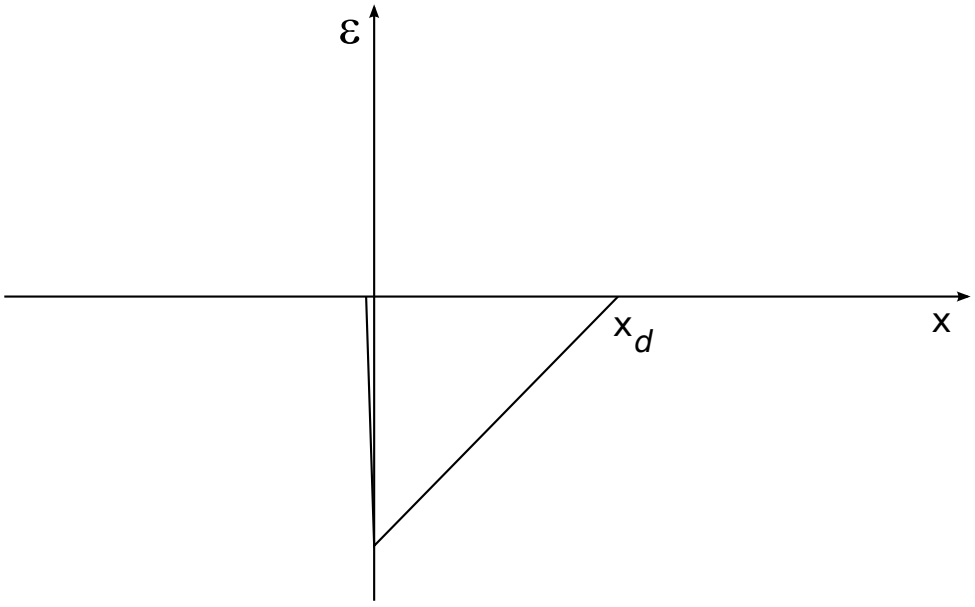

Figure 3.7: Full depletion approximation electric field.

$$\phi(x) = \frac{qN_d}{2\epsilon_s}[x_d^2 - (x_d - x)^2],\ for\, 0 < x < x_d \tag{3.18}$$

$$\phi(x) = \frac{qN_d x_d^2}{2\epsilon_s},\ for\, x > x_d \tag{3.19}$$

The potential across the metal can be neglected. Since the density of free carriers is very high in a metal, the thickness of the charge layer in the metal is very thin. Therefore, the potential across the metal is several orders of magnitude smaller than that across the semiconductor, even though the total amount of charge is the same in both regions.

The total potential difference across the semiconductor equals the built-in potential, ϕ_i, in thermal equilibrium and is further reduced/increased by the applied voltage when a positive/negative voltage is applied to the metal as described by equation (3.5). This boundary condition provides the following relation between the semiconductor potential at the surface, the applied voltage and the depletion layer width:

$$\phi_i - V_a = -\phi_{(x=\infty)} = \frac{qN_d x_d^2}{2\epsilon_s}. \tag{3.20}$$

Solving this expression for the depletion layer width, x_d, yields:

$$x_d = \sqrt{\frac{2\epsilon_s(\phi_i - V_a)}{qN_d}}. \tag{3.21}$$

3.6 Schottky diode current

The current across a metal-semiconductor junction is mainly due to majority carriers. Three distinctly different mechanisms exist: diffusion of carriers from the semiconductor into the metal, thermionic emission of carriers across the Schottky barrier and quantum-mechanical tunnelling through the barrier. The diffusion theory assumes that the driving force is distributed over the length of the depletion layer. The thermionic emission theory on the other hand postulates that only energetic carriers, those, which have an energy equal to or larger than the conduction band energy at the metal-semiconductor interface, contribute to the current flow. Quantum-mechanical tunnelling through the barrier takes the wave-nature of the electrons into account, allowing them to penetrate through thin barriers. In a given junction, a combination of all three mechanisms could exist. However, typically only one mechanism limits the current, being denoted as the dominant current mechanism.

3.6.1 Diffusion current

This model assumes that the depletion layer is large compared to the mean free path, so that the concepts of drift and diffusion are valid. The resulting current

density equals:

$$J_n = \frac{qD_nN_c}{V_t}\sqrt{\frac{2q(\phi_i - V_a)N_d}{\epsilon_s}}e^{-\frac{\phi_B}{V_t}}[e^{\frac{V_a}{V_t}} - 1] \tag{3.22}$$

The current therefore depends exponentially on the applied voltage, V_a, and the barrier height, ϕ_B. The pre-factor can more easily be understood if one rewrites it as a function of the electric field at the metal-semiconductor interface, ε_{max}:

$$\varepsilon_{max} = \sqrt{\frac{2q(\phi_i - V_a)N_d}{\epsilon_s}} \tag{3.23}$$

resulting:

$$J_n = q\mu_n N_c \varepsilon_{max} e^{-\frac{\phi_B}{V_t}}[e^{\frac{V_a}{V_t}} - 1] \tag{3.24}$$

so that the pre-factor equals the drift current at the metal-semiconductor interface.

3.6.2 Thermionic emission

The thermionic emission theory assumes that electrons, which have an energy greater than the top of the barrier, will cross the barrier provided they move towards the barrier. The actual shape of the barrier is hereby ignored. The current density can be expressed as:

$$J_{s\to m} = A^*T^2e^{-\phi_B/V_t}(e^{V_a/V_t} - 1) \tag{3.25}$$

where $A^* = \frac{4Rqm^*k^2}{h^3}$ is the Richardson constant and ϕ_B is the Schottky barrier height.

The expression for the current due to thermionic emission can also be written as a function of the average velocity with which the electrons at the interface approach the barrier. This velocity is referred to as the Richardson velocity given by:

$$\nu_R = \sqrt{\frac{kT}{2\pi m}}, \tag{3.26}$$

so that the current density becomes:

$$J_n = q\nu_R N_c e^{-\frac{\phi_B}{V_t}}[e^{\frac{V_a}{V_t}} - 1] \tag{3.27}$$

This expression states that the current is the product of the electronic charge, q, the velocity, ν, and the density of available carriers in the semiconductor located next to the interface. The velocity equals the mobility multiplied with the field at the interface for the diffusion current and the Richardson velocity for the thermionic emission current. The minus one term ensures that the current is zero if no voltage is applied as in thermal equilibrium any flux of carriers is balanced by a flux of carriers in the opposite direction.

3.6.3 Tunnelling

The tunnelling current is obtained from the product of the carrier charge, velocity and density. The velocity equals the Richardson velocity, the velocity with which on average the carriers approach the barrier. The carrier density equals the density of available electrons, n, multiplied with the tunnelling probability, Θ, yielding:

$$J_n = q\nu_R n\Theta, \tag{3.28}$$

where ν_R is the Richardson velocity and n is the density of carriers in the semiconductor. The tunnelling probability term, Θ, is obtained from:

$$\Theta = e^{(-\frac{4}{3}\frac{\sqrt{2qm^*}}{\hbar}\frac{\phi_B^{3/2}}{\varepsilon})}, \tag{3.29}$$

and is added since the total current depends on the carrier flux arriving at the tunnel barrier multiplied with the probability, Θ, that they tunnel through the barrier. The tunnelling current therefore depends exponentially on the barrier height, ϕ_B, to the 3/2 power.

Chapter 4

Surface chemical treatment

Chemical etching is widely used on different stages of semiconductor device preparation [53, 54, 55]. Around 70 etching solutions, both selective and non-selective, are currently used for surface treatment of CdTe and substitutional solid solution alloys, mainly (CdZn)Te, based on it. Most of them were developed for the elementary and $A^{III}B^{V}$ semiconductors. It was reported [56, 57, 58] that chemical treatment strongly influences device electrical properties.

Etching solutions differ by the etching speed, roughness and stoichiometry of obtained surface, contamination of the surface layer with solution components, etc.

Etching process is strongly influenced by various conditions like temperature of the etching solution, speed of the etchant flux, previous surface treatment and material purity.

One of the possible classification of etching solutions is by the power of oxidant.

4.1 Etching compositions with bromine

Bromine is one of the most frequently used oxidants in etching compositions for the surface treatment of $A^{II}B^{VI}$ type semiconductor compounds [57]. It is because of:

- bromine is much softer oxidant than Cr^{+6} and H_2O_2 [53]
- bromides, obtained as a products of the oxidation process, are well soluble in water
- oxidation products form a layer on the treated surface which allows to precisely control reaction speed.

Solutions of elementary bromine in organic and inorganic solvents (methanol (CH_3OH), ethanol (C_2H_5OH), dimethylformamide ($(CH_3)_2NC(O)H$), hydrobromic acid (HBr)) are basically used for etching of $A^{II}B^{VI}$ type semiconductors. Bromine interacts with the solvent, hence nature of the last one influences speed and character of the surface treatment process.

The bromine concentration in solutions decreases gradually during preservation even in a closed flask. pH of the solution decreases as well. Ethanol is oxidized by the bromine:

$$C_2H_5OH + 2Br_2 + H_2O \leftrightarrow CH_3COOH + 4HBr. \tag{4.1}$$

Preservation of bromine-methanol solutions has the same problem.

As a result of surface treatment in bromine-methanol 0.5 % solution with illumination sub-lattice limits are well defined on all planes for both $CdTe$ and $Cd_{1-x}Zn_xTe$ [59]. Etching in the same solution without illumination forms a big concentration of cadmium vacancies ($1 - 4 \times 10^{14}\, cm^{-3}$) on the surface [60]:

$$CdTe + Br_2(CH_3OH) \leftrightarrow CdBr_2(CH_3OH) + Te, \tag{4.2}$$

which can be removed electrochemically [61].

Tellurium layer formation on the CdTe surface after etching in 5 % Br-methanol solution was experimentally determined by the Raman spectroscopy [62] and Auger electron spectroscopy [63]. Layer thickness was found to be 1-4 nm. CdTe and CdZnTe surface etched in 2 % bromine-methanol solution is also enriched with tellurium [64, 65, 66]. Similar results are reported in [67, 68], where after two minutes etching in 1 % bromine-methanol solution Cd/Te ratio is 0.43. Surface treatment in 0.02 % Br_2 solution in CH_3OH forms 0.5-0.7 nm thick amorphous tellurium layer [69, 70]. However, washing in $NaBH_4$ decreases layer thickness to 0.25 nm. Maximum tellurium layer thickness is reported [67] to be as big as 40 Å depending on bromine concentration and etching time.

After $30\, s$, etching in bromine-methanol solution with 1 : 1 volume ratio a tellurium dioxide was found on the $CdTe$ surface along with tellurium. Cd/Te ratio was 1.59. Heating in the vacuum to the $723\, K$ helped to remove some amount of TeO_2 [60]. Etching CdTe in 10 % bromine-methanol solution forms on its surface $3 - 10\, nm$ thick cadmium enriched layer ($Cd/Te = 1.58$). Tellurium is oxidized only in the upper part of the layer ($1 - 2\, nm$) and its composition is TeO_x ($x \to 0$). Thus, after etching a heterostructure is formed on the CdTe surface. Roughly its structure is: insulating layer ($0.5 - 2\, nm$ thick, $Cd + TeO_x$ + impurities), conductive layer ($6 - 10\, nm$ thick, $Cd + Te$), crystal volume [71].

In [72] layers formed on the $CdTe$ surface after etching in 12 % bromine-methanol solution were investigated by means of secondary mass-spectrometry (SIMS), Rutherford back scattering and ellipsometry. It was found, that just etched surfaces are slightly oxidized, enriched with Cd, Cd/Te ratio is 1.58. Surface layer thickness is ~ 10 Å, but in the atmosphere it increases with time. Increasing Te concentration on the surface is explained by its diffusion from the sample volume.

Investigation of the CdTe surface etched in Br_2-methanol and Br_2-butanol showed, that mainly cadmium is washed out as a result of Cd^{2+} and Br^- interaction. When the cadmium concentration reaches a critical value, structural changes occur, and tellurium precipitates are formed. TeO_2 is formed on such surface in water presence.

It is reported [73, 74], that $20\,min.$ washing in methanol totally removes Br_2 from the CdTe surface etched in 0.1 % bromine-ethanol solution, and Cd/Te ratio decreases from 0.7 to 0.5. X-ray photoelectron spectroscopy (XPS) analysis showed a presence of $TeBr_4$ purely soluble in this solution. Bromine absorbed on the surface can diffuse into the volume.

XPS results for the $Cd_{0.2}Hg_{0.8}Te$ surface etched in 0.001 % Br_2-CH_3OH solution are reported in [75]. Extremely small bromine concentration allows to etch with the speed $\sim 0.1\,nm/s$. Chemical-mechanical polishing produce smooth surface with surface composition close to that of the bulk material. The resultant surface can be approximated as $0.8\,nm$ $Hg_{0.6}Te/Hg_{0.8}Cd_{0.2}Te$.

P-type $CdTe$ surface composition after etching in some solutions containing bromine were investigated by the XPS [76]. It was found, that 1 % bromine-methanol solution gives $Cd/Te = 0.7$ ratio after $2\,min.$ etching; 1 % Br_2-CH_3OH + 1M KOH after $2\,min$ treatment gives Cd/Te=0.67 ratio; 1 % bromine-methanol + hydrazine after $2\,min$ treatment with the following cleaning in the $0.5\,N$ $Na_2S_2O_3$ + 2M NaOH in deionized water at $80 - 90°\,C$ gives Cd/Te=0.87 ratio; 1 % bromine-methanol + hydrazine after $2\,min$ treatment with the following cleaning in hydrazine ($\sim 3\,min$) gives Cd/Te=0.85 ratio. TeO_2 layer was present after all treatments, since samples were kept in the atmosphere.

CdTe surface preparation quality is critical for the device fabrication [77]. When adding lactic acid to the bromine-methanol solution, the quality of x-ray and gamma ray detectors improves [78]. After mechanical treatment with Al_2O_3 abrasive powder (grain size 0.5 μm) and ultrasound cleaning in acetone, samples were etched in 5 % bromine-methanol solution [79] or in 2 % Br_2 in 20 % lactic acid solution in ethylene glycol [80]. After the etching samples were cleaned in CH_3OH. Etching speed of n-type $Cd_{1-x}Zn_xTe$ (x = 0.1 - 0.2) in 2-10 % bromine solution in methanol was $50\,\mu m/min$ at room temperature [81]. Etching time and removed layer thickness are also very important parameters for the x-ray and gamma ray detector preparation [82]. It was found that etching in bromine-ethylene glycol solutions for 6 min. is optimal and significantly improves device properties.

4.2 Etching compositions with iodine

It is possible to use etching compositions containing iodine for the purpose of polishing and etching of the CdTe surfaces.

Surface treatment of the $Cd_{1-x}Zn_xTe$ was studied in detail in [83]. It was per-

formed in the aqueous solution containing 0.2 % I_2 and 4 % NaI at room temperature. Etching quality was judged by the surface look. XPS measurements were done to define surface composition. Cd/Te ratio was found to be 0.36 which shows that surface layer is significantly tellurium enriched.

It is generally known that polishing quality of the solution increases with the increase of its viscosity. In order to obtain good quality polished surfaces of the $Cd_xHg_{1-x}Te$ ethylene glycol was added to the etching solution [84]. It was shown that treatment in I_2-KI aqueous solution with ethylene glycol gives high quality $Cd_xHg_{1-x}Te$ surface. Detailed study of the etching process for the CdTe, HgTe, $Cd_xHg_{1-x}Te$ surfaces in the I_2-KI-HBr aqueous solutions was done in [85, 86, 87]. Presence of ethylene glycol in the solution gradually decreases etching speed. Etching speed is also proportional to the iodine concentration [86]. This allows to control etching process precisely.

$Cd_{1-x}Zn_xTe$ surface etching can be made in solution containing KIO_3 [88]. Solution also contained lactic acid to decrease pH and increase chemical reaction speed. XPS analysis showed smaller deviation from the stoichiometry in comparison with using bromine-methanol solutions.

Adding organic acids into the etching solutions increases polishing effect. In order to modify solution properties various acids (lactic $C_3H_6O_3$, tartaric $C_4H_6O_6$, citric $C_6H_8O_7$) were added to the H_2O_2-HI system [89]. Direct reaction speed dependence on the acid concentration was confirmed.

4.3 Etching compositions with nitric acid

Nitric acid is used in etching compositions for the CdTe and in combination with CrO_3, $K_2Cr_2O_7$, H_2SO_4. HNO_3 acts as oxidant. Redox process has few stages [90]:

$$HNO_2 + HNO_3 \leftrightarrow 2NO_2 + H_2O, \tag{4.3}$$

$$NO_2 + e^- \leftrightarrow NO_2^-, \tag{4.4}$$

$$NO_2^- + H^+ \leftrightarrow HNO_2. \tag{4.5}$$

HNO_3 redox reaction is auto-catalytic, hence equations (4.3)-(4.5) correspond to the equilibrium state where needed HNO_2 concentration is already present in the solution [91, 92]. Despite of good solubility of all etching reaction products, HNO_3 is considered [91] to be not the best oxidant because of auto-catalytic character of the process and huge nitrogen oxide gas emission.

Nitric acid forms on the $Cd_xHg_{1-x}Te$ thin layer of mercury compounds and can be used for the Te layer removal formed after etching in bromine-methanol solution. After 2 min. treatment in HNO_3 tellurium layer was found on the surface [93]. Layer thickness was reported to be $\sim 50\,nm$. Since the crystal structure of Te is different

from that of CdTe, the action of acid is not simply a "leaching" of Cd atoms, leaving a Te matrix. Instead, there is apparently a recrystallization, or epitaxy, from the liquid [93].

XPS measurement shows a formation of the layer consisting of TeO_2 and Te after washing in concentrated HNO_3 [94]. Auger electron spectroscopy and XPS measurements did not show cadmium presence in the surface layer after etching in 15 % nitric acid [95]. Te layer thickness was estimated to be 60-80 nm [96].

Surface layer on the p-type CdTe has about 100 times smaller resistivity than the volume and its thickness reaches $500\,nm$ [97]. Etching in the solutions containing $HNO_3 + H_3PO_4 + H_2O$ leads to the surface enrichment with tellurium and increasing solar cell sensitivity ($\sim$12.5 %) on the structures CdTe-Sb/Au, which is much better than after treatment in bromine-methanol solution [73].

To visualize structure defects in the semiconductor single-crystals (dislocations, twins, point defects, inclusions, etc.) selective etching is used. It is based on etching speed variation for different crystallographic directions.

In [98] dislocations were detected by chemical etching. Before etching samples were mechanically polished by $1\,\mu m$ Cr_2O_3 and chemically polished in 1 % bromine-methanol solution, dissolving more than $20\,\mu m$ to remove the damaged layer. After that the samples were etched in the solution: $60\,vol.part$ H_2O, $1\,vol.part$ Cr-acid, $1\,vol.part$ concentrated HNO_3, $1\,vol.part$ concentrated HF. The etch pits produced by the etchant were proven to be due to dislocations by correlating to each pit patterns with X-ray reflection topography and by deformation experiments.

Etching with chromic acid ($Na_2Cr_2O_7$ in 3M HNO_3) increases the open-circuit photovoltage as observed on the polished but not etched crystal, and increases the short-circuit photocurrent density. It also reduces the surface defect concentration as recorded by two-beam photocurrent spectroscopy [99].

In [100] one of the most widely used polishing etching solutions for cadmium telluride was proposed - solution E (20ml HNO_3 + 10ml H_2O + 4g $K_2Cr_2O_7$). Mechanism for the CdTe etching in E solution is proposed in [101, 102]: NO_2^- interacts mainly with Cd, $Cr_2O_7^{2-}$ oxidises Te to insoluble TeO_2, which is oxidized by nitric acid to a soluble compounds. After treatment in E solution some amount of chromium is reported to remain on the surface [103]. Cd/Te ratio in the surface layer is 0.08 [96], layer thickness is $30 - 60\,nm$. From the XPS measurements [104] results the concentration peaks ratio Te/Cd > 9, and tellurium in the surface layer is in oxidation state Te^{+4}. After etching in this solution it is possible to define (111) crystallographic direction on n-type CdTe by the etching pits [105, 106] and Cd and Te sub-latices surfaces.

It is reported [107] that surface layer formed by etching in E solution consists of Te and TeO_2 and can gradually debase optical properties of the CdTe based devices.

4.4 Etching compositions with hydrogen peroxide

Because of strong oxidizing properties hydrogen peroxide (H_2O_2) is used for CdTe etching only in a mixture with strong complex-forming agents, such as HF. Usage of HF is motivated by the stability of 30 % H_2O_2 solution in such mixtures.

Cadmium telluride surface treated in solution 2 vol.part H_2O_2 + 3 vol.part HF + 1 vol.part H_2O has 60-80 nm thick tellurium enriched surface (Cd/Te=0.2) [96]. Etching solution 2 vol.part H_2O_2 + 3 vol.part HF + 1 vol.part H_2O is used for the (111) CdTe surface identification and dislocation density study [108, 59]. After etching of single-crystals $Cd_{0.96}Zn_{0.04}Te$ in the solution with composition 200ml HF + 400 ml H_2O_2 + 400 ml H_2O, grown steps were found on the surface (110) [109].

Surface layer formed by etching in solutions containing H_2O_2 were analysed by the non-destructive spectroscopic ellipsometry [69]. It was found, that oxide layer is not a mechanical mixture of CdO and TeO_2, but a chemical compound, possibly $CdTeO_3$ or Cd_2TeO_5. It was established, that products solubility greatly depends on solution pH, thus it is possible to control layer composition by changing pH.

SIMS analyses showed TeO, TeO_2 and TeO_3 presence in significant amount on the surface etched in heated solution with composition 4 vol.part H_2O_2 + 1 vol.part NH_4OH [72]. Presence of TeO_3 peak is explained by its forming from more complex compounds like $CdTeO_3$. Layer thickness is estimated to be 70-80 nm, and its refraction index is ∼2 (close to that of TeO_2). Additional oxidizing does not increase thickness, but changes refraction index to 2.2.

Solution with composition 1 *vol.part* HF + 1 *vol.part* H_2O_2 + 1 *vol.part* CH_3OH was used to identify twins, inclusions and dislocation on CdTe surface [66].

4.5 Etching compositions with bases

For the preparation of the photovoltaic devices based on CdTe an etching in bases is used. This process removes tellurium oxides layer formed during etching in solutions with acids. It is known that at $pH = 14$ elementary chalcogens react by the following equation:

$$4X + O_2 + 8OH^- \leftrightarrow 2XO_3^{2-} + 4H_2O + 2X^{2-} \tag{4.6}$$

It is reported [60], that at $pH = 14$ tellurium is reducted:

$$Te^0 + e^- \leftrightarrow 1/2Te_2^{2-}. \tag{4.7}$$

This process goes only if electric field is applied. Only electrochemical reduction allows to remove peaks caused by tellurium layer presence. Simple etching in NaOH solution does not help to remove surface film. Electrochemical reduction of CdTe in 1M KOH besides removing tellurium layer decreases cadmium vacancies concentration. Auger spectroscopy shows that $0.7\,nm$ thick surface layer on the CdTe surface

after reduction in Na_2SO_4 + NaOH is enriched by cadmium (Cd/Te=1.42) [95]. Etching speed in this solution is $1.2\,\mu m/min$ [96].

It should be mentioned, that in basic solution the surface oxidation can occur as well. In order to obtain $TeO_2/Cd_xHg_{1-x}Te$ heterostructure it was recommended to oxidise plate surfaces in mixture of $K_2Fe(CN)_6$ and KOH.

Chapter 5

Experiment

5.1 Crystal growth

CdTe crystals were grown in our laboratory, in the Institute of Physics of Charles University (Prague, Czech Republic). Growth was performed by a two-step method. Initially polycrystalline CdTe was synthesized from component materials and doping element. After that it was melted and recrystallized into single-crystalline ingot.

Synthesis of the material

Cadmium and tellurium for crystal preparation were commercially purchased (Nippon Mining & Metals Co., Ltd., Japan). Materials purity was 6N (Table 5.1). Materials were loaded into the quartz ampoule in equiatomic relation. Walls of ampoule were graphite covered to prevent crystal contamination. Ampoule was evacuated out to the vacuum level better than $10^{-3}\,Pa$ and sealed. It was encapsulated in the ampoule with bigger diameter to prevent material oxidation in case of accidental crash of the main ampoule.

For the synthesis a horizontal furnace with $40\,cm$ long working zone with uniform temperature was used. Synthesis process requires a special temperature scheduler to prevent ampoule explosion. The major part of the mixed material interacts and forms CdTe at $750^\circ\,C$, but the synthesis starts at $450^\circ\,C$ when Te melts. Reaction between cadmium and tellurium is exothermic. Thus, rapid temperature increase may occur. This would result in a huge cadmium partial pressure and consequent ampoule explosion. For this reason the temperature increase was restricted to the $0.5^\circ\,C/min$.

Synthesized CdTe was molten and held in that state for 10 hours at temperature $1115^\circ\,C$ for homogenization. Melt was solidified at a cooling rate $0.1^\circ\,C/min$ down to $1085^\circ\,C$ when all material becomes solid. After that the ampoule was cooled down to the room temperature without temperature control. Obtained ingot was extracted from the ampoule and used as a source for CdTe single crystal growth.

Table 5.1: Standard specifications of the used material (ppm wt) [110]

impurity	Cd	Te
Zn	< 0.1	-
Fe	< 0.1	< 0.05
Ni	< 0.01	< 0.1
Ag	< 0.03	< 0.01
Tl	< 0.01	-
Pb	< 0.01	< 0.02
Bi	< 0.01	< 0.05
Cu	< 0.01	< 0.02
Sn	< 0.1	< 0.01
Na	-	< 0.05
Mg	-	< 0.01

Growth of the crystal

Crystals used in this study were grown using different techniques. The crystal $F2421$ was obtained by the VGF and doped with chlorine on the level of $5 \times 10^{18}\, cm^{-3}$. The crystal $B4339$ was grown by VB and doped with indium on the level of $5 \times 10^{15}\, cm^{-3}$. Detailed description of these methods is given in Section 1.3.

Crystal $F2421$ was grown in boron nitride (BN) crucible to prevent contamination from ampoule walls. Crucible diameter was 100 mm. Polycrystalline CdTe was crashed into pieces and loaded into it. Crucible and cadmium for pressure control were loaded into the quartz ampoule. Then the ampoule was evacuated to the vacuum better than $10^{-3}\, Pa$ and sealed off. VGF furnace had two zones, one for the crystal and second for the Cd to control vapour pressure inside the ampoule. The source material was heated to the temperature higher than its melting point and held in molten state for a period of 12 hours for homogenization and equilibration with the vapour. The growth of single-crystal was performed by cooling of the melt from $1115^\circ\, C$ to $1085^\circ\, C$ with the speed $0.5^\circ\, C/h$. Cadmium overpressure was kept at $1.2\, atm$ for the whole period. Temperature gradient in the furnace was $\sim 5^\circ\, C/cm$.

Crystal $B4339$ was grown by the vertical modification of Bridgman technique. Crashed polycrystalline material together with additional cadmium were loaded into the quartz ampoule. Inner walls were covered with graphite. Ampoule diameter was $45\, mm$. Crystal zone was heated to the $1115^\circ\, C$ and kept for 10 hours for homogenization. Cd zone temperature was chosen to have cadmium overpressure of $1.2\, atm$. Crystal growth was performed by mechanical moving of the ampoule across the temperature gradient with the speed $3\, mm/h$ until all the material was solid.

Post-growth annealing at $800^\circ\, C$ was done to prevent the cracking of the ingot

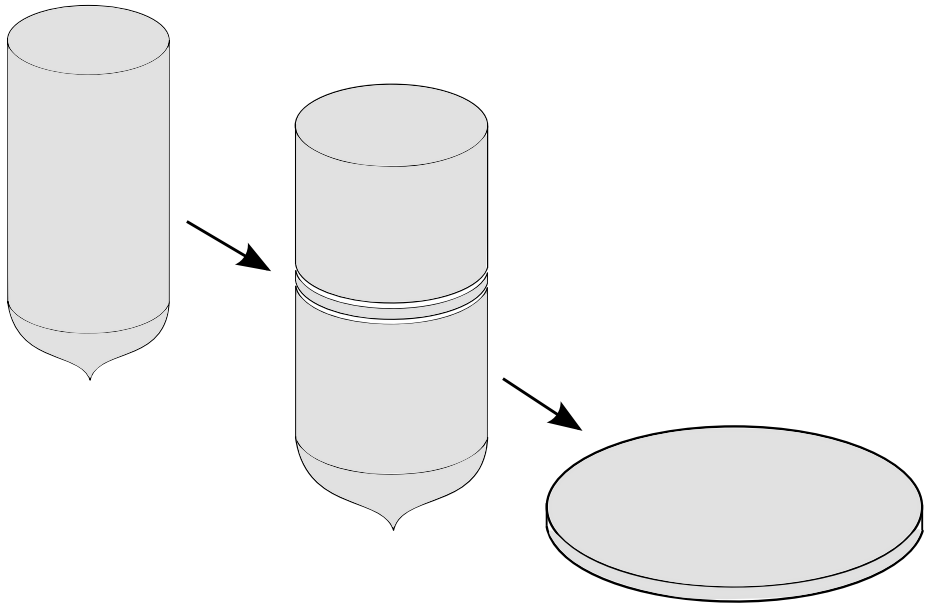

Figure 5.1: Fabrication of thin wafers from *as-grown* single crystals. Ingots are cut in the axis perpendicular to the growth direction using diamond wire saw "Well 6234".

and to improve its structural properties.

5.2 Sample preparation

Samples with dimensions $5 \times 5 \times 1.6$ mm were used for the measurements. They were obtained from the CdTe single crystal ingots by the multi-step process involving cutting, grinding, polishing and etching.

CdTe single crystals were cut at right angle to the growth direction as shown in Figure 5.1. Cutting was done with a commercially purchased diamond wire saw (Well Diamond Wire Saws, Inc., Model 6234). Wire with $0.3\,mm$ diameter was used. Thickness of the wafers was $2\,mm$. Cutting process introduces defects into the surface layer. In order to remove them wafers were ground. For grinding boron carbide (B_4C) abrasive was used. It was mixed with water and glycerine. Wafers were ground first with powder F600 (grain size $10\,\mu m$) and after that with F1000 (grain size $6\,\mu m$).

CdTe wafers were cut with diamond wire saw (Well Diamond Wire Saws, Inc., Model 3242) into square samples with dimensions $5 \times 5\,mm$ as shown in Figure 5.2. Diameter of the wire was $0.3\,mm$.

Samples were chemically-mechanically polished in 3% Br_2-ethylene-glycol solution on the silk cloth. Process was performed at room temperature for 3 minutes for each side. Removed layer thickness was 100 μm.

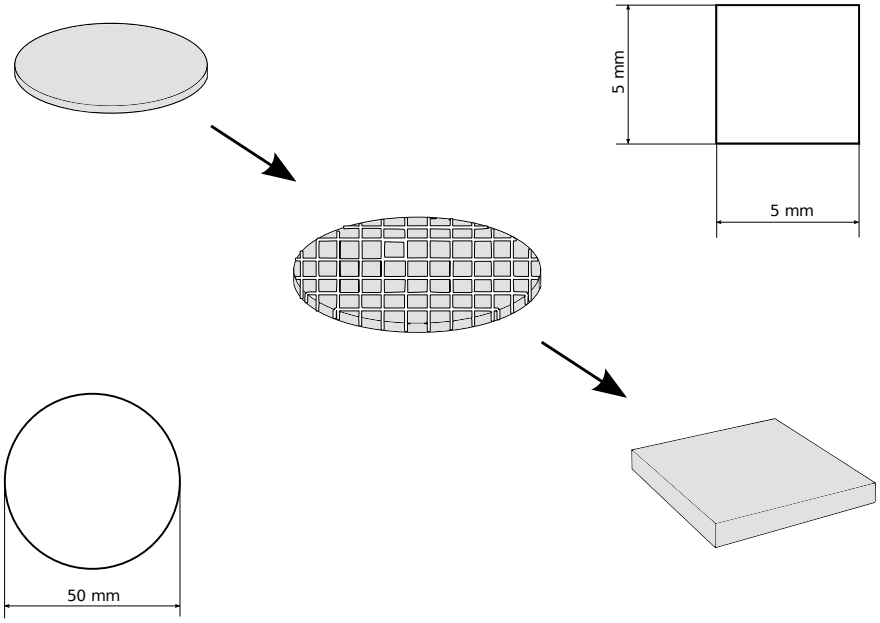

Figure 5.2: Preparation of samples. Wafers are cut on squares with diamond wire saw "Well 3242".

Chemical etching in 3% Br_2-methanol solution at room temperature for 1 minute was the final step of the sample preparation. Measured thickness of the removed layer was 14 μm.

After each process the surface was contaminated with different substances. In case of cutting there were residues of CdTe itself, in grinding - abrasive powder, in polishing and etching - products and reagents of the chemical reaction. Complex washing was used to remove them. Washing was performed in distilled water, after that in ethanol, next in acetone and finally samples were dried in the clean air flow.

5.3 Surface treatment

5.3.1 Etching techniques

Samples were chemically etched in various solutions to obtain surfaces with different chemical composition, oxide thickness, roughness and electrical properties. Three main solutions were: "classical" bromine in methanol; solution emitting bromine based on HBr and HNO_3; and non-bromine solution with HI and hydrogen peroxide:

- **Br - solution**
  Standard 3% solution of bromine in methanol.
  Used at room temperature immediately after mixing

- **HBr - solution**

HNO_3 + HBr + $C_4H_6O_6$
Solution needed to be left for 2 hours after mixing. Used at room temperature

- **HI - solution**
  H_2O_2 + HI + $C_6H_8O_7$
  Solution needed to be left for 2 hours after mixing. Used at room temperature.

Etching was performed using rotation equipment. Samples were submerged in the solution and rotated with the speed 90 rotations per minute. Sample thickness was checked before and after etching to define process speed. After the etching the surface was cleaned in ethanol, acetone and distilled water. Finally, it was dried in the flow of warm air.

5.3.2 Surface roughness study

The surface roughness of the samples was measured by means of a noncontact 3D surface profiler (Zygo NewWiew 5000, USA), pictured in Figure 5.3. This microscope uses noncontact scanning white-light interferometry to acquire ultrahigh Z-resolution images. The measurement is based on the interferometry - a traditional technique in which a pattern of bright and dark lines (fringes) results from an optical path difference between the reference and sample beams. Incoming light is split inside an interferometer, one beam going to an internal reference surface and the other to measured sample. After reflection, the beams recombine inside the device, undergoing constructive and destructive interference and producing the light and dark fringe pattern.

5.4 Contact preparation

Contacts are the important part of any detector device. Also they are needed to make electrical measurements of the properties of material or metal-semiconductor junction. The contact quality influences the precision of measurements.

Taking into the consideration differences of the performed experiments in every particular case different contacts were prepared. First part of the research was on high-temperature bulk material properties. Here we tried to prepare stable at high temperature ohmic contacts, so they would not influence measured values. In the second part the properties and preparation techniques of the contacts were investigated. Here different contacts, both ohmic and rectifying, were made.

5.4.1 Welding wires for the high-temperature measurements

High-temperature measurements were done in the atmosphere of cadmium. Thus, thermal stability and chemical passivity to the Cd vapour were required for the

Figure 5.3: Zygo NewWiew 5000 noncontact 3D surface profiler.

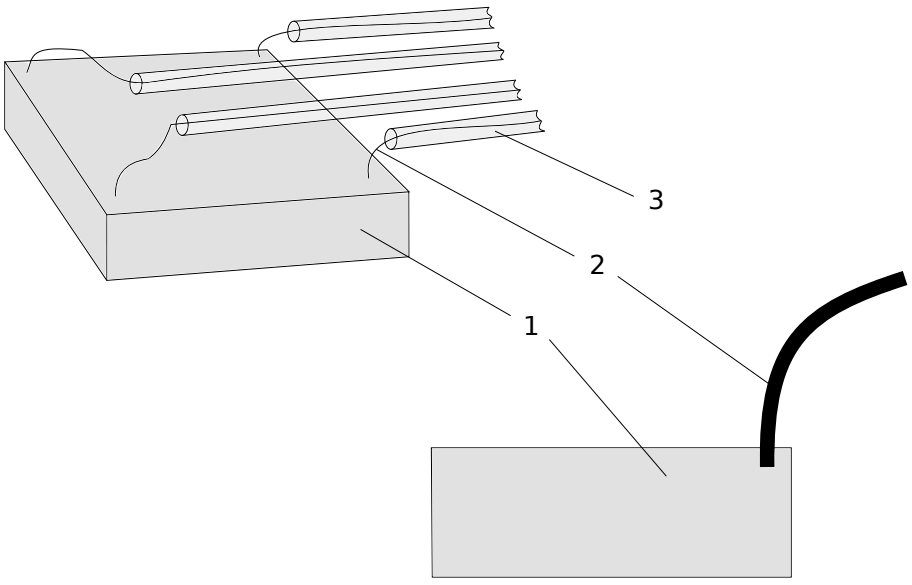

Figure 5.4: Molybdenum wires welded into the sample. 1 - sample; 2 - Mo wire; 3 - quartz capillary tube.

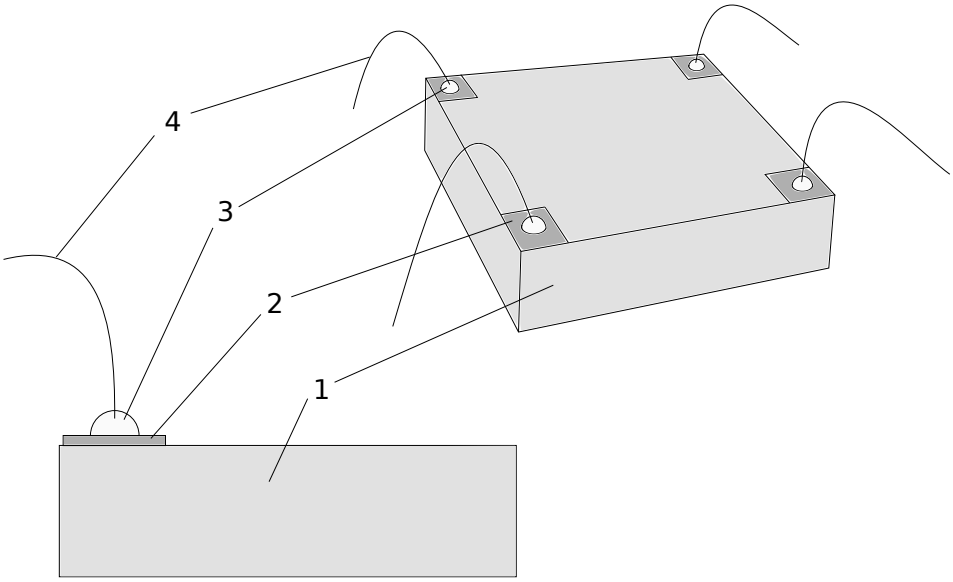

Figure 5.5: Contacts prepared by the chemical deposition or by the thermal evaporation. 1 - sample; 2 - deposited metal; 3 - silver paste or soldered indium; 4 - silver wire.

contacts. Molybdenum wires satisfy both requirements and therefore were used in our study.

Mechanically pressed contacts are commonly used for the high-temperature measurements [111]. However, the local sublimation of CdTe under the wire, especially in case of low component overpressure, results in a lost of the electrical connection. Therefore, welding of the wire into the sample was used.

Surface of the wires was cleaned prior to contact fabrication. For the cleaning the boiling 15 % water solution of NaOCl was used. After $5\,min$ cleaning the wires were washed in water and then in methanol. The welding was done in an argon atmosphere to prevent sample and contact oxidation. Each wire was bent after the welding and put into the quartz capillary tube. No sample holder was needed since Mo wire were hard enough to hold the sample inside the ampoule (Figure 5.4).

5.4.2 Chemical deposition of metals

Gold and platinum were chemically deposited to fabricate metal-semiconductor junctions. Sample surfaces were masked with photoresist. Windows were left in places where metallic contacts were desired to be formed. Samples were heated in oven to 80°C for a period of 20 minutes for photoresist to harden.

Gold was deposited from the 5% water solution of chloroauric acid ($HAuCl_4$).

Chemical reaction can be written as follows:

$$[AuCl_4]^- + 3e^- \rightarrow Au + 4Cl^- \tag{5.1}$$

Process was done at room temperature. Deposition time was 1 minute. Deposition of platinum was similar. It was performed from 0.5% water solution of hexachloroplatinic acid (H_2PtCl_6). Solution was heated to 95°C. Deposition time was 2 minutes. Chemical reaction is:

$$[PtCl_6]^{2-} + 4e^- \rightarrow Pt + 6Cl^- \tag{5.2}$$

As a result, thin layer of metal was formed on the top of CdTe. Remaining photoresist was removed in the acetone. Samples were washed in distilled water, after that in ethanol and in acetone. Finally it was dried in the flow of the warm air.

5.4.3 Thermal evaporation of metals

Thermal evaporation was used to deposit gold and indium contacts. Samples were masked with photoresist in the same way as for the chemical deposition. Chamber was evacuated to the vacuum better than $10^{-3}\,Pa$. A thin layer of metal was deposited on the sample. After the deposition samples were washed and dried by the same scheme as in the chemical deposition.

Silver wires were connected to the metallic contacts. Diameter of the wires was $0.05\,mm$. Contacting was done either by the silver paste or by the indium (Figure 5.5). It was found that soldering with In may change electrical properties of the contacts. That is why silver paste was chosen to be main contacting substance and indium was used for the comparison. When using silver, samples were left for $30\,min$ to harden the paste. No sample heating was used to prevent silver diffusion into the volume.

5.5 Electrical measurements

Series of various electrical measurements were carried out to investigate both material properties and contact preparation techniques.

Chemical self-diffusion in semi-insulating CdTe was studied indirectly through the conductivity. Hall effect measurements were performed to define material main properties. Contacts were characterized by the V-I curves obtained from the current-voltage characteristic. Samples homogeneity was evaluated by the resistivity mapping.

5.5.1 Hall effect

Hall effect measurements were used, since they give a complex information about semiconductor material properties including conductivity type, concentration of the carriers and their mobility. The measured value was Hall voltage, which is given by

$$U_y = \frac{R_H I_x B_z}{b} = R_H j_x B_z, \tag{5.3}$$

where b is a sample thickness in the direction of the magnetic field, R_H is the Hall coefficient and j_x is the current density. The sign of the Hall coefficient allowed us to define the conductivity type of the material. Its value is negative for n-type and positive for p-type:

$$R_H = -\frac{r_H}{nq}, \tag{5.4}$$

with r_H, Hall factor, close to 1. Thus, the carrier concentration is determined as

$$n = -\frac{1}{R_H q}. \tag{5.5}$$

The Hall mobility is defined by the product of the zero-field conductivity, σ_0 and the Hall coefficient:

$$\mu_H = |R_H \sigma_0|. \tag{5.6}$$

Van der Pauw method was used for the measurements. The circuit was the same, as used for the study of the conductivity.

High-temperature Hall effect and conductivity measurements were performed in a two-zone vertical furnace, which was fixed inside the magnet. Zone one, with the sample, was located in the centre of the magnet coils. Zone two, with component, was used to control component overpressure. Experimental set-up is shown in Figure 5.6. Temperature was controlled by the Eurotherm 2408 PID controllers. For the measurement direct current and direct $0.5\,T$ magnetic field were used. The wires from the sample were connected to the switch system as shown in Figure 5.7.

5.5.2 Conductivity

Van der Pauw method was used for study of the conductivity. This method can be used to measure specific resistivity and Hall effect on flat samples with an arbitrary shape. This method allowed us to perform electrical measurements knowing only one geometric parameter - sample thickness. Specific resistivity was calculated from

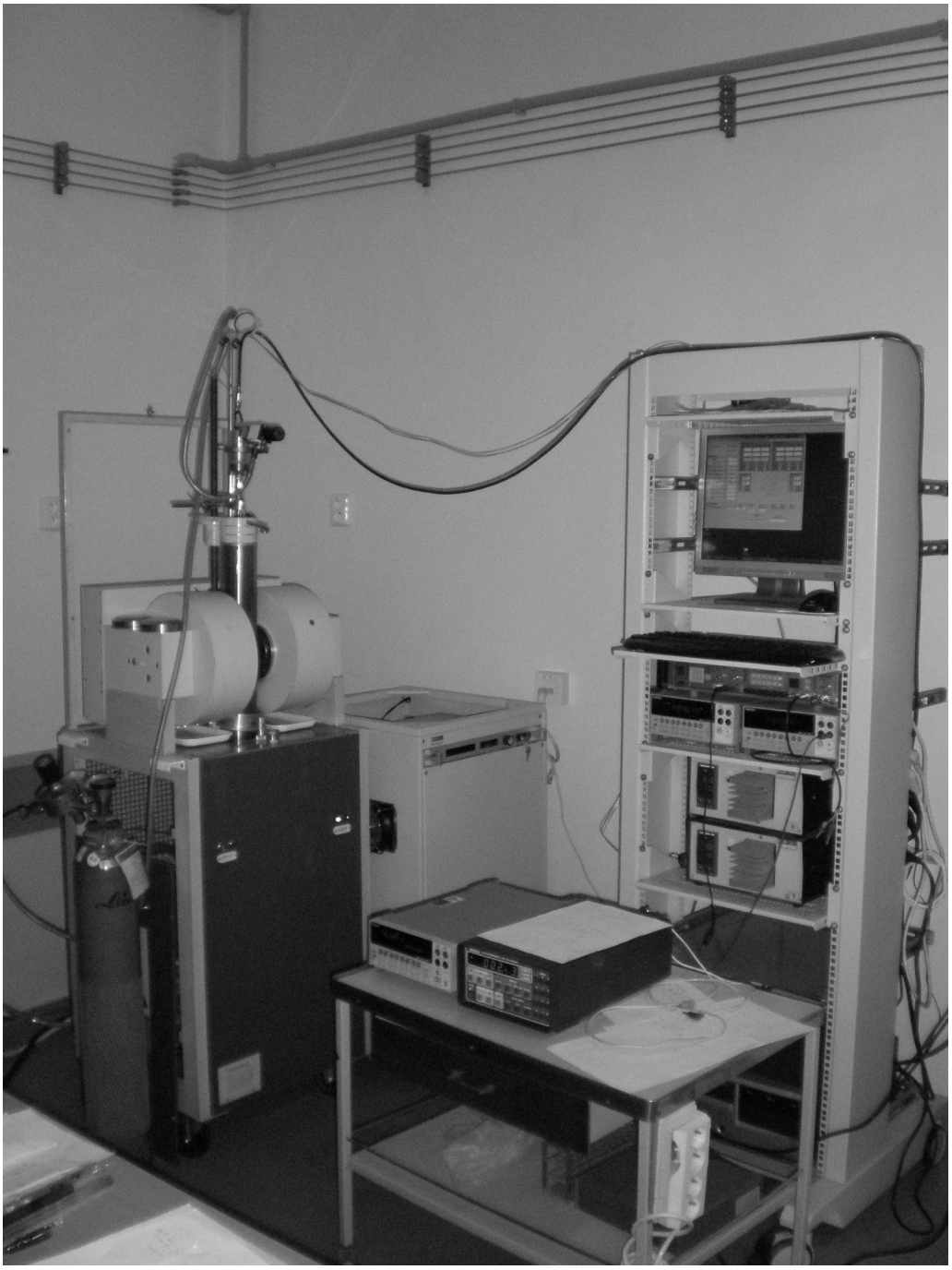

Figure 5.6: High-temperature measurement set-up.

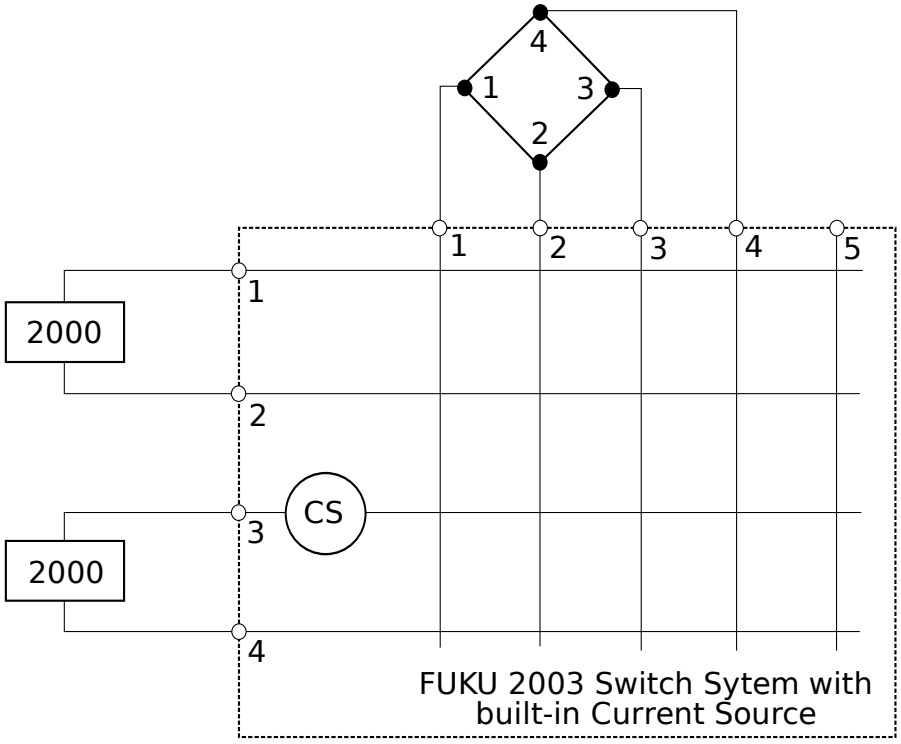

Figure 5.7: Electric circuit used for high-temperature measurements of Hall effect and conductivity. 2000 - Keithley Multimeter; CS - built-in Current Source.

the following equation [112, 113]:

$$\rho = \frac{\pi b}{\ln 2} \frac{R_{12,34} + R_{23,41}}{2} f\left(\frac{R_{12,34}}{R_{23,41}}\right), \tag{5.7}$$

where $R_{12,34} = \frac{V_{34}}{I_{12}}$, $R_{23,41} = \frac{V_{41}}{I_{23}}$ and f being geometric factor that can be given by:

$$f\left(\frac{R_{12,34}}{R_{23,41}}\right) = 1 - \frac{\ln 2}{2}\left(\frac{R_{12,34} - R_{23,41}}{R_{12,34} + R_{23,41}}\right)^2. \tag{5.8}$$

Measurement circuit is shown in Figure 5.7.

5.5.3 Diffusion (through the conductivity)

The sample was placed together with the cadmium source into the quartz ampoule and sealed. Measurements were performed in two zone furnace, one zone controlled the sample temperature and the other the Cd partial pressure.

In a typical measurement cycle the sample was held at a fixed temperature and at an initial P_{Cd_0} until its conductivity (σ_0) was stabilised. After that the cadmium source temperature was step-like changed to obtain sharp change in P_{Cd} and $\tilde{D}$ has been established by a single-exponential fit of normalised conductivity relaxation

[40, 114]

$$\frac{\sigma_t - \sigma_\infty}{\sigma_0 - \sigma_\infty} = A\, e^{-\frac{\tilde{D} t \pi^2}{b^2}}, \tag{5.9}$$

where $b = 1.6\,mm$ is the sample thickness, σ_∞ is the final conductivity, and A is a normalisation parameter. In case of $\tilde{D}(\Delta)$ being dependent on stoichiometry deviation, Δ, the fit with equation (5.9) should be applied to the progressed relaxation, when $\Delta(z)$ deviates only weakly from the final Δ.

Measurements at P_{Cd} near Cd saturation have been performed with aim to minimise the sample sublimation and to prolong the stability of the contacts. Three samples have been measured. Two of them to inspect basic relaxation characteristics and the third sample for detailed measurement of the diffusion. Data of the third sample were used for the evaluation of $\tilde{D}$.

5.5.4 Current-voltage characteristics

A current-voltage characteristic is a relationship between the DC current through an electronic device and the DC voltage across its terminals. Also known as I-V curves, it is used in electronics to determine basic parameters of a device and to model its behaviour in an electrical circuit.

To measure V-I on semi-insulating CdTe special set-up was built. Experimental circuit is shown in Figure 5.8. A single Model 7152 Matrix Card, housed in a Model 7001 mainframe, was used to connect the electrometer and the current source to the sample. Model 6514 Electrometer was chosen because of its $> 200\,T\Omega$ input impedance. To ensure faster measurement time, guarded measurements were made by turning the Guard switch ON for the Model 6514, and by guarding the Model 220 output using a Model 6167 guarded input adapter. All cabling was made using low noise triax input cables.

Samples were measured inside the cryostat to exclude illumination influence on the sample electrical properties. Whole set-up is pictured in Figure 5.9.

Two- and three-point methods were used, respectively. In the first one the voltage is measured on the same terminals through which the current flows. It is widely used for characterization of detector devices. However, it gives an information on the whole structure. Three-point method employs third independent terminal, through which the current does not flow. In this case it is possible to obtain I-V curve for a single terminal. In our measurements we define current flowing from the contact to the sample as being positive.

For the measurement control and data acquisition a special program was written.

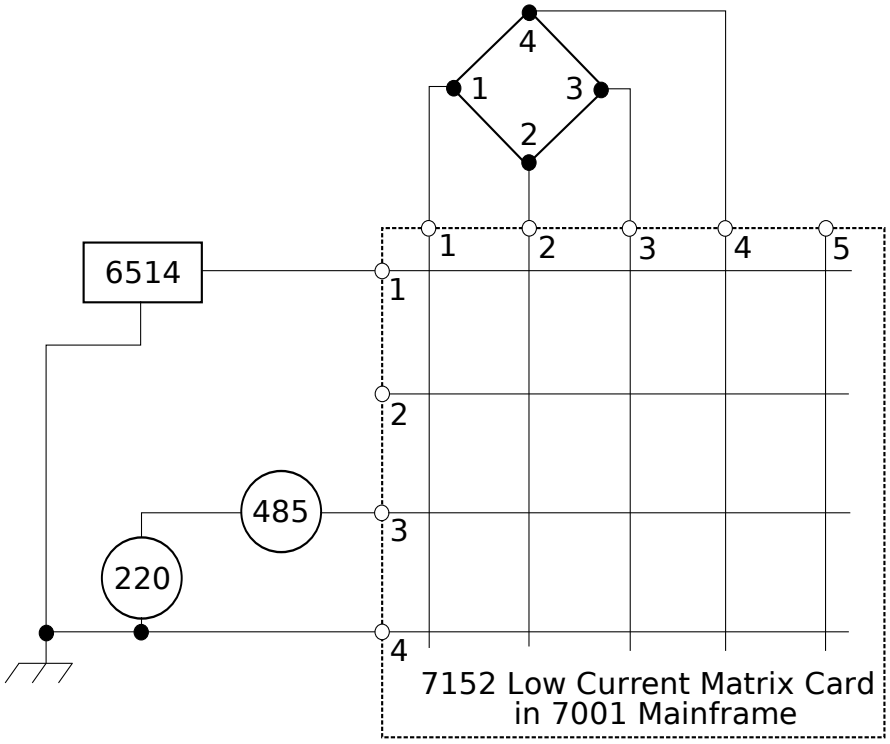

Figure 5.8: Electric circuit used for current-voltage characteristic study of the contacts on semi-insulating CdTe. 6514 - Keithley System Electrometer; 220 - Keithley programmable Current Source; 485 - Keithley Autoranging Picoammeter.

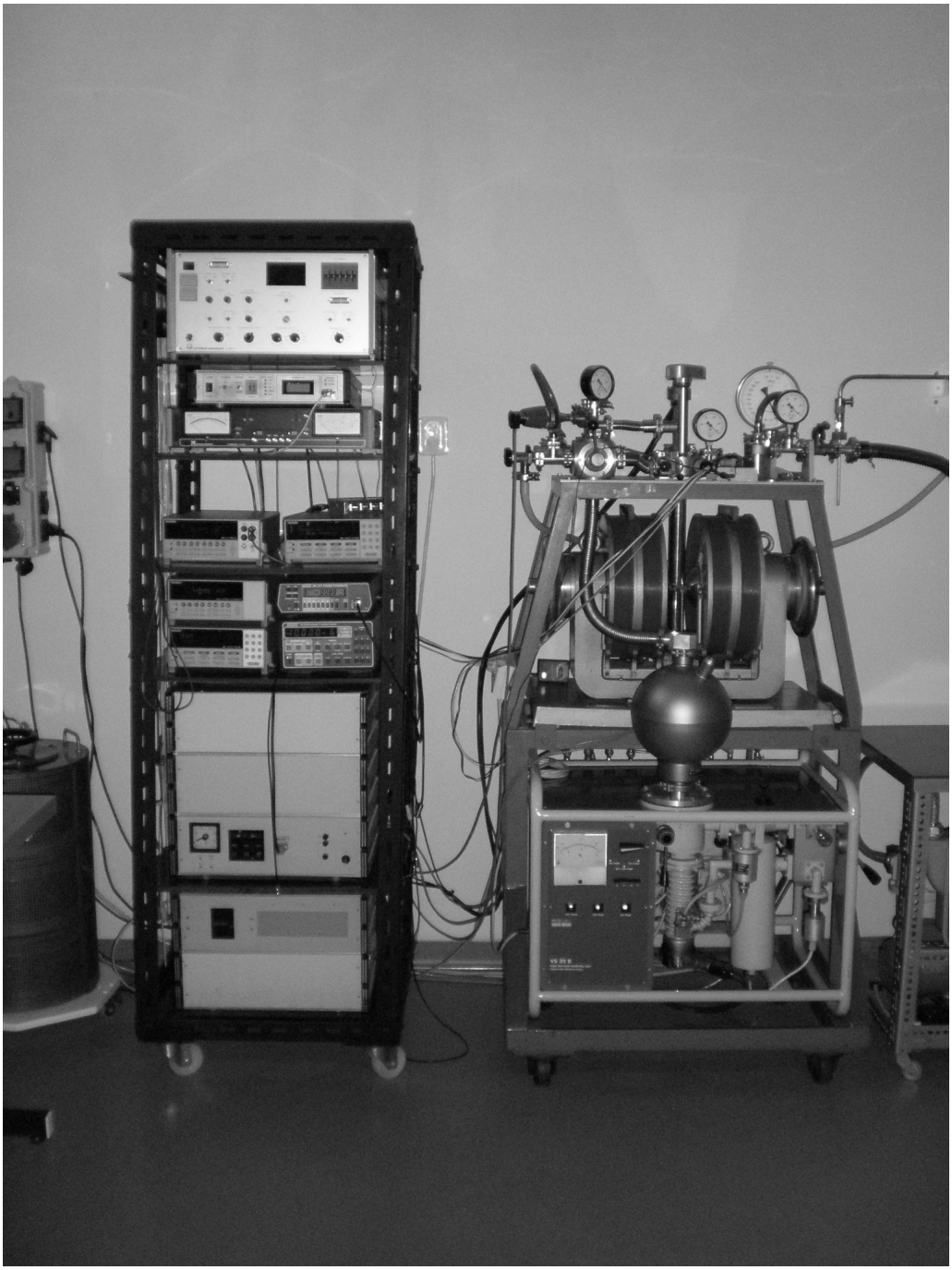

Figure 5.9: Low-temperature measurement set-up used for current-voltage characteristics study.

5.5.5 Capacitance-voltage

The capacitance per unit area of the Schottky diode is given by

$$\frac{C}{A} = \sqrt{\frac{\pm q\varepsilon_r\varepsilon_0(N_A - N_D)}{2(\pm V_{bi} \pm V - \frac{kT}{q})}} \tag{5.10}$$

where the "+" sign applies to a p-type ($N_A > N_D$) and the "-" sign to an n-type ($N_A < N_D$) material, ε_r is semiconductor dielectric constant, and V is the reverse-bias voltage [115]. For n-type material $N_A < N_D$, $V_{bi} < 0$, and $V < 0$, whereas for p-type material $N_A > N_D$, $V_{bi} > 0$, and $V > 0$. The $\frac{kT}{q}$ in the denominator accounts for the majority carrier tail in the space-charge region which is omitted in the depletion approximation. The built-in potential is related to the barrier height by the relationship

$$\phi_B = V_{bi} + V_0 \tag{5.11}$$

$$V_0 = (\frac{kT}{q}) \ln \frac{N_c}{N_D}, \tag{5.12}$$

where N_c is the effective density of states in the conduction band. Plotting $1/(\frac{C}{A})^2$ versus V gives a curve with slope $2/[q\varepsilon_r\varepsilon_0(N_A - N_D)]$, and with the intercept on the V-axis, $V_i = -V_{bi} + \frac{kT}{q}$.

The barrier height is determined from the intercept voltage by

$$\phi_B = -V_i + V_0 + \frac{kT}{q} \tag{5.13}$$

With aim to collect maximum information about measured samples, we have utilized kind offer to exploit the equipment of the CNRL (VUT, Brno) and performed capacitance-voltage measurements there. Agilent E4980A Precision LCR Meter was chosen for its wide frequency range, powerful compensation functions, and highly accurate bias characteristics. This versatility of the meter guaranteed highly accurate C-V measurements, and higher efficiency in the evaluation of MOS properties.

5.5.6 Resistivity mapping

Time Dependent Charge Measurements (TDCM) was utilized for the resistivity mapping [116]. This contactless non destructive method allowed to study areal homogeneity of the resistivity without degrading of the surface quality. In this method the sample acts as a capacitor and the resistivity is evaluated by measuring a time dependent charge transient observed after application of a voltage step.

The CdTe wafer was inserted between a 2.5 mm in diameter measurement electrode, surrounded by an extended guard electrode, and a back electrode (Figure

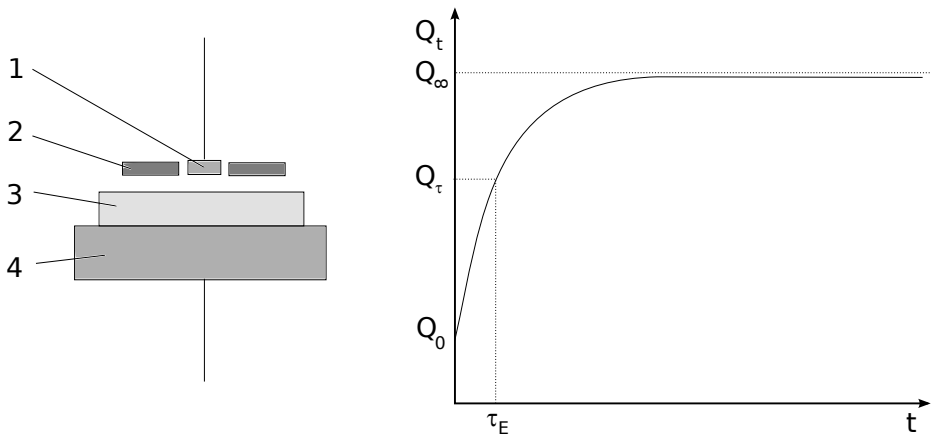

Figure 5.10: Measurement cell structure and the measured Q/t curve for the TDCM. 1 - top (scanning) electrode; 2 - guard; 3 - sample; 4 - bottom electrode

5.10). Planar semiconductor sample is equivalent to a parallel capacitor C_s and a resistor R_s. C_a is the total series capacitance of the contact resulting from the space between the sample and the electrode. The measurement routine is initiated with a voltage step instantaneously charging the capacitors connected in series. C_s is discharged with a characteristic time constant τ_E such that eventually the equivalent circuit is reduced to C_a. The charge redistribution is recorded as shown in Figure (5.10). Using the measured charges Q_0 (after application of the step voltage), Q_∞ (after completed charge transfer to C_a) and τ_E the substrate resistivity can be evaluated according to

$$\rho = Q_0 \tau_E [Q_\infty \varepsilon_r \varepsilon_0]^{-1}, \tag{5.14}$$

where ε_r is the relative permittivity constant of the material (10.3 for CdTe), and ε_0 is the permittivity of vacuum. Detailed resistivity maps of the samples were obtained.

Chapter 6

Results & Discussions

6.1 Sample characterization

All studied samples were cut from single crystals. However, it was taken into the consideration that even inside one grain a gradient of material properties can be observed. Such heterogeneity may be crucial for measurement precision and can significantly decrease that. Thus, special measures were taken to eliminate possible errors. Both volume and surface of the samples were controlled. Prior to electrical measurements samples were mapped to define degree of their homogeneity. Also surface topology was measured after treatment in various etching solutions.

6.1.1 Resistivity mapping

Resistivity mapping was done using commercially available equipment (COREMA, SemiMap Scientific Instruments, Germany). The capacitive metal electrodes above and below the sample were positioned by fast and precise xy translation. They defined local sample and air capacitors at the desired measurement spot. A charging voltage step was applied to the R-C circuit and the dynamic charge redistribution was recorded. The resistivity was obtained from the initial and final charge values and the relaxation time. A typical result obtained from measurement is shown in Figure 6.1.

Distribution of the resistivity in all samples was similar. The electrical resistivity of semi-insulating samples ranged from $\sim 3 \times 10^9$ to $4.5 \times 10^9\,\Omega cm$. Excluding edges, waste area resistivity lies in the range from 3.3×10^9 to $3.5 \times 10^9\,\Omega cm$. Sample do not have any grain boundaries. Resistivity is homogeneously distributed trough the whole volume of the sample.

6.1.2 Surface topology

Topology was studied on surfaces treated in two different etching solutions (HBr and HI). Samples were etched for 20, 40, and 60 seconds. One additional measure-

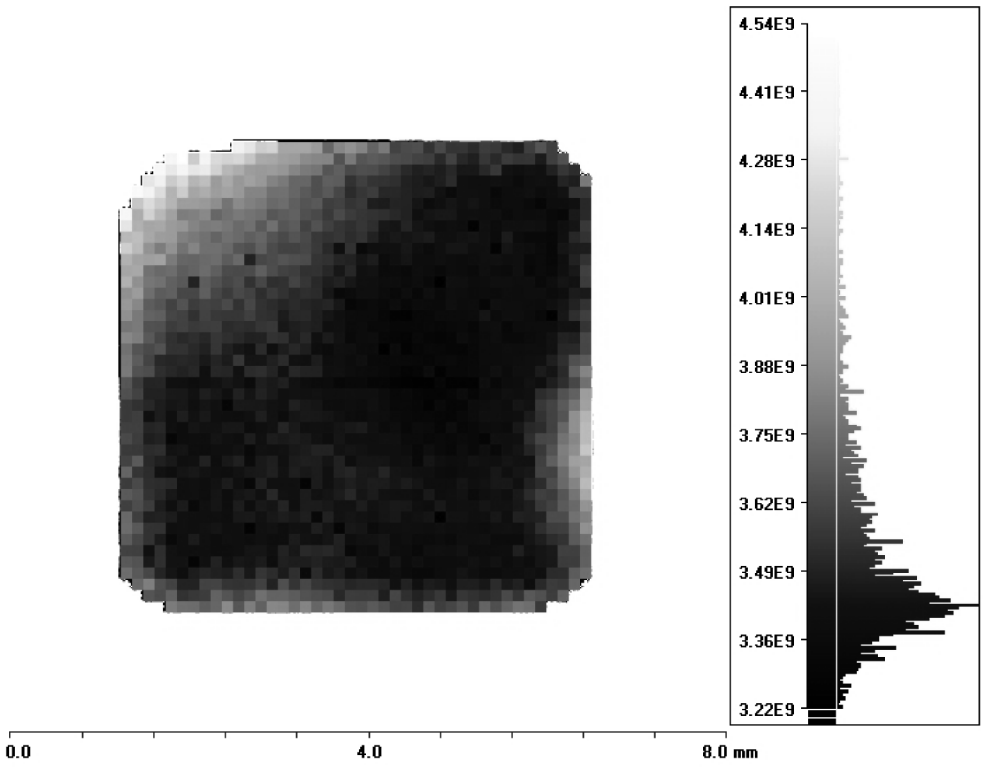

Figure 6.1: A typical image obtained from the sample resistivity mapping. Left part shows the areal resistivity profile, right part plots the resistivity distribution.

Table 6.1: Comparison of surface roughness after treatment in various solutions.

etching	roughness, nm	
time, s	HBr - solution	HI - solution
before etching	9.22	8.06
20	5.20	5.30
40	4.92	1.45
60	3.08	1.53

ment was made before etching to be used as a reference. Results of the root-mean-square roughness measurements are summarized in Table 6.1. Initial surfaces of the samples just after polishing are similar. Roughness better than $10\,nm$ is the best quality which is possible to obtain on the hand-polished surfaces. By the chemical-mechanical polishing smoother surface can be manufactured only by using precise polishing equipment. Further improvement of the samples' properties was made by the chemical etching process. For the HBr-solution the lowest surface roughness (the better quality) is obtained after $60\,s$. It is on the level of $\sim 3\,nm$. In case of HI-solution the best quality is reached after $40\,s$. This time is enough to get even better surface with twice lower roughness at the level under $1.5\,nm$. Etching rate for this particular solution is different (HBr - $4.33\,\mu m/min$; HI - $15\,\mu m/min$). Thus, to remove destructed layer in HBr-solution longer time is needed. Roughness of the sample surface after etching in HI-solution for $60\,s$ has slightly higher value. Since the difference is within the statistical deviation it is considered irrelevant. These results show that the etching process consists of at least 2 stages. On the first stage surface inhomogeneities are removed faster. This can be explained by the nature of the etching solution. None of the etchant is absolutely non-selective. At the beginning of the etching process peaks are removed faster which results in obtaining smoother surfaces. On the second stage after removing damaged layer and reaching the best surface quality etching speed normalises for the whole surface area. However, in case of large stock removal, the surface roughness starts to increase since etching process is very complex and is never homogeneous.

Three dimensional (3D) surface maps for the modular scanning areas of $0.18\,mm \times 0.13\,mm$ are presented in the Figures 6.2 and 6.3. They represent surfaces of the CdTe samples treated at room temperature in HBr - solution for $60\,s$ and in HI - solution for $40\,s$ respectively. Thin peaks on both figures correspond to settled powdery dust. The deviations from the ideal flat surface in the form of waves is caused by the crystal structure of the samples. Semiconductor crystals contain different kinds of defects as described in Section 1.4. Etching rate for these defects differs from the perfect crystal lattice. As a result in places where defects came into the the surface sample is etched with another velocity. Etching process by itself is inhomogeneous due to many factors. Altogether, it influences the shape of the obtained surface.

Diagonal surface profiles from the 3D surface maps are pictured on Figures 6.4 and 6.5. Small oscillations are characteristic for the solutions representing chemical interaction between solution and sample components. Difference in height of the waves is caused by the nature of the etching solution as well. It is apparent, that etching in HI - solution under the same conditions gives approximately twice lower surface roughness in comparison with using HBr - solution.

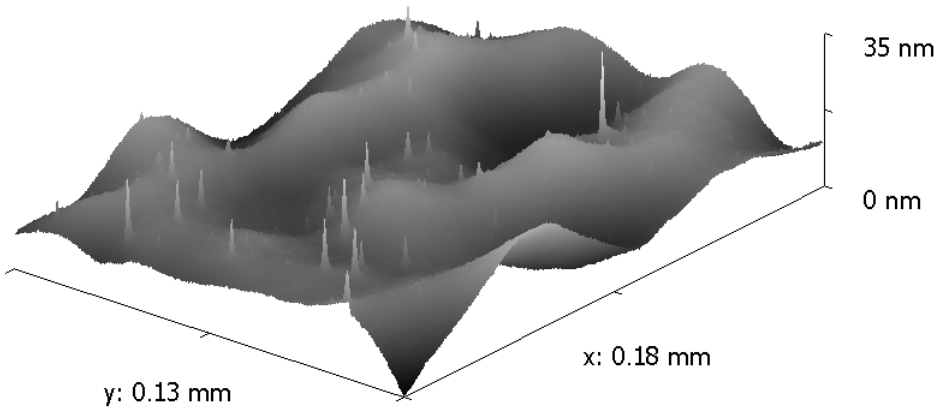

Figure 6.2: Oblique plot of the sample surface after etching in HBr - solution at room temperature for 60 seconds.

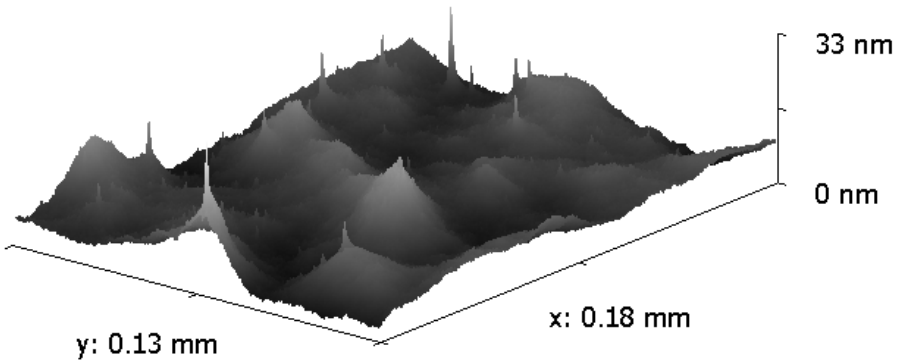

Figure 6.3: Oblique plot of the sample surface after etching in HI - solution at room temperature for 40 seconds.

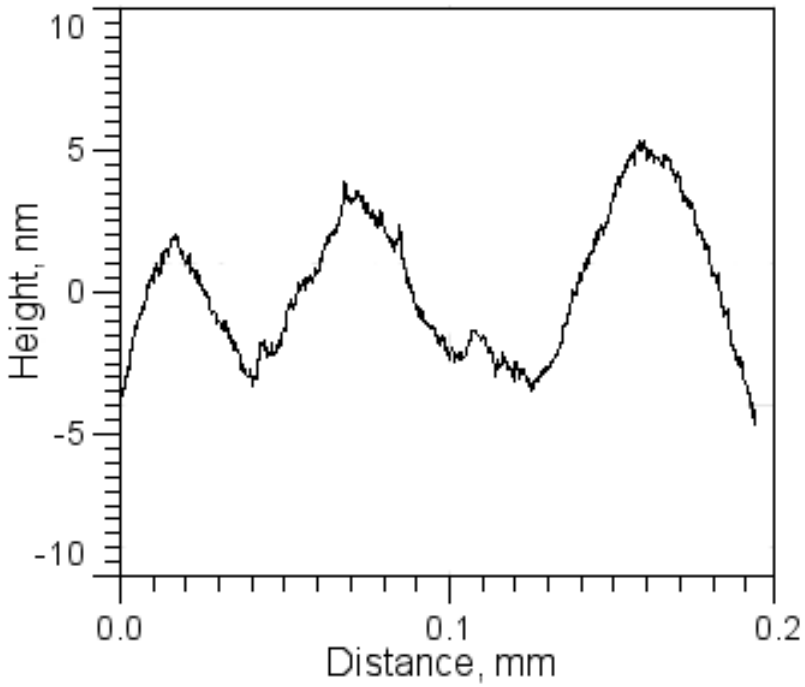

Figure 6.4: Surface profile of the CdTe surface etched in HBr - solution at room temperature for 60 seconds.

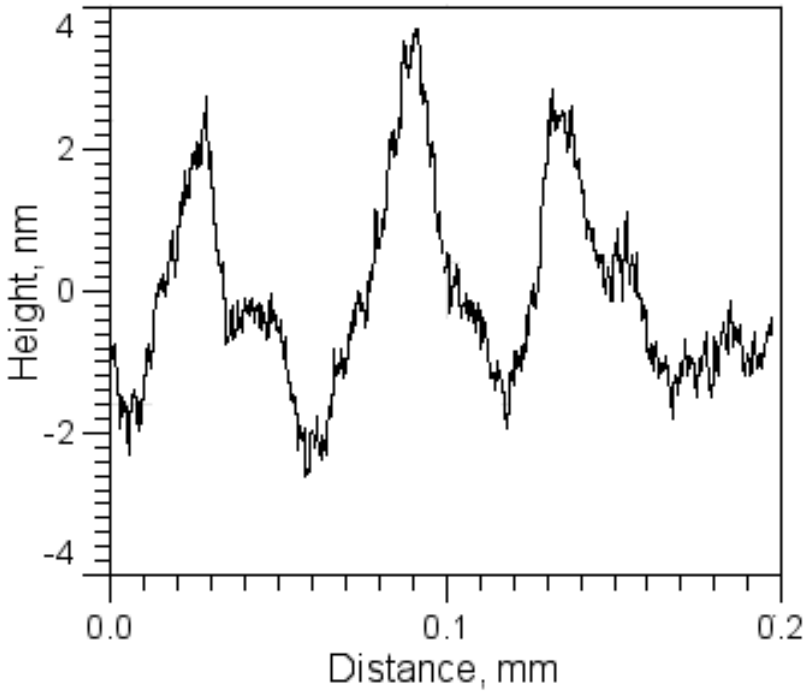

Figure 6.5: Surface profile of the sample surface treated in HI - solution at room temperature for 40 seconds.

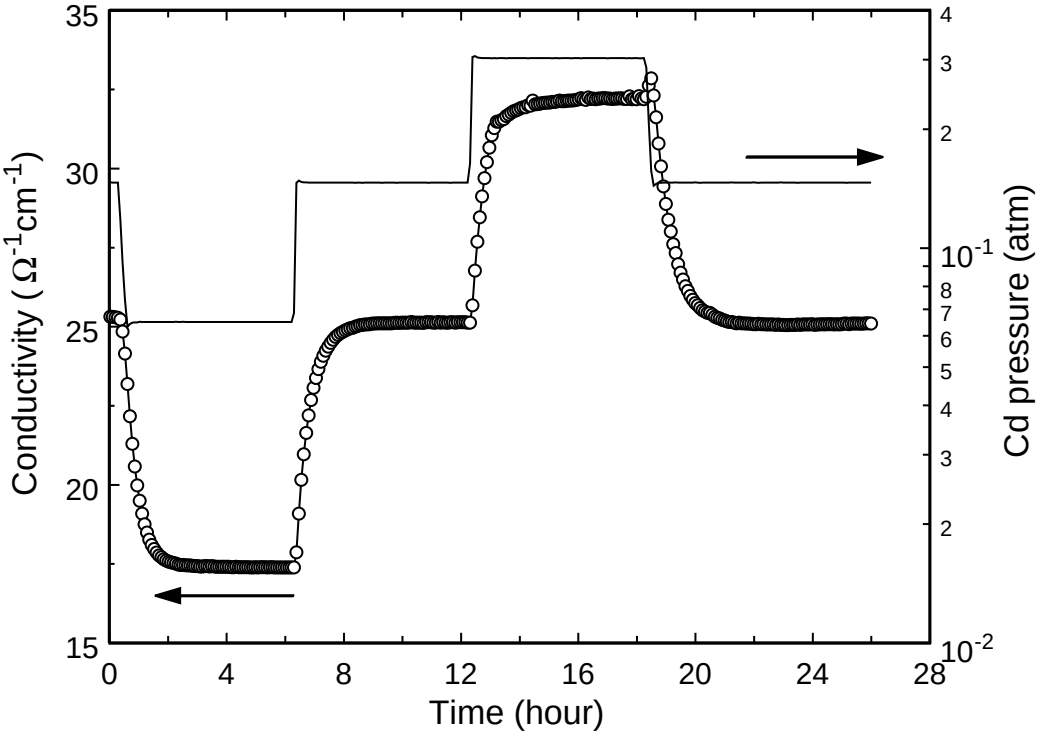

Figure 6.6: Four steps of conductivity relaxation of CdTe:Cl at $700^\circ C$. Small increase of σ after P_{Cd} step down at 18.2 hour is due to instability of the furnace at the fast cooling of Cd source. This drawback does not affect the evaluation of $\tilde{D}$, which is determined at latter period of σ_t.

6.2 Chemical diffusion in bulk CdTe:Cl

The conductivity relaxation and chemical diffusion have been measured in relatively narrow temperature interval 600-700°C. The reason is in a large activation energy of diffusion found in this material. Above 700°C the relaxation is too fast to stabilise P_{Cd} satisfactorily before the dominant part of relaxation occurs. Below 600°C the delay to reach the final state has extended up to several days and the sample became unstable during the long delay, when several relaxation cycles had to be measured. Typical profile of σ_t at 700°C is plotted in Figure 6.6.

Prior the analysis of $\tilde{D}$ the defect equilibrium has been studied. The theory outlined in section 1.4 has been used to describe measured conductivity and results are shown in Figure 6.7. An excellent fit has been obtained taking total Cl density [Cl]$=4 \times 10^{18}\, cm^{-3}$ and A-centre formation energy $E_A = -0.38\, eV$, when other parameters remained unchanged as established in undoped CdTe. The evaluated [Cl] is close to the intentional doping of the melt, which is probably caused by a fast solidification and minimised segregation of Cl into melt. Analogous Cl doping of the melt used in [117] resulted in significantly lower [Cl] found in the solid CdTe:Cl.

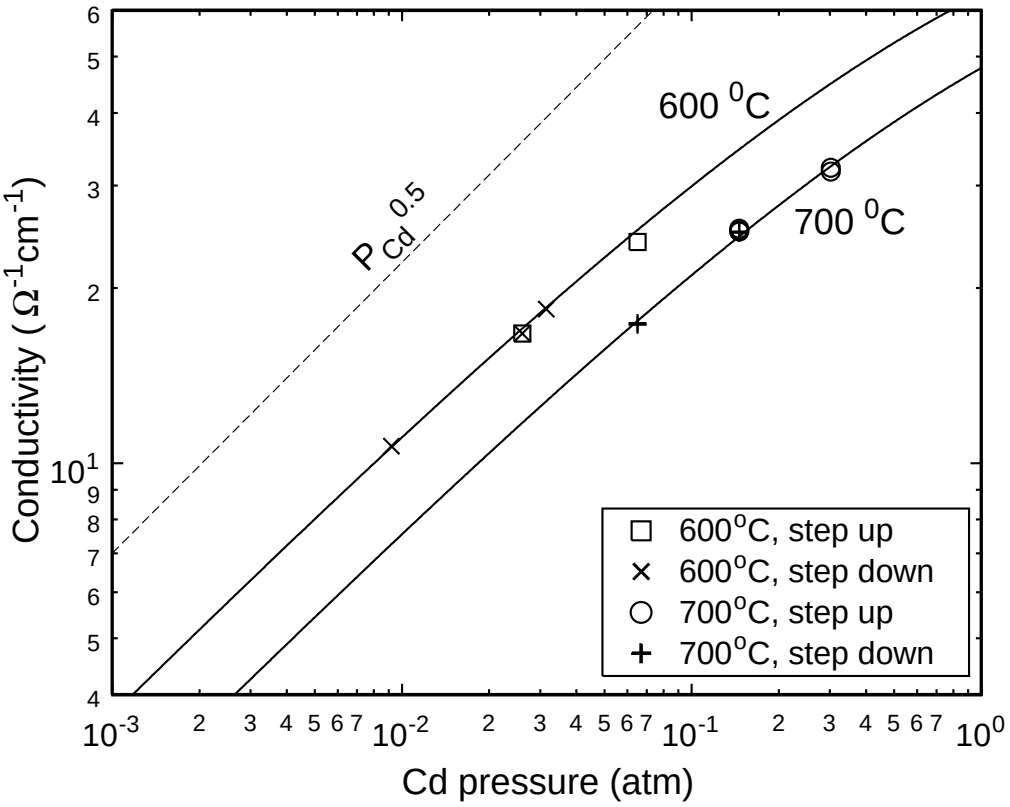

Figure 6.7: Experimental and theoretical equilibrium conductivity of CdTe:Cl. Remarks 'step up/step down' outline the direction of change of P_{Cd} 'increased/decreased' to reach the final value. Dash line indicates the slope of $P_{Cd}^{0.5}$ characteristic for compensated semiconductor.

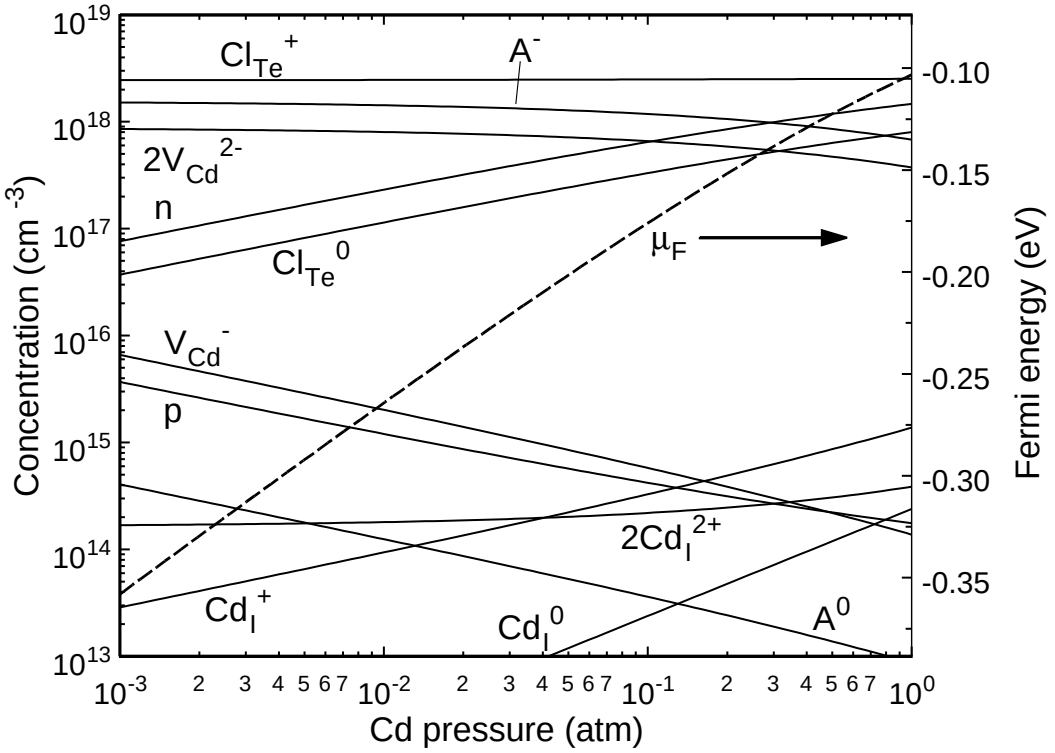

Figure 6.8: Calculated free carrier and point defect densities of Cl-doped CdTe [Cl]=$4 \times 10^{18}\, cm^{-3}$ at 700°C. Fermi energy is depicted by the right axis.

The fitted E_A is similar to $E_A = -0.5\, eV$ estimated within Coulomb model [5].

$\sigma \propto P_{Cd}^{0.5}$ points to compensated semiconductor, which slightly converts to uncompensated material at maximum P_{Cd}. The proximity of σ relaxed after P_{Cd} up/down step proves that there is no effect of the step direction and σ has relaxed into final state. The detailed view on the defect structure at 700°C is given in Figure 6.8. It is apparent that in compensated CdTe:Cl the densities of principal point defects change only weakly and Cl_{Te}^{+} are compensated by A^{-} and V_{Cd}^{2-} acceptors.

The chemical diffusion coefficient has been established according equation (5.9). Several examples of the single-exponential fit of σ_t are plotted in Figure 6.9. It was found that most curves can be easily fit with single exponential, if the initial period of relaxation is skipped. An exception has been identified at 700°C near Cd saturation ($P_{Cd} = 0.3\, atm$), where 90% of the relaxation occurred approximately twice faster than the final part used for the evaluation of $\tilde{D}$. Such behaviour cannot be explained within model used here. Taking into account that the effect is apparent only near Cd saturation, we could speculate that partial melting of disturbed regions of the sample, especially along dislocations, might enhance the diffusion there. Similar course of σ_t was reported without relevant comment also in [40].

The comprehensive summary of experimental and calculated chemical diffusion

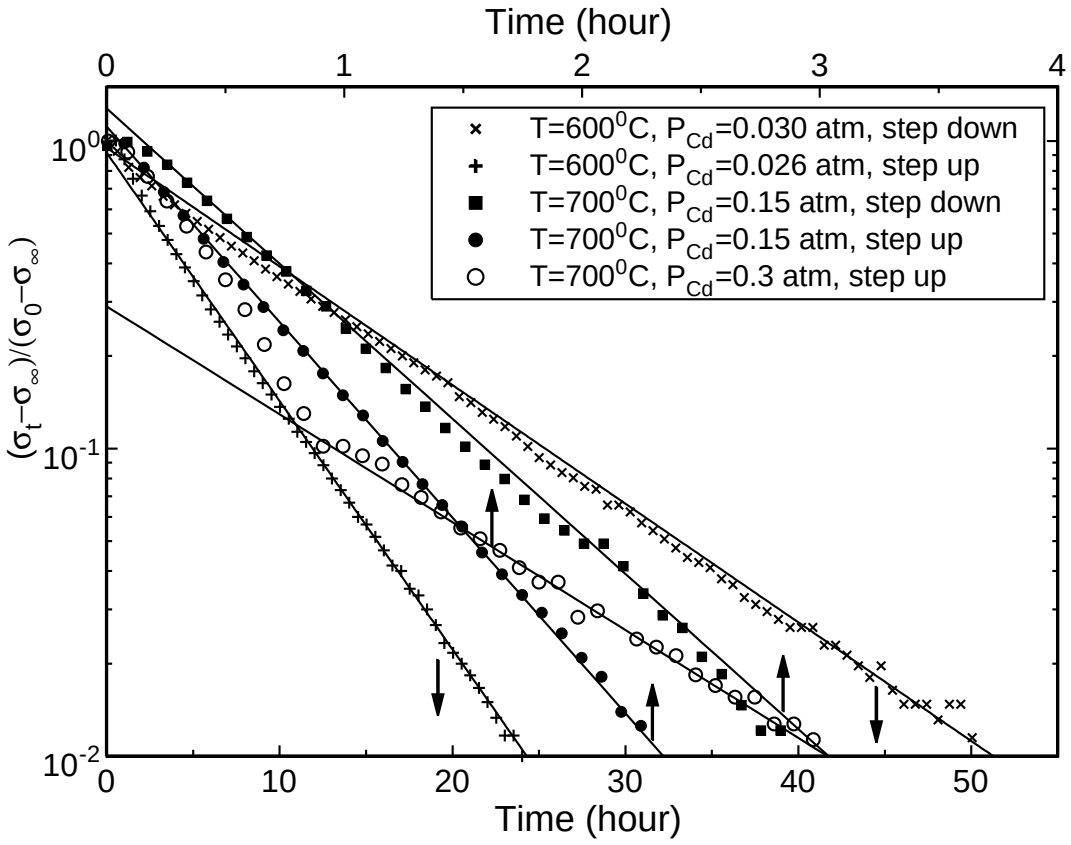

Figure 6.9: Single-exponential fit of the conductivity relaxation at conditions given in the legend. The time of relaxation at 600°C/700°C is depicted by the bottom/upper time axis.

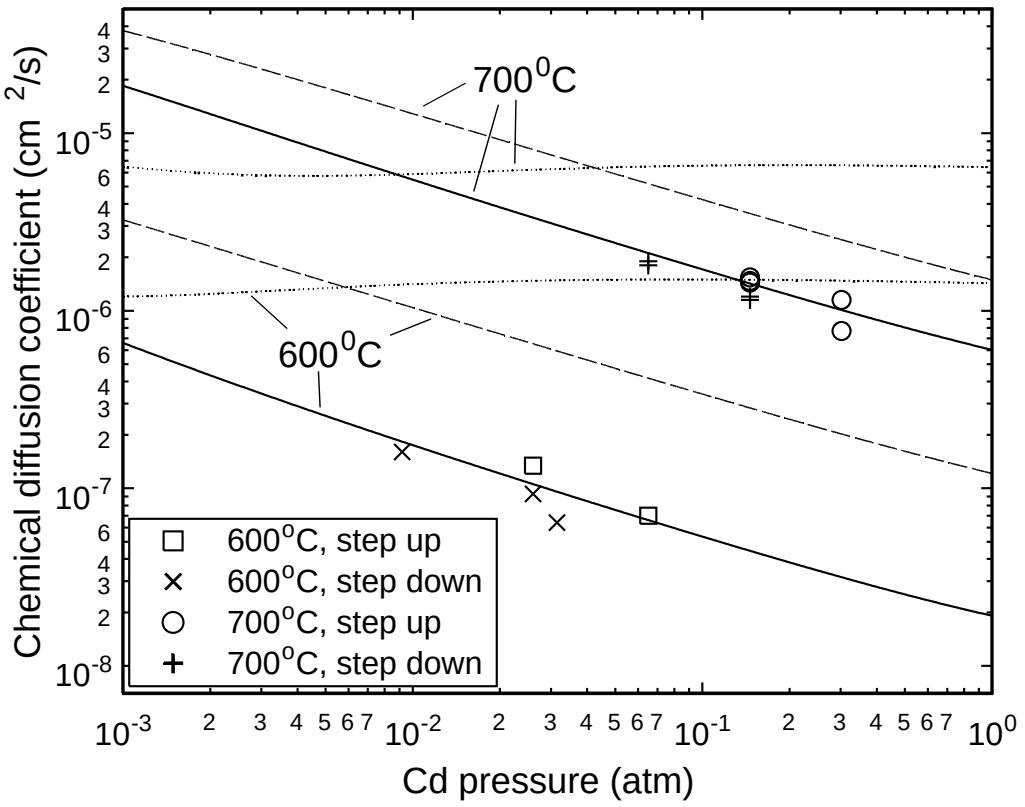

Figure 6.10: Experimental and theoretical chemical diffusion coefficients at temperatures 600°C (bottom lines) and 700°C (upper lines). Dash lines show $\tilde{D}$ for $D(V_{Cd}^{2-}) = \tilde{D}_u/3$. Full lines depict $\tilde{D}$ for $D(V_{Cd}^{2-})$ and $D(V_{Cd}^{-})$ given by eqs. (6.1), (6.2). Dotted lines depict undoped CdTe.

coefficients is presented in Figure 6.10. Let us pay the attention to experimental data at first. Though the interval of P_{Cd} is relatively narrow, it is apparent that $\tilde{D} \propto P_{Cd}^{-0.5}$ as was predicted in equation (2.22). The relaxation after step up/down yields distinct $\tilde{D}$. This 'memory effect' cannot be explained in standard diffusion theory. We expect that the effect enhances with poorer quality of the material, its homogeneity, purity or crystallinity. Comparing with other reports [118] the relaxation time ratio $\tau^+/\tau^- \approx 0.8$ observed here is insignificant.

Having defect properties determined by the fit of equilibrium transport data, the calculation of $\tilde{D}$ according equation (2.21) is limited by unsettled diffusion coefficients of involved diffusing point defects. The first trial to express $\tilde{D}$ was done according [51] taking diffusion coefficients of all diffusing native defects equal to $\tilde{D}_u/3$. The point of this approach stems from the fact that measured $\tilde{D}_u$ in undoped CdTe is independent of P_{Cd} and this choice allows to accomplish satisfactorily such a result. Respective $\tilde{D}$ are outlined in Figure 6.10 by dash lines. We see that $\tilde{D}$ exhibits the proper slope $\tilde{D} \propto P_{Cd}^{-0.5}$. The magnitude, however, deviates from experimental points. Due to V_{Cd}^{2-} is the only principal native defect driving diffusion in CdTe:Cl, see equation (2.22), the unique parameter to be tuned $D(V_{Cd}^{2-})$ remains. In parallel, the demand of P_{Cd} independent $\tilde{D}_u$ can be fulfilled with complementary optimisation of $D(V_{Cd}^{-})$. The final fits of $\tilde{D}$ and $\tilde{D}_u$ are plotted in Figure 6.10 by full and dotted lines, respectively, that have been obtained with

$$D(\mathrm{V}_{\mathrm{Cd}}^{2-}) = 2.8 \times 10^3 \, e^{-\frac{1.82\,\mathrm{eV}}{k_B T}} \ \ \mathrm{cm}^2/\mathrm{s}, \tag{6.1}$$

$$D(\mathrm{V}_{\mathrm{Cd}}^{-}) = 4 \times 10^{-4} \, e^{-\frac{0.2\,\mathrm{eV}}{k_B T}} \ \ \mathrm{cm}^2/\mathrm{s}. \tag{6.2}$$

Regardless completion of all demands put on the fit and excellent agreement with experiment, diffusion coefficients (6.1), (6.2) must be analysed with care. Let us concentrate on $D(V_{Cd}^{2-})$ at first. This parameter expresses a very good agreement with that evaluated from self-diffusion data in CdTe [36]

$$D(\mathrm{V}_{\mathrm{Cd}}^{2-}) = \frac{2.74 \times 10^3}{f_c} \, e^{-\frac{1.85\,\mathrm{eV}}{k_B T}} \ \ \mathrm{cm}^2/\mathrm{s}, \tag{6.3}$$

where the correlation factor $f_c \approx 1$. Taking into account that equation (6.3) was not implicitly used at the calculations, its proximity to equation (6.1) strongly supports defect model used. On the contrary, the fit of $D(V_{Cd}^{-})$ looks rather artificial. There is no principal argument for big difference from $D(V_{Cd}^{2-})$ and an alternative approach should be searched as well. One of the possibilities to make the model more realistic is the involvement of another native defect abandoned here till now. Fast diffusing Te interstitial Te_I could be a good candidate for that. This native defect was skipped out in defect models due to its equivalence with V_{Cd} in defect chemistry reaction

constants, which makes it hardly distinguishable, and larger formation energy [20, 119] making Te_{I} suppressed. Contingent enhanced $D(Te_I)$ would, however, bring Te_I to the central attention.

The numerical results based on relatively troublesome calculations are conveniently represented by the form

$$\tilde{D} = \frac{1.5 \times 10^7}{\sqrt{P_{\mathrm{Cd}}(\mathrm{atm})}}\, e^{-\frac{2.55\,\mathrm{eV}}{k_B T}} \ \ \mathrm{cm}^2/\mathrm{s}, \tag{6.4}$$

which expresses significantly larger activation energy of diffusion $2.55\,eV$ in CdTe:Cl relatively to $1.15\,eV$ (equation 2.6) found in undoped CdTe.

6.3 Properties of the contacts

The subjects of this study were electrical contacts on the semi-insulating cadmium telluride. Dependence of the contact properties on the metal nature, deposition technique, and anterior surface treatment were studied in details. Samples were etched using techniques described in section 5.3.1. Deposition of the contacts was made as described in sections 5.4.2 and 5.4.3. Four types of contacts were prepared:

- deposited from the solution gold - Au_{ch};
- deposited from the solution platinum - Pt_{ch};
- thermally deposited gold - Au_{th};
- thermally deposited indium - In_{th}.

Current-voltage characteristics of the contacts were measured at room temperature in accordance with section 5.5.4. To assure reproducibility of the results, measurement were independently repeated. Each curve represents data obtained out of 8 measurements.

A relative quantity R_{sp} was introduced for the evaluation of the contacts quality. It was defined as

$$R_{sp} = \frac{t^+}{t^-}, \tag{6.5}$$

where $\mathrm{t}^{+/-}$ represents the slope of the direct/reverse current-voltage characteristic near the maximum voltage.

6.3.1 Three-terminal versus two-terminal I-V technique

For this particular measurements samples were etched in standard 3% Br-methanol solution. Gold contacts were deposited from the aqueous solution. Measurements were made at room temperature.

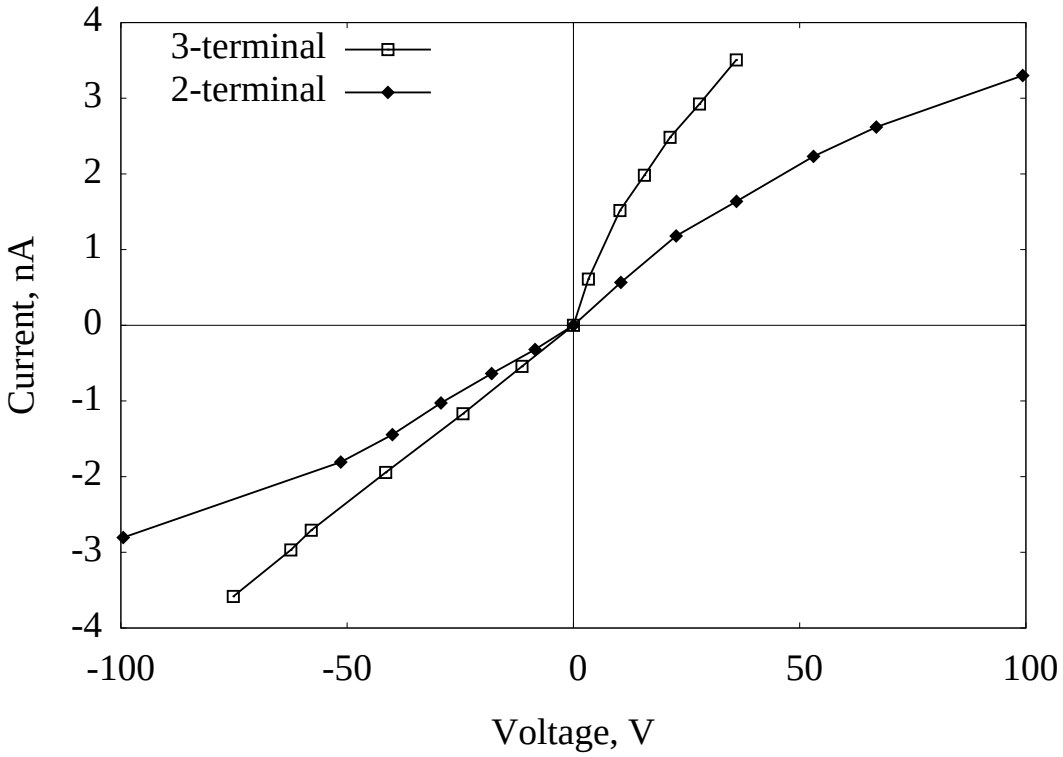

Figure 6.11: Comparison of the current-voltage characteristics of the gold contact on the n-type sample treated in the Br-solution obtained using three- and two-terminal methods.

A comparative two- and three-terminal I-V measurement showed the benefit of the latter method for the investigation of the properties of the single contact. As shown in Figure 6.11 in the two-terminal method the curve is roughly symmetric, but the three-terminal method proves that the contacts are non-ohmic. This is because of the circuit arrangement. All contacts are metal-semiconductor junctions. In case of two-terminal measurements the properties of two junctions connected in the opposite direction are measured jointly leading to the lost of information about each of the terminals. Three-terminal measurement solves this problem by utilizing third independent electrode for the measurement of potential. As a result, it gives precise information on each contact separately.

6.3.2 Comparison of various metals as contact materials

Detailed investigation of the properties of metal contacts deposited on CdTe was done. Both n- and p-type semi-insulating cadmium telluride samples were used. Four various types of contacts were fabricated. Gold, platinum and indium were employed as contact materials. In case of Au two deposition techniques were used, namely thermal evaporation and deposition from aqueous solution. Surfaces of all samples were prepared by the same technique, including chemical-mechanical polishing and treatment in etching solution.

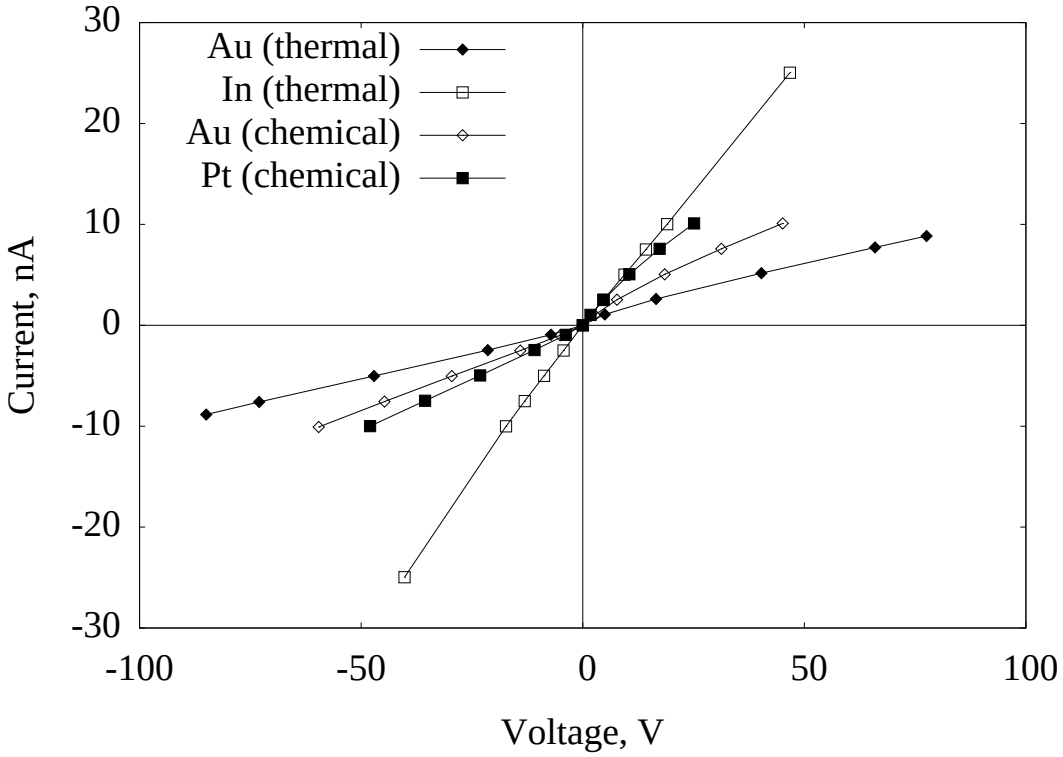

Figure 6.12: Comparison of the current-voltage characteristics of the metal-semiconductor junctions prepared on n-CdTe. Sample surface was treated in standard bromine-methanol solution. Contacts were prepared using various metals and techniques: ♦ - thermally evaporated Au; □ - thermally evaporated In; ◊ - Au deposited from the aqueous solution; ■ - Pt deposited from the aqueous solution.

A comparison of the properties of the contacts made out of various metals on the n-type cadmium telluride etched in 3% Br-methanol solution is shown on Figure 6.12. Current-voltage characteristic of the indium contact is close to linear. Characteristic curves representing Au_{th}, Au_{ch}, and Pt_{ch} contacts are different. In the negative bias all the three behave according to Ohm's law. Linear dependencies of the current on applied voltage have only different slopes. This points on different contact resistance. For the positive bias stronger increase of current is observed.

Concave shaped I-V curves under forward bias are observed on most Au and Pt contacts fabricated on n-CdTe. For such anomalous behaviour we propose two possible explanations described in Section 6.3.4. In case of surface treated in HBr-solution characteristics obtained for platinum and gold contacts are linear in reverse bias and concave under forward bias (Figure 6.13). Indium contact characteristic is slightly S-shaped and has the resistance one order of magnitude lower than other contacts. For better visibility it is depicted separately by the right axis. Despite not been ideally ohmic In_{th} contact has the best comparative quality.

On surfaces etched in HI-based etching solution again anomalous current-voltage characteristics with concave shapes are obtained under forward bias (Figure 6.14). Only In_{th} contacts behave according to Ohm's law. Resistance of the indium contact

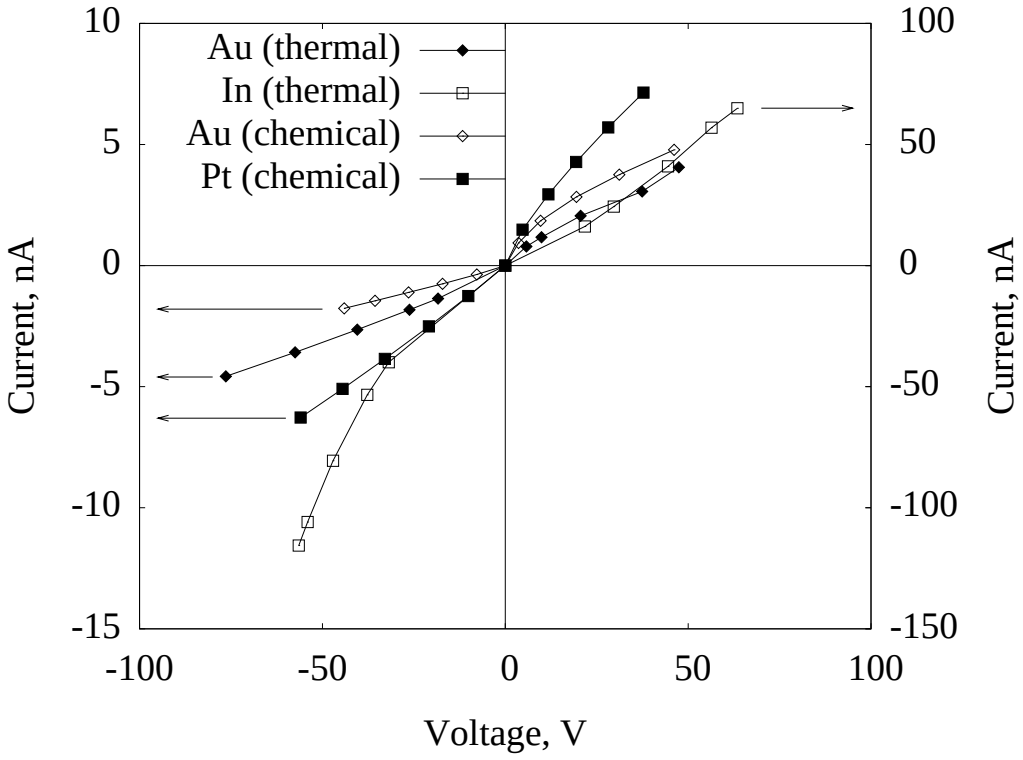

Figure 6.13: Comparison of the current-voltage characteristics of the metal-semiconductor junctions prepared on n-CdTe. Sample surface was treated in HBr solution. Contacts were prepared using various metals and techniques: ♦ - thermally evaporated Au; □ - thermally evaporated In (depicted by the right axis); ◊ - Au deposited from the aqueous solution; ■ - Pt deposited from the aqueous solution.

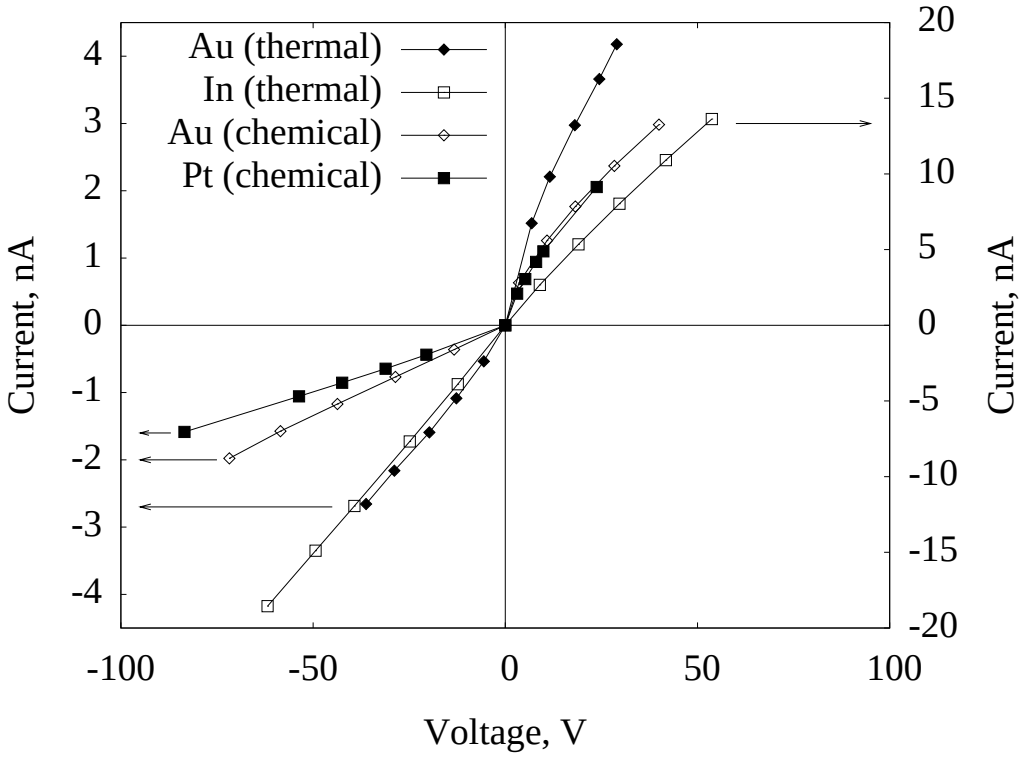

Figure 6.14: Comparison of the current-voltage characteristics of the metal-semiconductor junctions prepared on n-CdTe. Sample surface was treated in HI solution. Contacts were prepared using various metals and techniques: ♦ - thermally evaporated Au; □ - thermally evaporated In (depicted by the right axis); ◊ - Au deposited from the aqueous solution; ■ - Pt deposited from the aqueous solution.

is 5 times lower from the resistances of contacts made out of the other metals.

It is clear that on SI CdTe with n-type conductivity thermally deposited indium forms contacts with the smallest resistivity. Among the compared materials they are the only contacts to have I-V characteristics close to linear.

Contacts prepared on CdTe with p-type conductivity behave totally different. In most cases ohmic contacts are obtained. This is expressed in linear character of the I-V curves. The difference between this contacts is mainly in the resistance. Thus, this parameter is chosen to be the determinative in the comparison of various contact preparation techniques on p-type cadmium telluride.

Lets take a look at cases with different surface treatments. Contacts, prepared on p-CdTe etched in standard bromine-methanol solution, are ohmic (Figure 6.15) with exception of contacts prepared by thermal evaporation of indium. Current-voltage characteristic of this particular contact is not linear, but has an S-shape profile. For other contacts (Au_{th}, Au_{ch}, and Pt_{ch}) linear dependencies of current on applied voltage are obtained. In case of thermally evaporated gold and deposited from the aqueous solution platinum obtained I-V curves are identical with small deviations from each other. The best properties among contacts with ohmic behaviour has the gold contact deposited from solution. It has the higher slope value of the current-

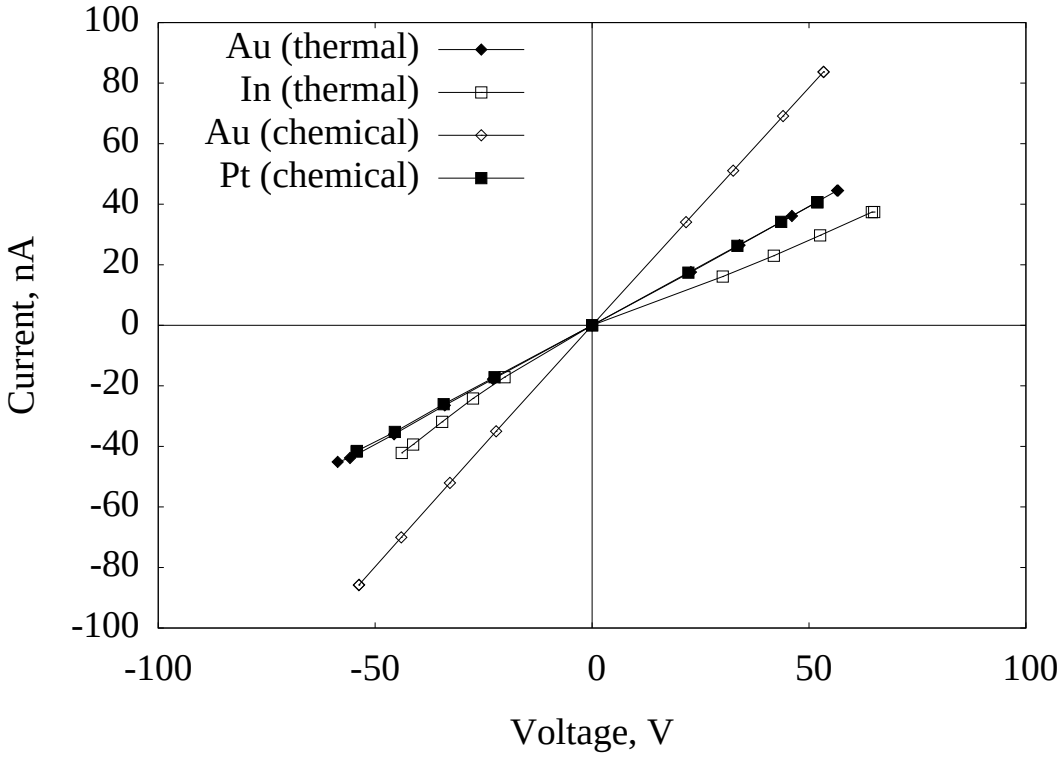

Figure 6.15: Comparison of the current-voltage characteristics of the metal-semiconductor junctions prepared on p-CdTe. Sample surface was treated in standard bromine-methanol solution. Contacts were prepared using various metals and techniques: ♦ - thermally evaporated Au; □ - thermally evaporated In; ◊ - Au deposited from the aqueous solution; ■ - Pt deposited from the aqueous solution.

voltage dependence indicating the smaller contact resistance.

Slightly different results are obtained in case of contacting surfaces treated in HBr - solution (Figure 6.16). Three types of contacts have similar properties. Namely Pt_{ch}, Au_{th}, and In_{th}. All of them show behaviour close to ohmic. Current-voltage characteristics for the first two (Pt_{ch} and Au_{th}) have small deviation from linear. I-V curve of the indium contact has slight S-shape profile. Gold contact deposited from solution proves to be the best on this particular surface. It is perfectly ohmic with the lowest resistivity among compared materials.

The worst result is obtained for the In_{th} contact prepared on p-type CdTe surface treated in HI - solution (Figure 6.17). Its resistance is found to be one order of magnitude higher than resistance of other contacts studied in our experiment. Current-voltage characteristics of Au_{th}, Au_{ch}, and Pt_{ch} contacts are close to linear and had similar slope values.

As we can see in case of p-type cadmium telluride thermally evaporated indium contacts exhibit poor behaviour, the worst among contacts compared in our investigation.

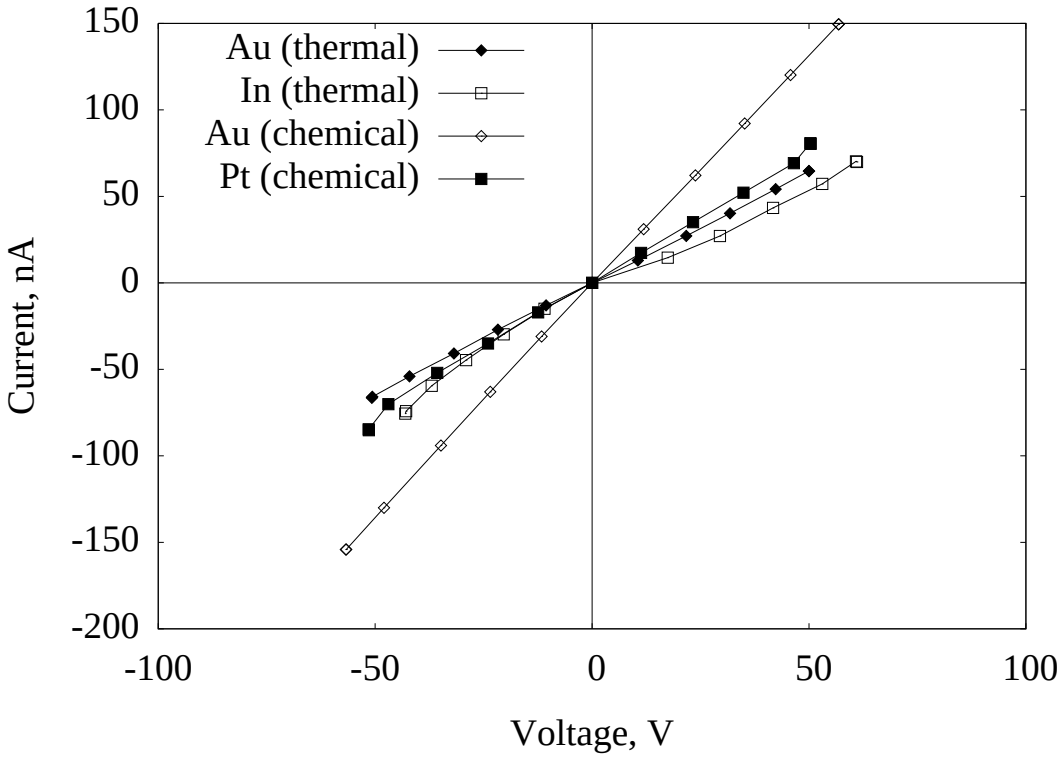

Figure 6.16: Comparison of the current-voltage characteristics of the metal-semiconductor junctions prepared on p-CdTe. Sample surface was treated in HBr solution. Contacts were prepared using various metals and techniques: ♦ - thermally evaporated Au; □ - thermally evaporated In; ◊ - Au deposited from the aqueous solution; ■ - Pt deposited from the aqueous solution.

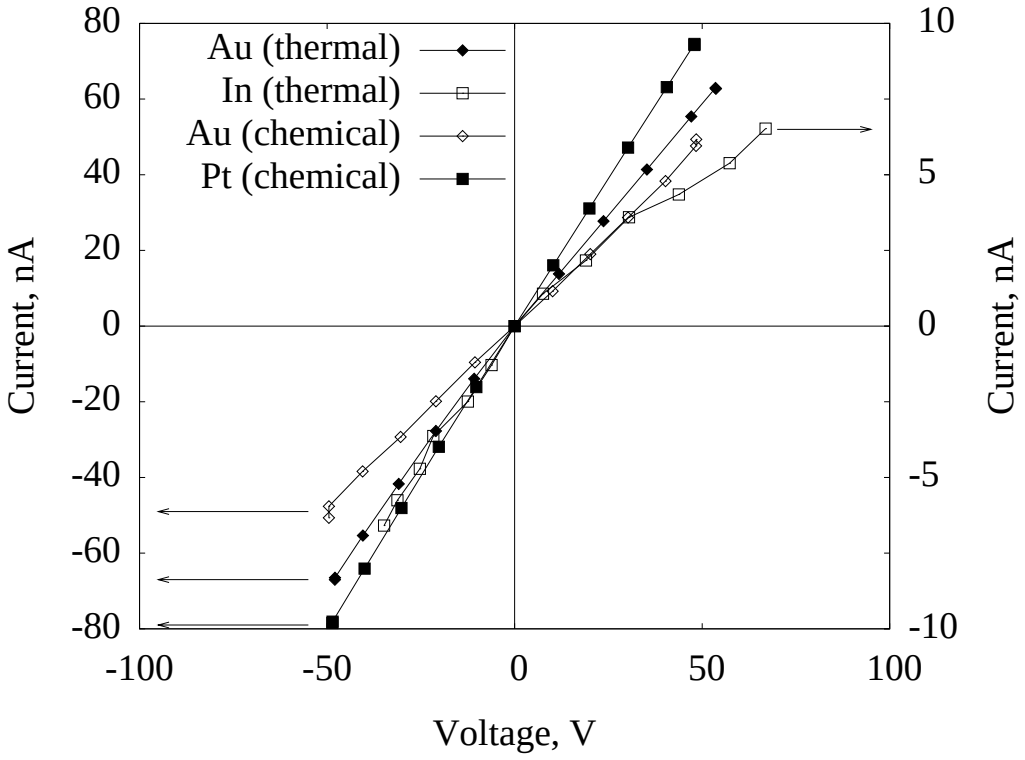

Figure 6.17: Comparison of the current-voltage characteristics of the metal-semiconductor junctions prepared on p-CdTe. Sample surface was treated in HI solution. Contacts were prepared using various metals and techniques: ♦ - thermally evaporated Au; □ - thermally evaporated In (depicted by the right axis); ◊ - Au deposited from the aqueous solution; ■ - Pt deposited from the aqueous solution.

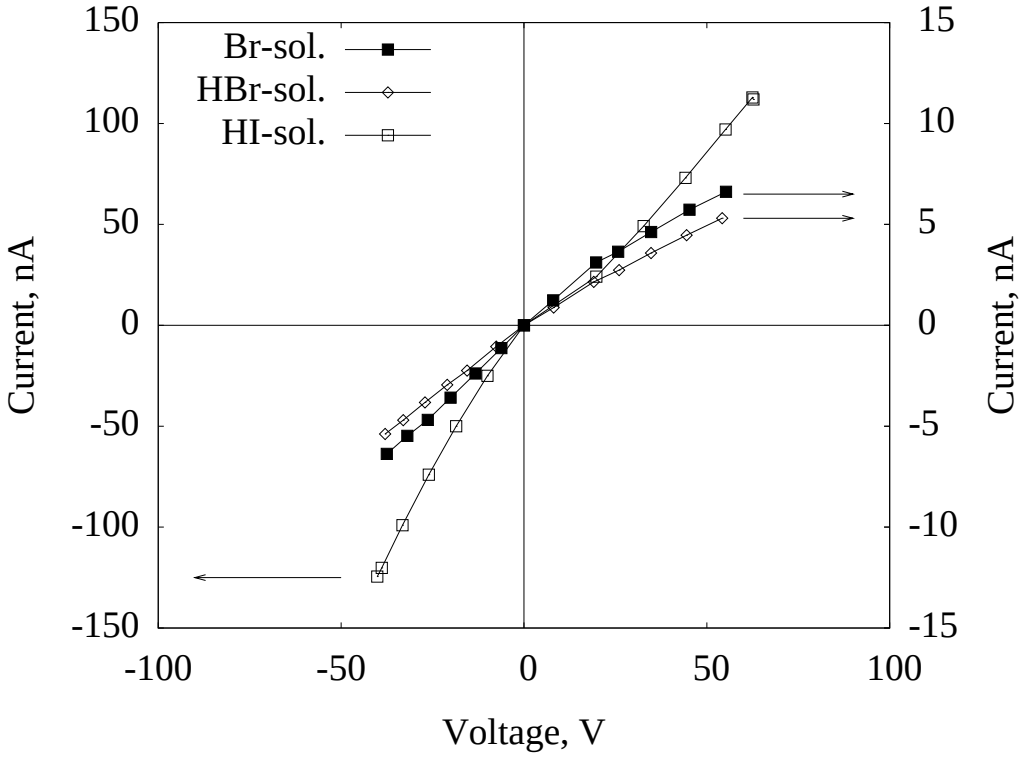

Figure 6.18: Comparison of the current-voltage characteristics of the metal-semiconductor junctions prepared on n-CdTe. Contacts were prepared by the thermal evaporation of In. Sample surface was treated in various solutions: ■ - standard bromine-methanol solution (depicted by the right axis); ◊ - HBr solution (depicted by the right axis); □ - HI solution.

6.3.3 Contact quality depending on the etching solution used for surface treatment

Contact quality is greatly influenced by the properties of the surface on which metal is deposited. Chemical polishing and etching change not only the roughness but also the composition of the surface layer. The purpose of surface treatment is to remove all inhomogeneities and oxide layer which may form barrier between the metal and bulk material. It is also important to achieve stoichiometric composition of the surface to exclude possibility of getting leakage current.

Comparison of the current-voltage characteristics of In contacts thermally deposited on the n-type CdTe samples treated in various solutions is shown in Figure 6.18. Despite of deviating from ohmic behaviour, the resistivity of the contact prepared on the sample surface etched in the HI-solution is significantly lower than in case of the use of other solutions.

Figures 6.19, 6.20, and 6.21 show current-voltage dependencies for the Au_{th}, Au_{ch}, and Pt_{ch} contacts respectively. All of them were prepared on n-type CdTe. Characteristics are similar and in all cases anomalous concave shape in positive bias region is observed. A discussion of this effect is given in Section 6.3.4.

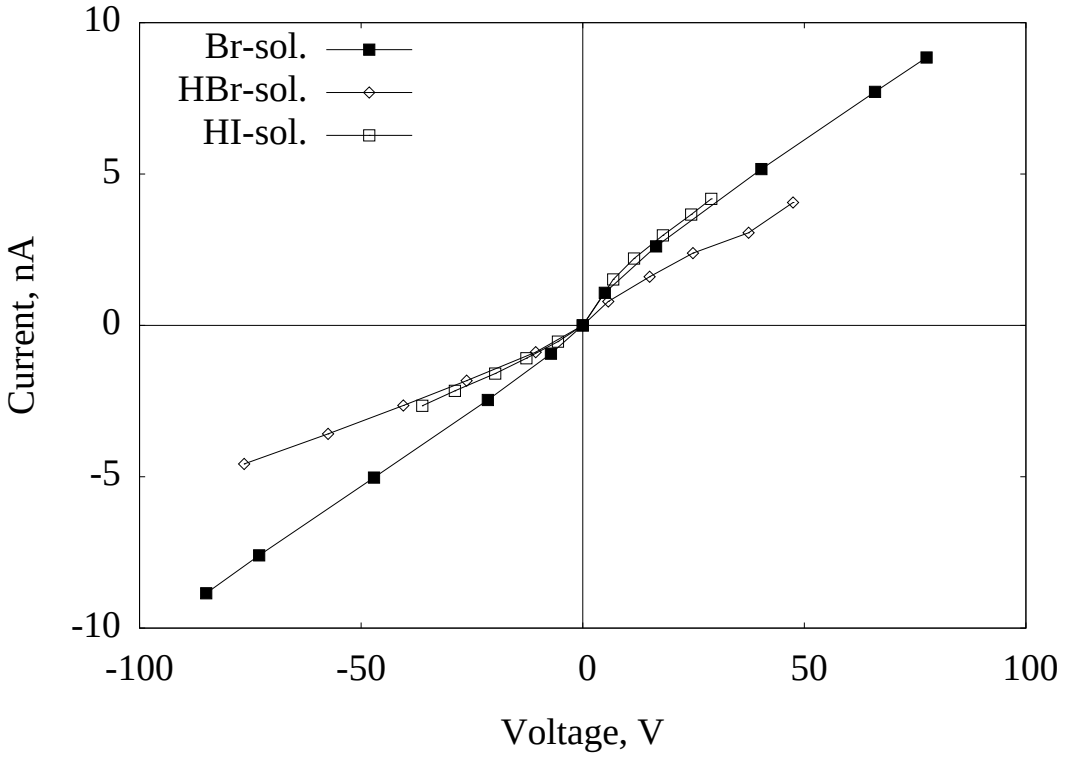

Figure 6.19: Comparison of the current-voltage characteristics of the metal-semiconductor junctions prepared on n-CdTe. Contacts were prepared by the thermal evaporation of Au. Sample surface was treated in various solutions: ■ - standard bromine-methanol solution; ◊ - HBr solution; □ - HI solution.

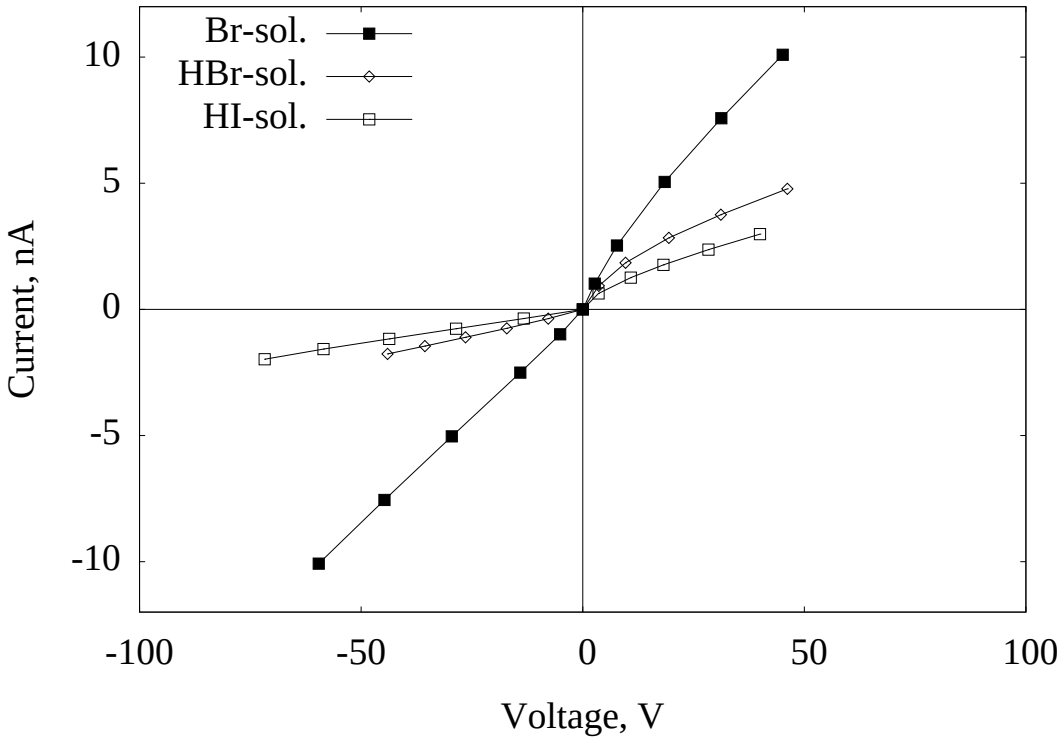

Figure 6.20: Comparison of the current-voltage characteristics of the metal-semiconductor junctions prepared on n-CdTe. Golden contacts were deposited from the aqueous solution. Sample surface was treated in various solutions: ■ - standard bromine-methanol solution; ◊ - HBr solution; □ - HI solution.

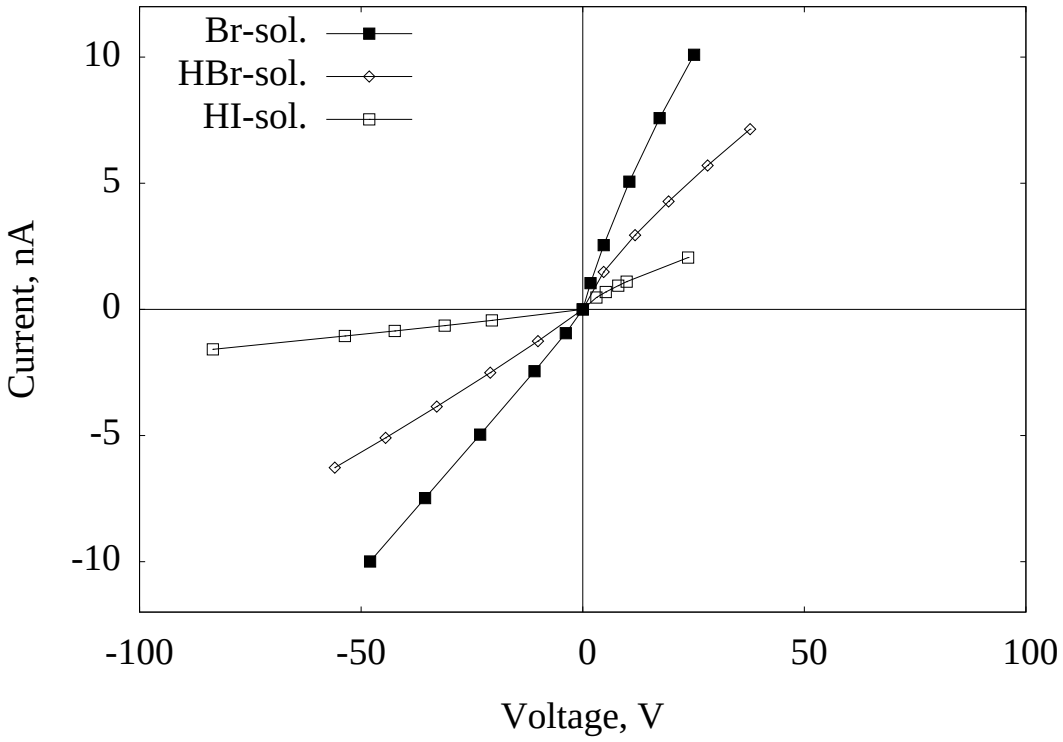

Figure 6.21: Comparison of the current-voltage characteristics of the metal-semiconductor junctions prepared on n-CdTe. Platinum contacts were deposited from the aqueous solution. Sample surface was treated in various solutions: ■ - standard bromine-methanol solution; ◊ - HBr solution; □ - HI solution.

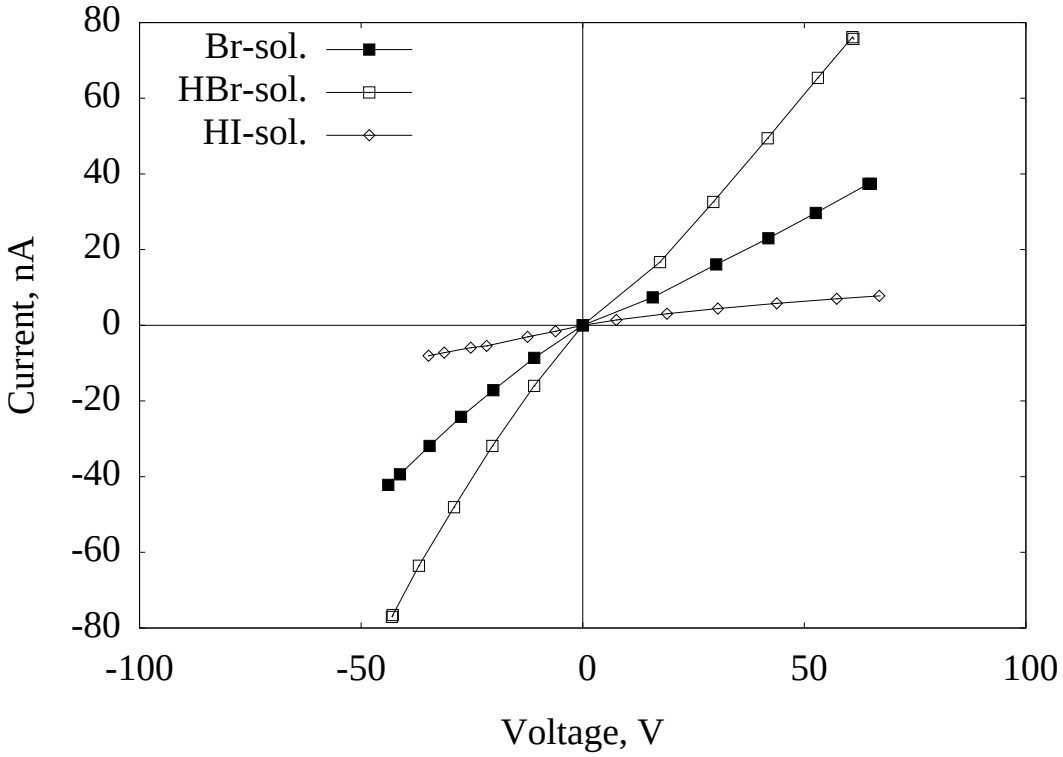

Figure 6.22: Comparison of the current-voltage characteristics of the metal-semiconductor junctions prepared on p-CdTe. Contacts were prepared by the thermal evaporation of In. Sample surface was treated in various solutions: ■ - standard bromine-methanol solution; ◊ - HBr solution; □ - HI solution.

On the Figure 6.22 typical curves of the I-V characteristics of the indium contacts fabricated on p-type CdTe are shown. All three dependencies are not linear proving that the contacts are non-ohmic.

Comparison of the properties of the thermally evaporated gold contacts on p-type CdTe does not show significant difference between compared etching solutions (Figure 6.23). All $I - V$ dependencies are linear (ohmic contacts) with the Br-solution causing slightly higher resistivity of the contacts. However, the difference is insignificant.

Comparison of the I-V characteristics of the Au contacts deposited from solution on the p-type CdTe is shown in Figure 6.24. The samples' surface was treated in three different etching solutions. Again as in the experiment with different metals, gold produces ohmic contacts in all cases. The resistivity of the contacts deposited on the surface treated in the HBr-solution is ~ 2 times lower than in case of surfaces etched by the standard Br_2-methanol solution.

Platinum contacts on three variously treated surfaces (Figure 6.25) behave similarly to the gold electrodes (Figure 6.23). In all cases they are ohmic (linear dependence). Contacts fabricated on the Br-solution treated surface are more resistive.

In order to be able to characterize contacts quantitatively we introduce here rel-

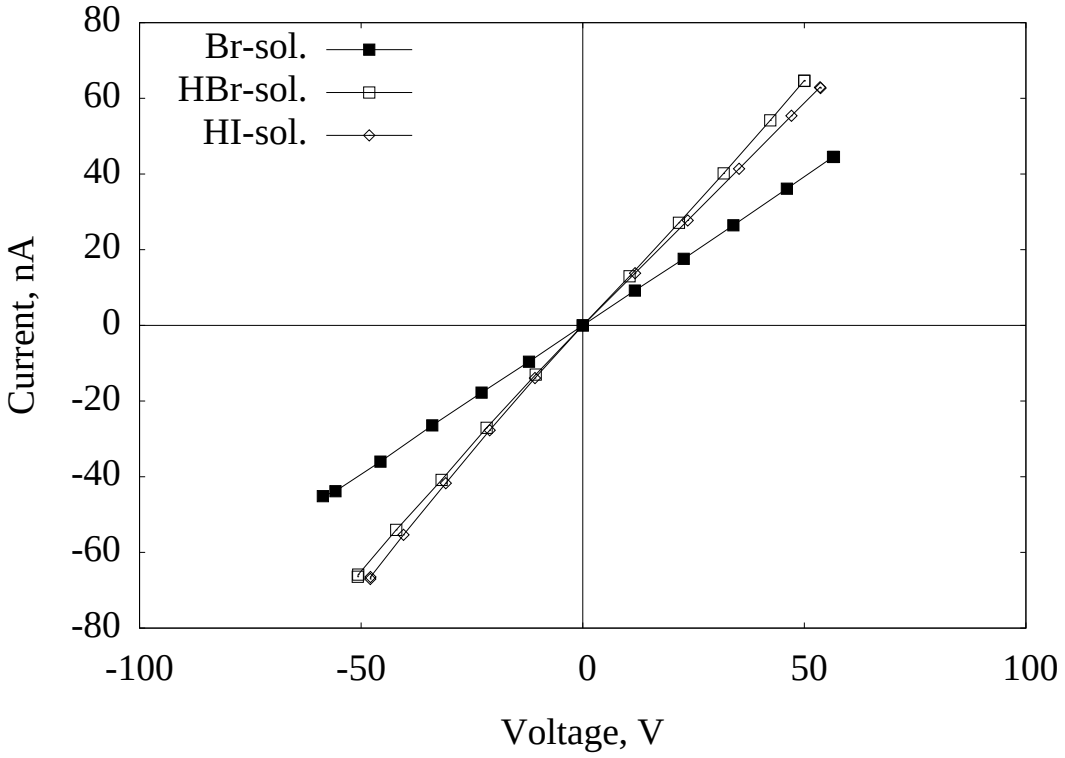

Figure 6.23: Comparison of the current-voltage characteristics of the metal-semiconductor junctions prepared on p-CdTe. Contacts were prepared by the thermal evaporation of Au. Sample surface was treated in various solutions: ■ - standard bromine-methanol solution; ◊ - HBr solution; □ - HI solution.

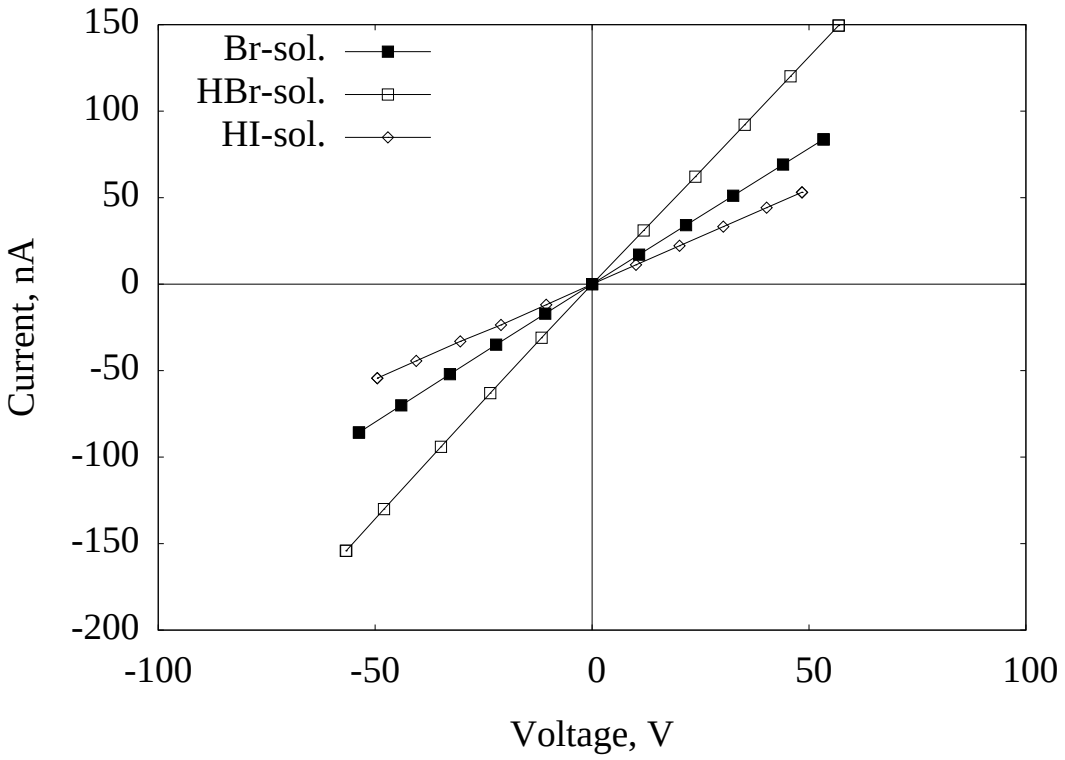

Figure 6.24: Comparison of the current-voltage characteristics of the metal-semiconductor junctions prepared on p-CdTe. Golden contacts were deposited from the aqueous solution. Sample surface was treated in various solutions: ■ - standard bromine-methanol solution; ◊ - HBr solution; □ - HI solution.

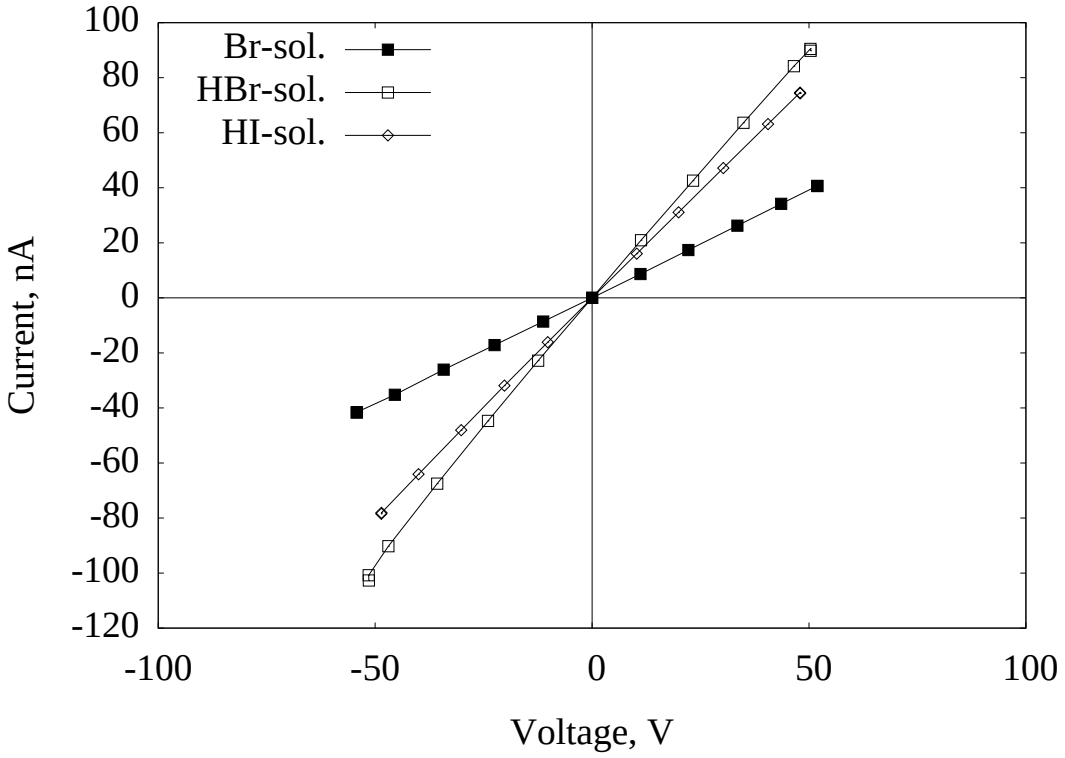

Figure 6.25: Comparison of the current-voltage characteristics of the metal-semiconductor junctions prepared on p-CdTe. Platinum contacts were deposited from the aqueous solution. Sample surface was treated in various solutions: ■ - standard bromine-methanol solution; ◊ - HBr solution; □ - HI solution.

Table 6.2: Slopes ratios in the region of positive and negative bias.

contact metal$_{dep.tech.}$	Au_{ch}		Pt_{ch}		Au_{th}		In_{th}	
conductivity type	n	p	n	p	n	p	n	p
Br - solution	0.93	1.03	0.63	0.92	1.08	0.96	1.21	1.74
HBr - solution	0.54	1.04	0.69	1.40	0.53	1.01	3.53	1.60
HI - solution	0.58	1.01	0.26	1.06	0.59	1.28	1.30	2.44

ative parameter R_{sp}. It represents contact rectification property. The value of the coefficient is a relation between the slope of I-V curve in the forward and reverse bias. Since current-voltage characteristics are not always linear the slope is calculated for the maximum voltage area. Other important parameter of the contact is its resistivity. It is not included into R_{sp}. Hence, the coefficient cannot be used for the comparison purpose. It is strictly limited for the characterization of each single contact. Slope ratios R_{sp} estimated for all current-voltage measurements are summarized in Table 6.2. Values close to 1 correspond to ohmic contacts.

The overall inspection of results allows us to conclude that the best contacts on n-type SI CdTe are prepared with In deposited thermally on the surface treated in HI-solution. On p-type SI CdTe the best option results in Au deposited chemically on the surface treated in HBr-solution. The comparison of the contact quality relevant to n-type/p-type SI CdTe proves the importance of well-known type of the conductivity to the choice of proper contact preparation treatment. In view of the fact that the treatment in HI-solution with In contact deposition improves/corrupts the quality of the contact on n-type/p-type, we can conclude that the treatment in HI-solution produces a donor-like (electron-rich) interface layer, which properly links the n-type with In having low work function. On the p-type, oppositely, the potential barrier is enhanced and the contact quality is worse. Analogous finding can be deduced for the treatment in HBr-solution where the formation of an acceptor-like (electron-pure) interface is expected.

6.3.4 Models of the anomalous concave shape of current-voltage characteristic under forward bias

The measurement of current-voltage characteristics on n-type SI CdTe under forward bias displays in most cases an anomalous concave form, which is not predicted by standard theories reviewed in textbooks. For the explanation of that effect we suggest two models outlined here.

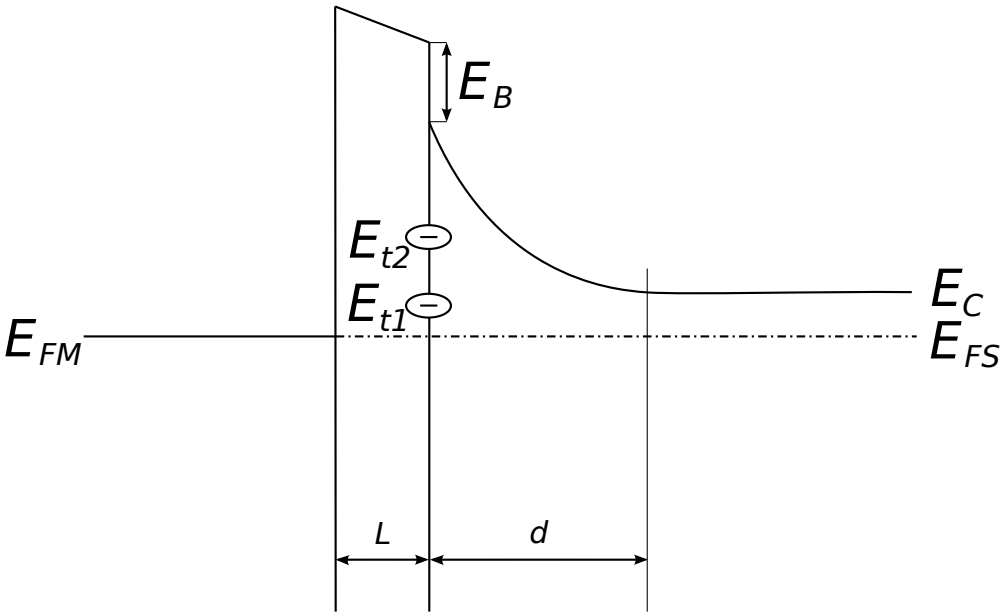

Figure 6.26: Schematic drawing of metal-insulator-semiconductor structure without applied bias. E_{t1} and E_{t2} represent trap levels discussed in model. E_B is the energy barrier. L and d are widths of insulator and depletion layers, respectively.

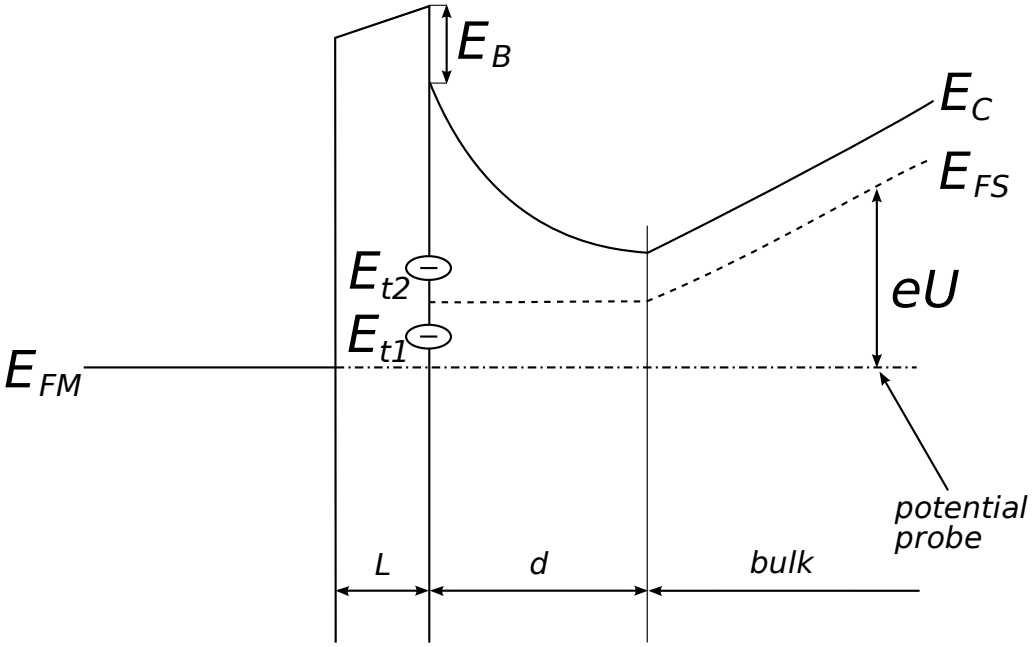

Figure 6.27: Schematic drawing of metal-insulator-semiconductor structure with applied bias U. The trap level E_{t1}/E_{t2} is occupied/empty. E_B is the energy barrier. L and d are widths of insulator and depletion layers, respectively.

Trap-mediated transport across barrier

The electric contact can be generally depicted as a metal-insulator-semiconductor (MIS) structure. The scheme of the energy band diagram without applied bias ($U = 0$) is plotted in Figure 6.26. n-type semiconductor is assumed and hole transport is neglected. The principle of the model stems from trap levels at the insulator-semiconductor interface capturing and emitting electrons both in the semiconductor and in the insulator. At least two different trap levels are assumed. Traps are characterized by energy E_t, density N_t and capture cross section s_t. Traps are set above Fermi energy at $U = 0$. Applying forward bias as depicted in Figure 6.27, traps are gradually populated with electrons and induced charge screens the electric field. The electric current is limited by the energy barrier height E_B above the conduction band edge. Electrons get over the barrier by thermal excitation. Due to low probability of their transfer across the barrier, the electron statistics both in metal and in semiconductor can be assumed close to equilibrium and the population of all states at the interface is described with unique Fermi energy E_F.

The electron transport across the barrier is described via Shockley-Read model [120]. The thermally activated electric current is given as

$$I = q\, e^{-\beta E_B} \nu_T N_c \left[\sum_i N_{ti} s_{ti} e^{\beta E_{ti}} \left(f_i - f_{0i} \right) + t \left(e^{E_F} - e^{E_{F0}} \right) \right], \tag{6.6}$$

where q is the electronic charge, $\beta = 1/k_B T$, ν_T is the thermal velocity, N_c is the effective conduction band density of states, and $f_{(0)}$ is the $(U = 0)$ trap occupancy defined by Fermi-Dirac distribution. The first term in square brackets depicts the current mediated by traps, where the capture and emission of electrons both in semiconductor and in insulator is expected. We perform only qualitative calculation here and assume for simplicity that the product $\nu_T N_c s_t$ is the same both in semiconductor and in insulator. Such assumption allows to write down I in such simple way. The second term in equation (6.6) depicts the thermally activated free electron flux, where the probability to pass S-I interface is determined by transfer coefficient t.

The voltage U corresponding to I is given by the bias on the insulator U_i and the voltage on the serial resistance of bulk SI CdTe U_b. The serial resistance has no direct effect to the model and is skipped in the calculations for simplicity. The bias on the insulator is calculated according the form

$$U_i = \frac{q\, L}{\varepsilon_0 \varepsilon_r} \sum_i N_{ti} \left(f_i - f_{0i} \right), \tag{6.7}$$

where L is the thickness of the insulator layer and ε_0 and ε_r are vacuum and relative permittivities, respectively.

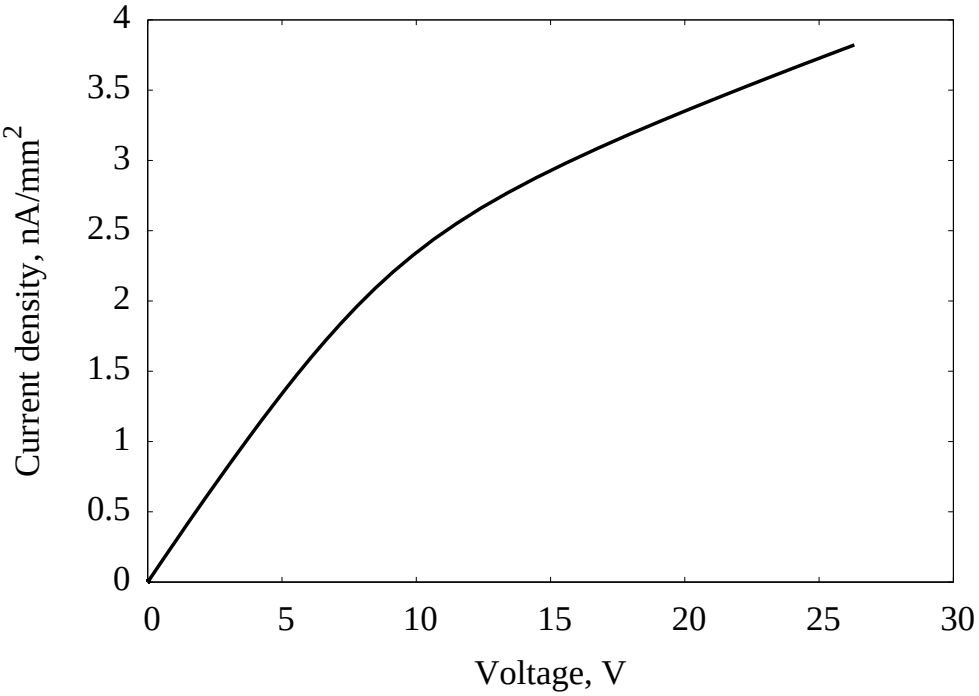

Figure 6.28: Current-voltage characteristic calculated according to trap-mediated transport across barrier theory.

The magnitude of t is critical for the validity of this model. Comparing the terms in equation (6.6) describing trap-mediated and free electron fluxes, we immediately ascertain that $t \ll N_t s_t$ must be demanded to reach the dominance of the former mechanism above the latter one. Using characteristic values for $N_t \approx 10^{12}\ cm^{-2}$ and $s_t \approx 10^{-15}\ cm^2$, $t \ll 10^{-3}$ should be assumed. Such a low t is equivalent to practically total reflection of electrons even with kinetic energy above E_B and it is hardly conceivable at usual interface. The reason why we still take the model into account is in unknown character and band structure of the insulator. t could be significantly suppressed on the interface of two materials having unlike position of the conduction band minimum in the Brillouin zone. The real energy barrier for free electrons coming from CdTe into barrier would be than larger than E_B, which represents the difference of energies of absolute minimum of conduction band of materials in touch. On the other hand, the trapping and de-trapping represents a local event being practically independent of wave vector of the electron. Consequently, in such a special case the trap-mediated transport across the barrier could dominate above the thermally activated free electron flux. Due to the band structure of insulator is not known, the possibility that t is very low remains open and should be checked in future research.

In case of t suppressed the concave shape of current-voltage characteristic is easily obtained when $s_{t1} > s_{t2}$ is set. We show in Figure 6.28 the current-voltage characteristic calculated according to equation (6.6), where $t = 0$ is used. Other

Table 6.3: Basic parameters used at the calculations according to trap-mediated transport across barrier model

parameter	value
N_{t1}	$5 \times 10^{11}\, cm^{-2}$
E_{t1}	$-0.46\, eV$
s_{t1}	$10^{-13}\, cm^2$
N_{t2}	$10^{12}\, cm^{-2}$
E_{t2}	$-0.38\, eV$
s_{t2}	$10^{-15}\, cm^2$
E_B	$0.25\, eV$
E_{F0}	$-0.6\, eV$
T	$295\, K$
ν_T	$3.8 \times 10^7\, cm/s$
ε_r	10.3
L	$1\, \mu m$

parameters are given in Table 6.3.

Extended depletion of CdTe bulk

The dominant problem in the preparation of room temperature (RT) gamma and x-ray detectors on CdTe is comprised in apparently contradictory demands of a low free carrier density, which has to be close to intrinsic carrier density $n_i \approx 10^6\, cm^{-3}$ in CdTe at RT, and the high carrier mobility-lifetime product ($\mu\tau$), which cannot be reached without significant reduction of trapping centres in the crystal. Even in the best quality materials the controlled density of shallow defects does not decrease below $10^{15}\, cm^{-3}$. To avoid considerable loss of photo-generated carriers and the depreciation of the detector, the deep trap density $N_t < 10^{13}\, cm^{-3}$ with trapping cross section $s = 10^{-15}\, cm^2$ is necessary [121].

Straightforward procedure to figure out this problem is based on the search of a deep defect with the ionization level near the middle of the band gap (mid-gap) and with $s < 10^{-17}\, cm^2$. Such defect introduced into the material at the density $N_{deep} \sim 10^{15}\, cm^{-3}$ would compensate the shallow defects and pin the Fermi energy near the mid-gap without strong trapping and degradation of $\mu\tau$ [122]. Recent experimental findings, however, do not support such a scheme and show s of mid-gap levels in the range of $10^{-14} - 10^{-13}\, cm^2$ or even up to $10^{-11}\, cm^2$ [123, 124]. The fact that high quality detectors on CdTe exist points to some underestimated processes at the detector fabrication, which result in significant shallow level self-compensation and a formation of SI CdTe even if $N_t < 10^{12}\, cm^{-3}$. The assumption of a very low N_t in the SI CdTe bulk forms the basis of this model.

The measurement of the contact under forward bias entails the reverse bias applied to the counterpart. Due to the depletion layer spreads from that reverse

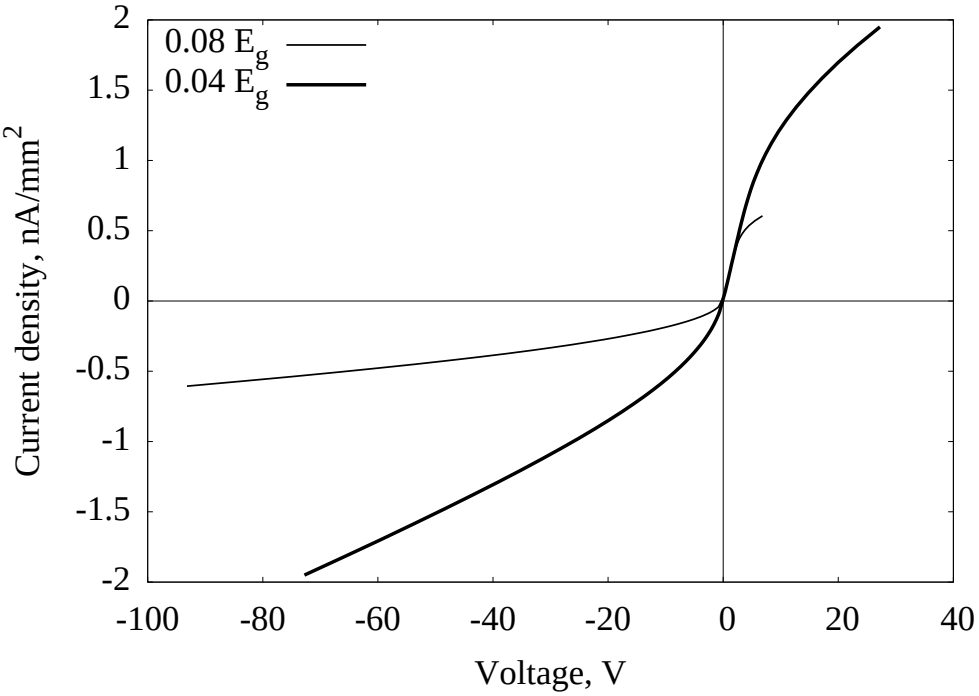

Figure 6.29: Current-voltage characteristics calculated according to extended depletion model. The labels show the band banding at the surface forming depletion layer.

contact into the bulk, it can reach at large enough voltage the area of the potential contact and affect the resistivity adjudged to the contact under forward bias.

For the analysis of the effects outlined above we have utilized the experience gained by our group at the research of SI CdTe in the past 15 years and an extensive library of computer programs for simulation of transport processes in SI CdTe. The electron transport in the structure with extended depletion region was simulated with the code solving self-consistently one-dimensional coupled drift-diffusion and Poisson's equations including generation-recombination processes on impurity levels described within Hall-Shockley-Read model. Details of the approach are presented in [125]. Band-bending below contacts is set by Fermi energy at the surface. Two examples of the calculated current-voltage characteristics are plotted in Figure 6.29. Parameters used at the calculations are given in Table 6.4. The second deep level put significantly below Fermi energy was used to increase the electric current without enormous charging of the level. It is apparent, that the calculated curves depict well the measured data and the model can be used as good basis for the explanation of the observed effect.

Summarizing positives and negatives of suggested models, both models explain the concave shape in current-voltage characteristics under forward bias. The former model suffers from necessary suppression of free-electron transport through the insulating barrier, the latter model requests very low density of deep levels to allows

Table 6.4: Basic parameters used at the calculations according to extended depletion theory. Items (a), (b) correspond to thin and thick lines in Figure 6.29, respectively.

parameter	value
sample thickness	$2\,mm$
1^{st} deep level energy	$E_c - 0.46\,E_g$
1^{st} deep level density	$10^{11}\,cm^{-3}$
1^{st} deep level electron capture cross section	$10^{-12}\,cm^2$
1^{st} deep level hole capture cross section	$10^{-12}\,cm^2$
2^{nd} deep level energy	$E_c - 0.6\,E_g$
2^{nd} deep level density	$10^{14}\,cm^{-3}$
2^{nd} deep level electron capture cross section	$10^{-11}\,cm^2$
2^{nd} deep level hole capture cross section	$10^{-13}\,cm^2$
equilibrium Fermi energy E_{F0}	$E_c - 0.42\,E_g$
Fermi energy at the surface	$E_c - 0.5\,E_g$ (a)
	$E_c - 0.46\,E_g$ (b)

the formation of extensive depletion layer at the reversed contact.

6.3.5 Capacitance-voltage measurements

All treatments of the CdTe samples were performed in the air atmosphere. Under such conditions surface is covered with thin oxide layer. By fabricating metal contacts on such surface metal-oxide-semiconductor (MOS) structure is formed. The exact thickness of the oxide layer is not known. Moreover, the exact structure of the semiconductor surface is unknown.

Properties of interface traps distributed in the semiconductor band-gap are conveniently studied with admittance measurements [126]. Capacitance-voltage measurements were performed as described in Section 5.5.5. For the admittance measurement we have prepared samples with design outlined in Figure 6.30, which is conventionally used in this case. Samples dimensions were $5 \times 5 \times 2\,mm$. Contacts 1 and 2 were $4 \times 4\,mm$. N-type SI CdTe sample contacted with gold to build depletion layer at the interface have been chosen. Due to the apparatus allowed to apply maximum 10 volts to the circuit, the bias did not manipulate interface charge markedly and no voltage dependence has been observed. Thus, we analyse only frequency dependence in this chapter.

Collected data are analysed according equivalent circuit plotted in Figure 6.31 characterized by the admittance

$$Y_0 = G + 2\pi j f C. \tag{6.8}$$

The course of the capacity and resistivity evaluated according the equivalent circuit is shown in Figures 6.32 and 6.33. The capacitance C has been excellently fit with

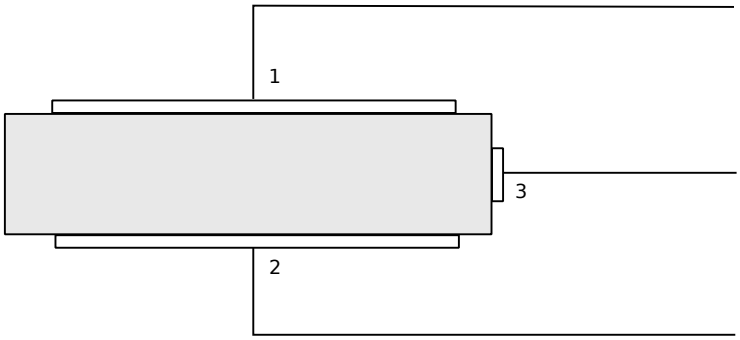

Figure 6.30: Sample design with three gold contacts for $C - V$ measurements. Alternating current is applied on contacts $1 - 2$. Voltage is measured on $1 - 3$ contacts.

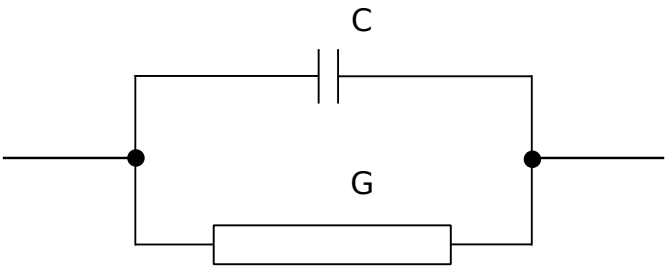

Figure 6.31: Equivalent circuit used by the Agilent E4980A Precision LCR Meter for the data analysis.

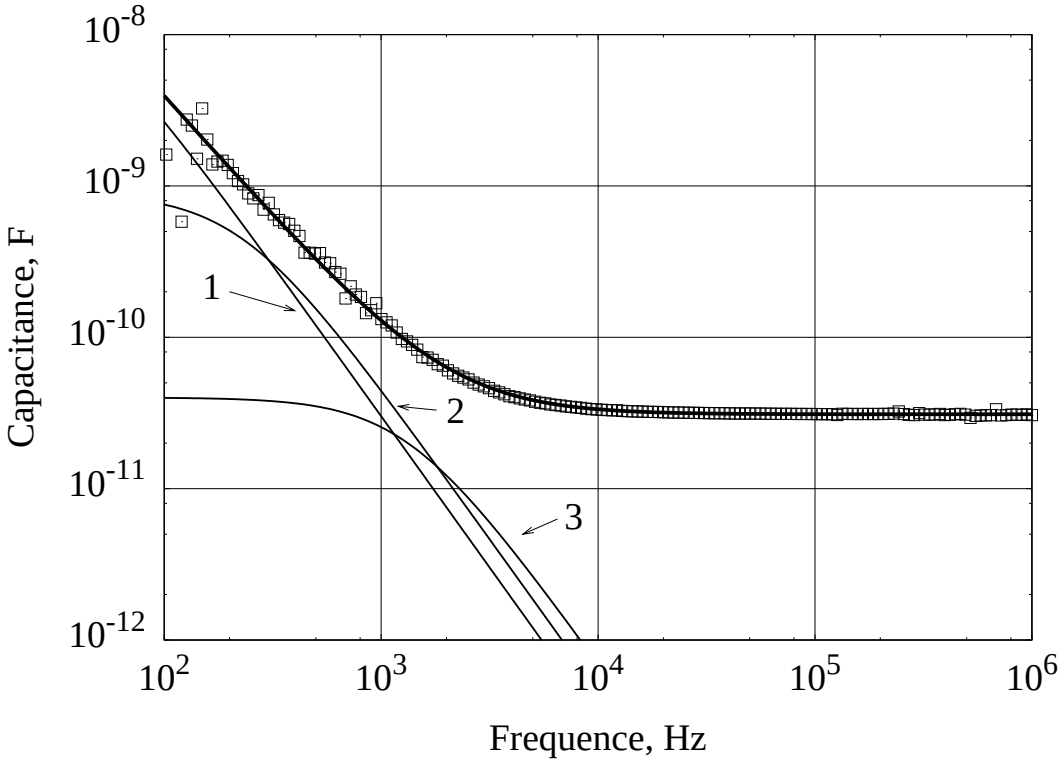

Figure 6.32: Dependence of contact capacitance on frequency. Experimental data are depicted with open squares. Thick line represents theoretical fit. 1, 2, 3 correspond to the first, second and third trap levels, respectively.

trial function

$$C_t = 6.1 \times 10^{-6} f^{-1.6} + 3.1 \times 10^{-11}. \tag{6.9}$$

Two samples have been measured and similar characteristics were obtained.

For the interpretation of measured data we follow [126] and describe the structure according MOS (Metal-Oxide-Semiconductor) equivalent circuit as shown in Figure 6.34, where parallel combination of G_i, C_i branches represent i^{th} trap level localized near interface. C_i is the capacitance of the i^{th} interface level, and G_i is the corresponding electron capture conductance. The admittance of the circuit is calculated according the form

$$Y = \sum_i \frac{(2\pi f C_i)^2/G_i}{1 + (2\pi f C_i/G_i)^2} + 2\pi j f \left(C_0 + \sum_i \frac{C_i}{1 + (2\pi f C_i/G_i)^2} \right), \tag{6.10}$$

where the sum counts respective branches of the circuit representing distinct trap levels. Comparing real and imaginary parts of equations (6.8) and (6.10), we immediately obtain G and C corresponding to the equivalent circuit.

Very good fit of both C and G presented in Figures 6.32 and 6.33 has been obtained taking three trap levels with parameters shown in Table 6.5. The parallel

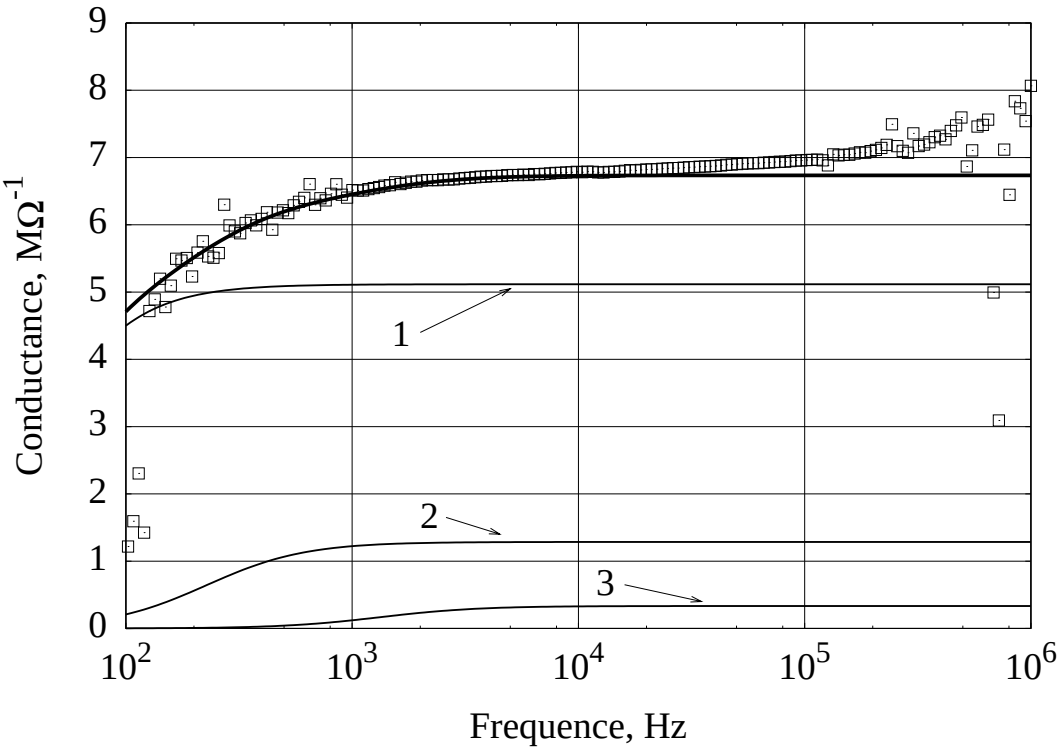

Figure 6.33: Dependence of contact resistance on frequency. Experimental data are plotted with open squares. Thick line shows theoretical fit. 1, 2, 3 correspond to the first, second and third trap levels, respectively.

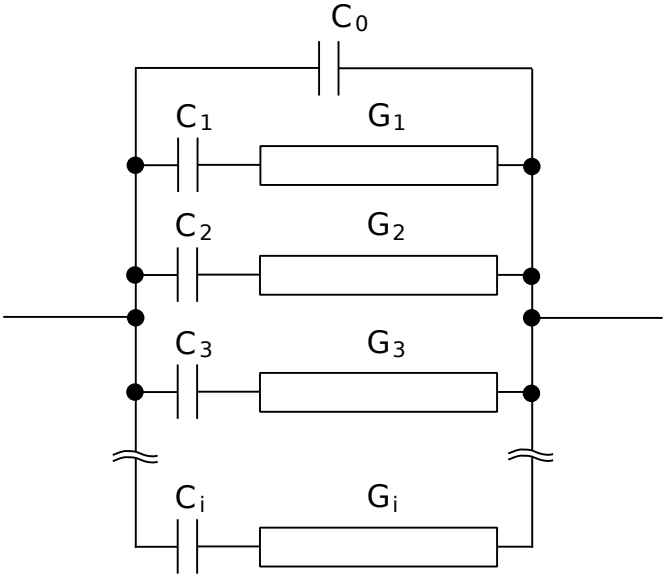

Figure 6.34: Alternative equivalent circuit used for the admittance analysis.

Table 6.5: Fitting parameters for the capacitance and admittance of the gold contacts on SI CdTe.

parameter	value
C_1	$28\,nF$
G_1	$6.5 \times 10^{-6}\,\Omega^{-1}$
C_2	$0.6\,nF$
G_2	$8.6 \times 10^{-7}\,\Omega^{-1}$
C_3	$40\,pF$
G_3	$4.0 \times 10^{-7}\,\Omega^{-1}$

capacitance $C_0 = 31\,pF$. The effect of respective trap levels to total C and G represented by corresponding summands in equation (6.10) is plotted by the lines marked 1, 2, 3 as well. Alternatively, the trap levels can be characterized by time constant representing respective level occupancy rates $\tau_i = C_i/G_i$, which result $\tau_1 = 4.3\,ms$, $\tau_2 = 0.7\,ms$, and $\tau_3 = 0.1\,ms$. Detailed microscopic interpretation of evaluated data is impossible at the moment. We recommend to extend outlined research to larger interval of biases applied to the sample and to complete temperature changes as well. Consecutively, varied external parameters will affect the effective circuit characteristics, which allow to establish the trap properties.

6.4 Detector response

As a final step of this research a gamma-ray spectra were measured on studied crystals in pulse-mode at room temperature. For the experiment two detectors were made from SI indium doped n-type and chlorine doped p-type CdTe. Detector dimensions were $5 \times 5 \times 1\,mm^3$. Surface was treated in HI-based etching solution. Indium electrodes ($4 \times 4\,mm^2$) were thermally fabricated on the opposite faces of the semiconductor. Since CdTe is sensible to visible light, it was shielded from light. Electric field was applied between the electrodes using an outside bias from Keithley 2410 1100V SourceMeter. The distance between gamma-ray source and CdTe was $1\,cm$. ^{241}Am standard source was placed at the upper part of an experiment cell. The source emit low-energy gamma rays that are suitable for the experiment. Generated current was integrated by a charge sensitive Ortec Preamplifier to measure the total charge induced by the outside radiation and produced a voltage pulse with amplitude proportional to the total induced charge. Shaping time was set at $0.5\,\mu s$. Obtained voltage pulse was amplified 1000 times with Ortec 671 Amplifier. Pulse height spectra were acquired with a Ortec EASY-MCA multichannel analyser.

Results obtained from the measurements are depicted in Figures 6.35 and 6.36. Spectra from the commercial detector (Amptek [127]) is given for the comparison on Figure 6.37. Our p-type sample is not sensitive to the gamma-rays. Three values

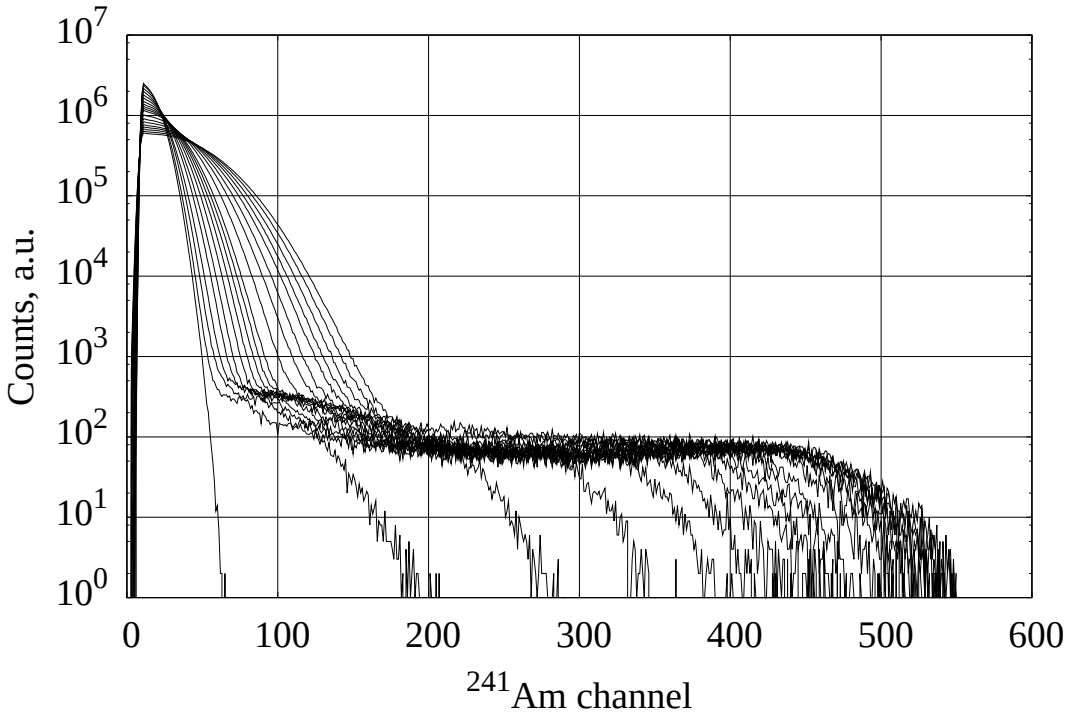

Figure 6.35: Room temperature ^{241}Am response of the indium doped n-type CdTe. External bias from 0 to $300\,V$ was used. Between 0 and $100\,V$ step was $10\,V$. Between 100 and $300\,V$ step was $25\,V$.

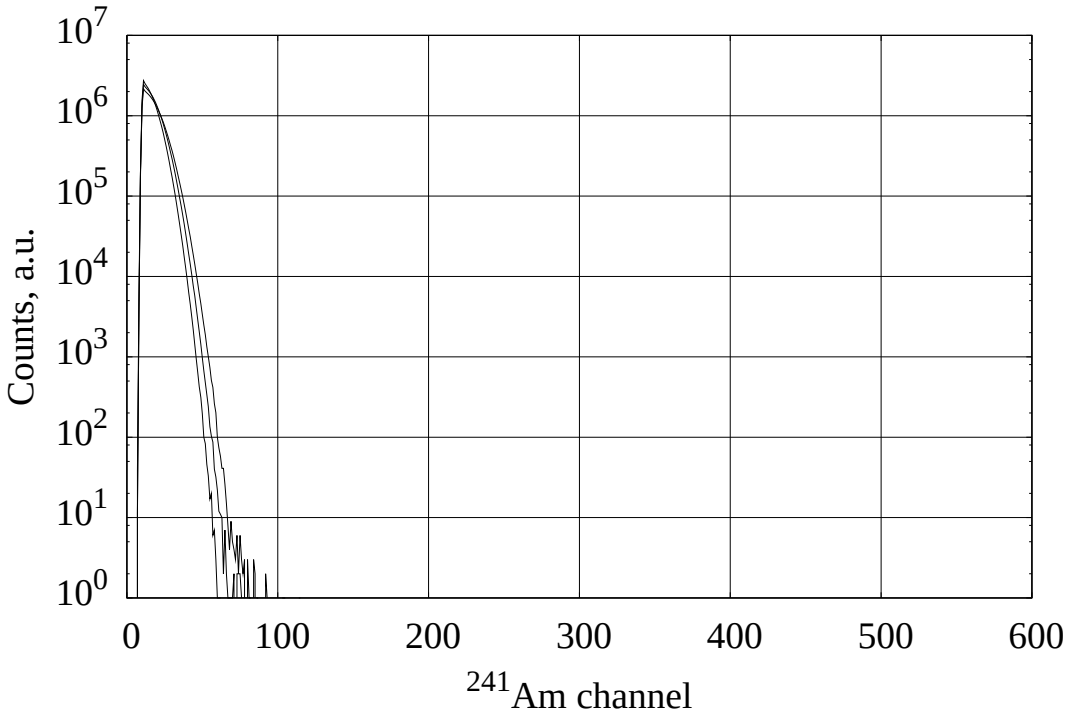

Figure 6.36: Room temperature ^{241}Am response of the chlorine doped p-type CdTe. External bias 100, 200, and $300\,V$.

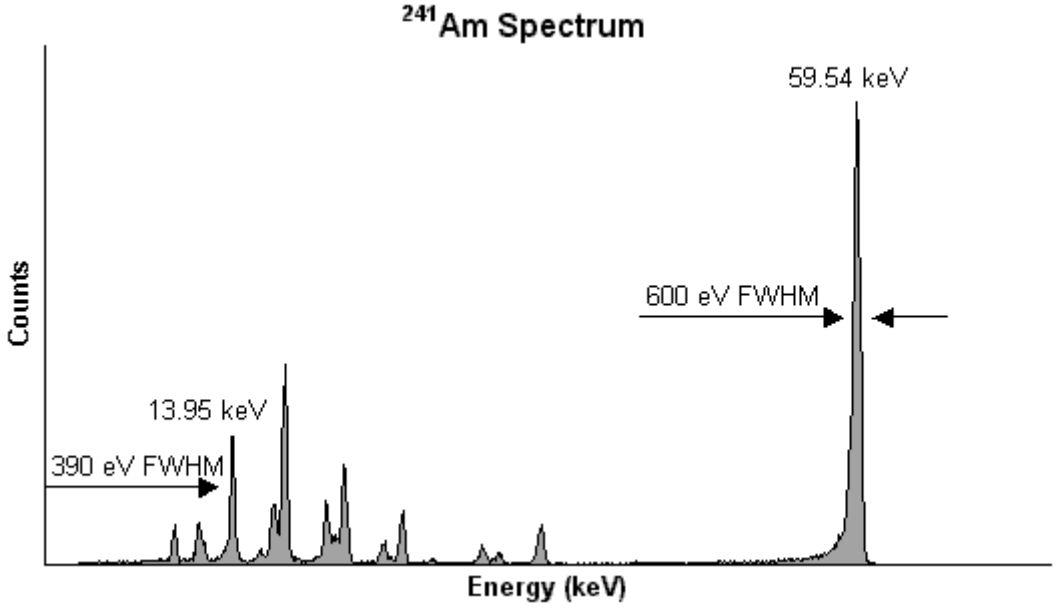

Figure 6.37: Detection spectra from AMPTEK commercial detector observed using ^{241}Am source [127].

of external bias were used - 100, 200, and 300 V. However, no charge was collected on this particular sample (Figure 6.36). n-type sample behave different. Applied voltage was from 0 to 100 V with 10 V step and from 100 to 300 V with 25 V step. Sample is sensitive to the gamma-rays. Without external bias only X-ray peak (at the left side of the chart) is registered. However, even 10 V is enough to observe a signal from gamma photon. Detection spectra depend on applied bias. With bias increase the signal is shifted to the higher channels. Higher bias allows to collect larger charge before it recombines inside the bulk material. Signal saturates at $U_{sat} \approx 150\,V$. At this value of the voltage most of the electron-hole pairs are registered on the electrodes. Detector properties are characterized by the mobility-lifetime product $\mu\tau$, which is calculated according the form

$$\mu\tau = \frac{l^2}{U_{sat}}, \tag{6.11}$$

where l is the detector thickness. For our n-type sample $\mu\tau \approx 6 \times 10^{-5}\,cm^2/V$. This $\mu\tau$ characterizes relatively bad detector material and cannot be compared with commercial products (Figure 6.37). Taking into account that sample was not specially picked, the observed detecting property is pretty good.

Conclusions

The aim of this work was to perform a complex investigation of semi-insulating CdTe for the gamma ray detector application starting from the crystal growth and finishing with device characterization.

In-situ high temperature measurements of Hall effect and conductivity were made on SI CdTe. Surface treatments in non-standard etching solutions was done. Properties of various contacts fabricated on such surfaces were investigated by the current-voltage measurements and compared mutually. Capacitance-voltage dependencies for the contacts were collected as well. Finally detection spectra were measured on the self-made detector. Additional techniques were used in parallel to have constant control on various samples' properties.

The main results of the work are:

- Transport properties in SI Cl-doped CdTe at high temperatures were studied. The chemical diffusion coefficient for the chlorine doped CdTe was established.
- Activation energy of diffusion $2.55\,eV$ in CdTe:Cl was found to be significantly larger relatively to $1.15\,eV$ in undoped CdTe.
- In compensated CdTe:Cl the densities of the principal point defects change only weakly and Cl_{Te}^{+} are compensated by A^{-} and V_{Cd}^{2-} acceptors.
- The proximity of σ relaxed after P_{Cd} up/down step proved that there is no effect of the step direction.
- Experimental set-up for current-voltage measurements on semi-insulating samples was build. Sophisticated data acquisition software was developed especially for the new set-up.
- The overall inspection of results allows us to conclude that the best contacts on n-type SI CdTe are prepared with In deposited thermally on the surface treated in HI-solution. On p-type SI CdTe the best option results in Au deposited chemically on the surface treated in HBr-solution. The comparison of the contact quality relevant to n-type/p-type SI CdTe proves the importance of well-known type of the conductivity to the choice of proper contact preparation treatment.

- In view of the fact that the treatment in HI-solution with In contact deposition improves/corrupts the quality of the contact on n-type/p-type, we can conclude that the treatment in HI-solution produces a donor-like (electron-rich) interface layer, which properly links the n-type with In having low work function. On the p-type, oppositely, the potential barrier is enhanced and the contact quality is worse.

- Analogous finding can be deduced for the treatment in HBr-solution where the formation of an acceptor-like (electron-pure) interface is expected.

- The measurement of current-voltage characteristics on n-type SI CdTe under forward bias displays in most cases an anomalous concave form, which is not predicted by standard theories reviewed in textbooks. For the explanation of that effect we suggest two models: a) trap-mediated transport across barrier; b) extended depletion of CdTe bulk.

- Theory of the interface traps distributed in the semiconductor band-gap was successfully used to explain capacitance-voltage measurements.

- Gamma ray spectra measured on the self-made detector showed that our samples are capable to detect even using low external bias ($10\,V$).

In future continuation of the research high-temperature electrical measurements should be made in wider temperature and pressure intervals. Both chlorine and indium crystals with different degree of doping should be used. Noise measurements should be applied for the study of the quality of the contacts. Also temperature dependences of the contacts properties should be investigated. Capacitance measurements at applied voltage up to $100\,V$ should be performed.

References

[1] K. Abbas, G. Nicolaou, D. Pellottiero, P. Schwalbach, and L. Koch, *Nucl. Instrum. and Methods*, vol. A376, p. 248, 1996.

[2] R.B. James, T.E. Schlesinger, J. Lund, and M. Schieber, *CdTe Nuclear Detectors and Applications*, vol. 43 of *Semiconductors and Semimetals*, p. 606, New York: Academic Press, 1995.

[3] M. Cuzin, F. Glasser, R. Mermet, N. Meunier, O.C. Peyret, and P. Rambaud, *Proc. SPIE*, vol. 2278, p. 21, 1994.

[4] C. Szeles, *Phys. Stat. Sol. B*, vol. 241, p. 783, 2004.

[5] R. Grill, J. Franc, P. Höschl, I. Turkevych, E. Belas, and P. Moravec, *IEEE Trans. Nucl. Sci.*, vol. 52, p. 1925, 2005.

[6] C. Scharager, P. Siffert, P. Höschl, P. Moravec, and M. Vaněček, *Phys. Stat. Sol. A*, vol. 66, p. 87, 1981.

[7] S.A. Medvedev, Yu.V. Klevkov, K.V. Kiseleva, and N.N. Sentyurina, *Inorg. Mater.*, vol. 8, p. 1064, 1972.

[8] M. Wienecke, H. Bereger, and M. Schenk, *Mater. Sci. Eng. B*, vol. 16, p. 219, 1993.

[9] M.L. Cohen and J.R. Chelikowsky, *Electronic Structure and Optical Properties of Semiconductors*, New York: Springer, 1988.

[10] R.F. Brebrick and R. Fang, *J. Phys. Chem. Solids*, vol. 57, p. 451, 1996.

[11] D. de Nobel, *Philips Res. Repts.*, vol. 14, p. 361, 1959.

[12] J.B. Mullin and B.W. Straughan, *Rev. Phys. Appl.*, vol. 12, p. 105, 1977.

[13] H.M. Hobgood, B.W. Swanson, and R.N. Thomas, *J. Cryst. Growth*, vol. 85, p. 510, 1987.

[14] H. Yamashita and S. Ibuki, *J. Phys. Soc. Jpn.*, vol. 13, p. 226, 1958.

[15] W.W. Piper and S.J. Polich, *J. Appl. Phys.*, vol. 32, p. 1278, 1961.

[16] K. Zanio, *Cadmium Telluride*, vol. 13 of *Semiconductors and Semimetals*, Orlando: Academic Press, 1978.

[17] P. Cheuvart, U. El-Hanani, D. Schneider, and R. Triboulet, *J. Cryst. Growth*, vol. 101, p. 270, 1990.

[18] P. Brunet, A. Katty, D. Schneider, A.Tromsoncarli, and R. Triboulet, *Mat. Sci. and Eng. B*, vol. 16, p. 44, 1993.

[19] F.A. Kröger, *The Chemistry of Imperfect Crystals*, vol. 195, New York: American Elsevier Comp., 1973.

[20] M.A. Berding, *Phys. Rev. B*, vol. 60, p. 8943, 1999.

[21] R. Grill, J. Franc, P. Höschl, I. Turkevych, E. Belas, P. Moravec, M. Fiederle, and K. W. Benz, *IEEE Trans. Nucl. Sci.*, vol. 49, p. 1270, 2002.

[22] P. Emanuelsson, P. Omling, B.K. Meyer, M. Wienecke, and M. Schenk, *Phys. Rev. B*, vol. 47, p. 15578, 1993.

[23] M.A. Berding, M. van Schilfgaarde, and A. Sher, *Phys. Rev. B*, vol. 50, p. 1519, 1994.

[24] D.M. Hofmann, P. Omling, and H.G. Grimmeiss, *Phys. Rev. B*, vol. 45, p. 6247, 1992.

[25] S.S. Chern, H.R. Vydyanath, and F.A. Kröger, *J.Sol.State Chem.*, vol. 14, p. 33, 1975.

[26] S.S. Devlin, *Phisics and Chemistry of of II-VI Compounds*, Amsterdam: North-Holland, 1967.

[27] D.L. Rode, *Phys. Rev. B*, vol. 2, p. 4036, 1970.

[28] D. Kranzer, *Phys. Stat. Sol. A*, vol. 26, p. 11, 1974.

[29] B. Segall, M.R. Lorenz, and R.E. Halsted, *Phys. Rev.*, vol. 129, p. 2471, 1963.

[30] S. Yamada, *J. Phys. Soc. Japan*, vol. 15, p. 1940, 1960.

[31] I. Turkevych, R. Grill, J. Franc, E. Belasand P. Höschl, and P Moravec, *Semicond. Sci. Technol.*, vol. 17, p. 1064, 2002.

[32] F.T.J. Smith, *Trans. Metall. Soc.*, vol. 1, p. 617, 1970.

[33] J. Franc, R. Grill, L. Turjanska, P. Höschl, E. Belas, and P. Moravec, *J. Appl. Phys.*, vol. 89, p. 786, 2001.

[34] F. Low and D. Pines, *Phys. Rev.*, vol. 98, p. 414, 1955.

[35] L. Darken, *Trans. Inst. Min. Metall.*, vol. 175, p. 184, 1948.

[36] S.S. Chern and F.A. Kröger, *J.Sol.State Chem.*, vol. 14, p. 44, 1975.

[37] R.C. Whelan and D. Shaw, *Phys. Status Solidi B*, vol. 29, p. 145, 1968.

[38] K.R. Zanio, *Appl. Phys. Lett.*, vol. 15, p. 260, 1969.

[39] Yu.V. Rud' and K.V. Sanin, *Soviet Phys. Semicond.*, vol. 5, p. 244, 1969.

[40] K.R. Zanio, *J. Appl. Phys.*, vol. 41, p. 1935, 1970.

[41] Yu.V. Rud' and K.V. Sanin, *Soviet Phys. Semicond.*, vol. 6, p. 764, 1972.

[42] Yu.V. Rud and K.V. Sanin, *Inorg. Mater.*, vol. 10, p. 839, 1974.

[43] S.S. Chern and F.A. Kröger, *J.Sol.State Chem.*, vol. 14, p. 299, 1975.

[44] H.H. Woodbury, *Phys. Rev.*, vol. 134, p. A492, 1964.

[45] P.M. Borsenberger, D. Stevenson, and R.A. Burmeister, *II-VI Semiconducting Compound, International Conference, New York: W. A. Benjamin, Inc.*, p. 439, 1967.

[46] R.C. Whelan and D. Shaw, *II-VI Semicond. Comp.*, p. 451, 1967.

[47] H.H. Woodbury and R.B. Hall, *Phys. Rev.*, vol. 157, p. 641, 1967.

[48] D.A. Stevenson, *In: D.S. Shaw, Editor, Atomic Diffusion in Semiconductors, Plenum, London*, p. 494, 1973.

[49] P.M. Borsenberger and D.A. Stevenson, *J. Phys. Chem. Solids*, vol. 29, p. 1277, 1968.

[50] R. Grill, E. Belas, M. Bugár, P. Höschl, B. Nahlovskyy, P. Fochuk, O. Panchuk, A. E. Bolotnikov, and R. B. James, *IEEE Trans. Nucl. Sci.*, vol. 56, p. 1763, 2009.

[51] R. Grill, E. Belas, J. Franc, P. Höschl, and P. Moravec, *Nucl. Instr. and Methods*, vol. A591, p. 218, 2008.

[52] D.R. Lide, Ed., *CRC HadNicollianbook of Chemistry and Physics*, CRC Press, Boca Raton, FL, 1998.

[53] C. Debiemme-Chouvy, F. Iranzo Marin, U. Roll, M. Bujor, and A. Etcheberry, *Surf. Sci.*, vol. 352, p. 495, 1996.

[54] D.A. Slater, Y. Luo, and R.M. Osgood Jr., *J. Cryst. Growth*, vol. 159, p. 754, 1996.

[55] I.M. Dharmadasa, *Prog. Cryst. Growth Charact. Mater.*, vol. 39, p. 249, 1998.

[56] F.X. Wagner and D. Sands, *Thin Solid Films*, vol. 358, p. 6, 2000.

[57] J.P. Ponpon, *Solid-State Electron.*, vol. 28, p. 689, 1985.

[58] Y. Eisen, *Nucl. Instrum. and Methods*, vol. A380, p. 431, 1996.

[59] D. Rose, K. Durose, W. Paloszand, A. Szczerbakow, and K. Grasza, *J. Phys. D: Appl. Phys.*, vol. 31, p. 1009, 1998.

[60] Daniel Lincot and Jacques Vedel, *J. Electroanal. Chem.*, vol. 175, p. 207, 1984.

[61] D. Landolt, *Electrochim. Acta*, vol. 32, p. 1, 1987.

[62] P.M. Amirtharaj and Fred H. Pollak, *Appl. Phys. Lett.*, vol. 45, p. 789, 1984.

[63] M. Saji and N. Kondon, *Oyo Butsuri*, vol. 54, p. 835, 1985.

[64] T. Ozaki, Y. Iwase, H. Takamura, and M. Ohmori, *Nucl. Instrum. and Methods*, vol. A380, p. 141, 1996.

[65] H. Cordes and R. Schmid-Fetzer, *Semicond. Sci. Technol.*, vol. 9, p. 2085, 1994.

[66] A. Szczerbakow, J. Domagala, D. Rose, K. Durose, V.Yu. Ivanov, and A.R. Omeltchouk, *J. Cryst. Growth*, vol. 191, p. 673, 1998.

[67] I.M. Dharmadasa, A.B. McLean, M.H. Patterson, and R.H. Williams, *Semicond. Sci. Technol.*, vol. 2, p. 404, 1987.

[68] B. Daudin, D. Brun-Le Cunff, and S. Tatarenko, *Surf. Sci.*, vol. 352, p. 99, 1996.

[69] D.E. Aspnes and H. Arwin, *J. Vac. Sci. Technol., A*, vol. 2, p. 1309, 1984.

[70] U. Sassenberg, H. Berger, and A. Engel, *Cryst. Res. Technol.*, vol. 22, p. K86, 1987.

[71] J.P. Ponpon, *Appl. Phys. A*, vol. 27, p. 11, 1982.

[72] M. Hage-Ali, R. Stuck, A.N. Saxena, and P. Siffert, *Appl. Phys. A*, vol. 19, p. 25, 1979.

[73] D.L. Bätzner, R. Wendt, A. Romeo, H. Zogg, and A.N. Tiwari, *Thin Solid Films*, vol. 361, p. 463, 2000.

[74] W.J. Danaher, L.E. Lyons, M. Marychurch, and G.C. Morris, *Appl. Surf. Sci.*, vol. 27, p. 338, 1986.

[75] W.H. Chang, T. Lee, and W.M. Lau, *J. Appl. Phys.*, vol. 68, p. 4816, 1990.

[76] Z. Sobiesierski, I.M. Dharmadasa, and R.H. Williams, *Appl. Phys. Lett.*, vol. 53, p. 2623, 1988.

[77] Y. Luo, D.A. Slater, M. Levy, and R.M. Osgood Jr., *Appl. Surf. Sci.*, vol. 104, p. 49, 1996.

[78] H. Yoon, J.M. VanScyoc, and M.S Goorsky, *J. Electron. Mater.*, vol. 26, p. 529, 1997.

[79] M.S. Han and T.W. Kang amd T.W. Kim, *Appl. Surf. Sci.*, vol. 148, p. 105, 1999.

[80] L. Wang, W. Sang, W. Shi, Y. Qian, J. Min, D. Liu, and Y. Xia, *Nucl. Instrum. and Methods*, vol. A448, p. 581, 2000.

[81] A. Burger, H. Chen, K. Chattopadhyay, D. Shi, S.H. Morgan, W.E. Collins, and R.B. James, *Nucl. Instrum. Methods Phys. Res., Sect. A*, vol. 428, p. 8, 1999.

[82] P.J. Ireland, *Thin Solid Films*, vol. 304, p. 1, 1997.

[83] O.S. Galkina, N.N. Grebenyuk, M.V. Dobrotvorskaya, V.K. Komar, and D.P. Nalivaiko, *Funct. Mat.*, vol. 8, p. 392, 2001.

[84] A.J. Fusco and B.C. Cochran, "Method for polishing detector material," Pat. USA # 4600469.

[85] P.W. Leech, P.J. Gwynn, and M.H. Kibel, *Appl. Surf. Sci.*, vol. 37, p. 291, 1989.

[86] P.W. Leech, M.H. Kibel, and P.J. Gwynn, *J. Electrochem. Soc.*, vol. 137, p. 705, 1990.

[87] G.N. Pain, N. Bharatula, T.J. Elms, P. Gwynn, M. Kibel, M.S. Kwietniak, P. Leech, N. Petkovic, C. Sandford, J. Thompson, T. Warminski, D. Gao, S.R. Glanvill, C.J. Rossouw, and A.W. Stevenson, *J. Vac. Sci. Technol., A*, vol. 8, p. 1067, 1990.

[88] O.S. Galkina, N.N. Grebenyuk, M.V. Dobrotvorskaya, V.K. Komar, D.P. Nalivaiko, and O.N. Chugai, *Funct. Mat.*, vol. 9, p. 463, 2002.

[89] Z.F. Tomashik, O.R. Gumenyuk, and V.N. Tomashik, *Proc. SPIE*, vol. 5065, p. 241, 2003.

[90] W. Kern, *RCA Rev.*, vol. 39, p. 278, 1978.

[91] B. Schwartz and H. Robbins, *J. Electrochem. Soc.*, vol. 111, p. 196, 1964.

[92] B. Schwartz and H. Robbins, *J. Electrochem. Soc.*, vol. 123, p. 1903, 1976.

[93] R.N. Zitter, *Surf. Sci.*, vol. 28, p. 335, 1971.

[94] M.H. Patterson and R.H. Williams, *J. Phys. D: Appl. Phys.*, vol. 11, p. L83, 1978.

[95] A.J. Ricco, H.S. White, and M.S. Wrighton, *J. Vac. Sci. Technol., A*, vol. 2, p. 910, 1984.

[96] P. Gaugash and A.G. Milnes, *J. Electrochem. Soc.*, vol. 128, p. 924, 1981.

[97] H.C. Montgomery, *Solid-State Electron.*, vol. 7, p. 147, 1964.

[98] I. Hähnert and M. Wienecke, *Mater. Sci. Eng., B*, vol. 16, p. 168, 1993.

[99] L.E. Lyons, G.C. Morris, N.A. Raftery, and T.L. Young, *Aust. J. Chem.*, vol. 40, p. 655, 1987.

[100] M. Inoue, I. Teramoto, and S. Takayanagi, *J. Appl. Phys.*, vol. 33, p. 2578, 1962.

[101] W. Faschinger, K. Lischka, and H. Sitter, *Chemtron.*, vol. 2, p. 28, 1987.

[102] Y.-C. Lu, C.M. Stahle, R.S. Feigelson, and J. Morimoto, *J. Appl. Phys.*, vol. 62, p. 4453, 1987.

[103] K. Chattopadhyay, S. Feth, H. Chen, A. Burger, and Ching-Hua Su, *J. Cryst. Growth*, vol. 191, p. 377, 1998.

[104] B.J. Kowalski, B.A. Orowski, and J. Ghijsen, *Surf. Sci.*, vol. 412, p. 544, 1998.

[105] T. Takeuchi, T. Kore-eda, and A. Ebina, *Appl. Surf. Sci.*, vol. 100, p. 596, 1996.

[106] S.C. Gupta, F.R. Chavada, S.K. Koul, and M. Gautanam, *J. Electrochem. Soc.*, vol. 135, p. 2899, 1988.

[107] B. Wermke, M. Mühlberg, A. Engel, and P. Rudolph, *Cryst. Res. Technol.*, vol. 24, p. 365, 1989.

[108] K. Nakagawa, K. Maeda, and S. Takeuchi, *Appl. Phys. Lett.*, vol. 34, p. 574, 1979.

[109] S. Zhu, B. Zhao, Q. Li, F. Yu, S. Shao, and X. Zhu, *J. Cryst. Growth*, vol. 208, p. 264, 2000.

[110] http://www.nikko-metal.co.jp/products/05_kagou/pdf/puremetal.pdf

[111] L. Turjanska, P. Höschl, E. Belas, R. Grill, J. Franc, and P. Moravec, *Nucl. Instr. Methods A*, vol. 90, p. 458, 2001.

[112] L.J. van der Pauw, *Phillips Res. Repts*, vol. 13, p. 1, 1958.

[113] L.J. van der Pauw, *Phillips Tech. Rev.*, vol. 20, p. 220, 1958.

[114] R.Grill, L.Turjanska, J.Franc, E.Belas, I.Turkevych, and P.Höschl, *Phys. Stat. Sol. B*, vol. 229, p. 161, 2002.

[115] A.M. Goodman, *J. Appl. Phys.*, vol. 34, p. 329, 1963.

[116] R. Stibal, J. Windscheif, and W. Jantz, *Semicond. Sci. Technol.*, vol. 6, p. 995, 1991.

[117] P. Fochuk, O. Panchuk, L. Shcherbak, and P. Siffert, *Phys. Stat. Sol. C*, vol. 2, p. 1178, 2005.

[118] M.U. Ahmed and E.D. Jones, *EMIS Datareviews Series No. 10*, chapter B4.2, p. 466, INSPEC, London, January 1994.

[119] S.H. Wei and S.B. Zhang, *Phys. Rev. B*, vol. 66, p. 155211, 2002.

[120] W. Shockley and W.T. Read, *Phys. Rev.*, vol. 87, 1952.

[121] J.W. Mayer, *Semiconductor Detectors*, p. 445, North Holland, Amsterdam, 1968.

[122] C. Szeles, Y.Y. Shan, K.G. Lynn, and E.E. Eissler, *Nucl. Instr. and Methods*, vol. A380, p. 148, 1996.

[123] A. Castaldini, A. Cavallini, B. Fraboni, P. Fernandez, and J. Piqueras, *J. Appl. Phys.*, vol. 83, p. 2121, 1998.

[124] H. Elhadidy, J. Franc, P. Moravec, P. Höschl, and M. Fiederle, *Semicond. Sci. Technol.*, vol. 22, p. 537, 2007.

[125] J. Franc, R. Grill, J. Kubát, P. Hlídek, E. Belas, P. Moravec, and P. Höschl, *J. Electron. Mater.*, vol. 35, p. 988, 2006.

[126] E.H. Nicollian and J.R. Brews, *MOS (Metal-Oxide-Semiconductor) Physics and Technology*, Wiley, New York, 1982.

[127] http://www.amptek.com/cdte.html